nature research

https://doi.org/10.1038/s41551-020-00604-w

Supplementary information

Catheter-integrated soft multilayer electronic arrays for multiplexed sensing and actuation during cardiac surgery

In the format provided by the authors and unedited

Table of Contents

Supplementary Note 1: Fabrication procedures for the multimodal, multiplexed electronics

I. Electrode array

Preparation of substrate

1. Clean Si wafers with acetone and IPA

2. Deposit Ti/Cu (10 nm/100 nm in thickness) as sacrificial layer

Bottom polymer

3. Spin coat PI2545 (1500 rpm, 40 s; bake at 110 °C for 180 s, 150 °C for 300 s; fully cure)

Metal layer

4. Define metal pattern using photoresist (AZ nLof 2035, 5000 rpm)

5. Oxygen plasma treatment for 1min (March RIE 190 mT, 100 W, 19 sccm)

6. Deposit Cr/Au (10 nm/300 nm in thickness) using electron-beam evaporation

7. Lift off in acetone (sonicate if necessary)

Top polymer

8. Spin coat PI2545 (1500 rpm, 40 s; bake at 110 °C for 180 s, 150 °C for 300 s; fully cure)

9. Deposit SiO_2 (100 nm in thickness) as hard mask

10. Define top polymer pattern using photoresist (S1813, 4000 rpm)

11. Dry etch of SiO_2 in reactive ion etcher (RIE) with CF_4 (Samco RIE-10NR)

12. Oxygen plasma etching of PI2545 (March RIE 200 mT, 200 W, 20 sccm)

Transfer printing

13. Undercut Cu sacrificial layer in copper etchant

14. Transfer electrode array from silicon wafer to water soluble tape (designated as **DEVICE 1**)

II. Temperature sensor array

Preparation of substrate

15. Clean Si wafers with acetone and IPA

16. Deposit Ti/Cu (10 nm/100 nm in thickness) as sacrificial layer

Bottom polymer

17. Spin coat PI2545 (1500 rpm, 40 s; bake at 110 °C for 180 s, 150 °C for 300 s; fully cure)

First metal layer

18. Define metal pattern using photoresist (AZ nLof 2035, 5000 rpm)

19. Oxygen plasma treatment for 1min (March RIE 190 mT, 100 W, 19 sccm)

20. Deposit Cr/Au (10 nm/100 nm in thickness) using electron-beam evaporation

21. Lift off in acetone (sonicate if necessary)

Middle polymer

22. Spin coat PI2545 (6000 rpm, 40 s; bake at 110 °C for 180 s, 150 °C for 300 s; fully cure)

Via

23. Define via pattern using photoresist (AZ 4620, 2000 rpm)

24. Oxygen plasma etching of PI2545 (March RIE 200 mT, 200 W, 20 sccm)

25. Remove photoresist in acetone

Second metal layer

26. Deposit Cr/Au (10 nm/100 nm in thickness) using sputter to cover the side walls

27. Define metal pattern using photoresist (S1813, 4000 rpm)

28. Etch Au/Cr with gold and chromium etchant

29. Remove photoresist in acetone

Top polymer

30. Spin coat PI2545 (6000 rpm, 40 s; bake at 110 °C for 180 s, 150 °C for 300 s; fully cure)

31. Deposit Cu (100 nm in thickness) as hard mask

32. Define top polymer pattern using photoresist (S1813, 4000 rpm)

32. Etch Cu with diluted copper etchant

33. Oxygen plasma etching of PI2545 (March RIE 200 mT, 200 W, 20 sccm)

Transfer printing

34. Undercut Cu sacrificial layer in copper etchant

35. Transfer temperature array from silicon wafer to water soluble tape

36. Deposit SiO_2 (100 nm in thickness) on water soluble tape through a shadow mask

37. Spin coat PMMA on a glass slide(3000 rpm, 40 s; bake at 180 °C for 180 s)

38. Spin coat Ecoflex 0030 on the glass slide (1500 rpm, 40 s; bake at 70 °C for 1 h)

39. UVO treatment of Ecoflex 0030 and water soluble tape with SiO_2 for 4 min

40. Print water soluble tape onto Ecoflex 0030 (SiO_2 side facing down, bake at 70 °C for 10 min)

41. Dissolve water soluble tape with warm water to expose the temperature sensor array (designated as **DEVICE 2**)

III. Pressure sensor array

Preparation of substrate

42. Clean Si wafers with acetone and IPA

43. Deposit Ti/Cu (10 nm/100 nm in thickness) as sacrificial layer

Bottom polymer

44. Spin coat PI2545 (1500 rpm, 40 s; bake at 110 °C for 180 s, 150 °C for 300 s; fully cure)

First metal layer

45. Define metal pattern using photoresist (AZ nLof 2035, 5000 rpm)

46. Oxygen plasma treatment for 1min (March RIE 190 mT, 100 W, 19 sccm)

47. Deposit Cr/Au (10 nm/100 nm in thickness) using electron-beam evaporation

48. Lift off in acetone (sonicate if necessary)

Middle polymer

49. Spin coat PI2545 (6000 rpm, 40 s; bake at 110 °C for 180 s, 150 °C for 300 s; fully cure)

Via

50. Define via pattern using photoresist (AZ 4620, 2000 rpm)

51. Oxygen plasma etching of PI2545 (March RIE 200 mT, 200 W, 20 sccm)

52. Remove photoresist in acetone

Second metal layer

53. Deposit Cr/Au (10 nm/100 nm in thickness) using sputter to cover the side walls

54. Define metal pattern using photoresist (S1813, 4000 rpm)

55. Etch Au/Cr with gold and chromium etchant

56. Remove photoresist in acetone

Top polymer

57. Spin coat PI2545 (6000 rpm, 40 s; bake at 110 °C for 180 s, 150 °C for 300 s; fully cure)

58. Deposit Cu (100 nm in thickness) as hard mask

59. Define top polymer pattern using photoresist (S1813, 4000 rpm)

60. Etch Cu with diluted copper etchant

61. Oxygen plasma etching of PI2545 (March RIE 200 mT, 200 W, 20 sccm)

Transfer printing

62. Undercut Cu sacrificial layer in copper etchant

63. Transfer temperature array from silicon wafer to water soluble tape

64. Deposit SiO_2 (100 nm in thickness) with a shadow mask to define the bonding sites

Compressive buckling

65. Prepare silicone (e.g. Dragon Skin 10 slow) as the elastomer for compressive buckling

66. UVO treatment of silicone and water soluble tape with SiO_2 for 4 min

67. Print water soluble tape onto pre-stretched silicone (SiO_2 side facing down, bake at 70 °C for 10 min)

68. Dissolve water soluble tape with warm water

69. Release the prestrain to form 3D pressure sensor array

Rigid cavities on top

70. Clean Si wafer with acetone and IPA

71. Thinning part of the silicon wafer with laser (LPKF ProtoLaser R)

72. Cutting outline of the silicon wafer with laser (LPKF ProtoLaser R) to yield Si rigid cavities

73. Spin coat PDMS (1:10, 3000 rpm) on a glass slide

74. Place bottom surfaces of the rigid cavities onto uncured PDMS

75. Align rigid cavities on top of 3D pressure sensor array

76. Cure PDMS at 70 °C for 1 h

Rigid islands at the bottom

77. Laminate PI film (12.5 μm in thickness) onto water soluble tape

78. Laser cut PI film into squares as rigid islands, peel off extra PI film

79. Deposit SiO_2 (100 nm in thickness)

80. Align rigid islands at the bottom surface of the 3D pressure sensor array (designated as **DEVICE 3**)

**Fabrication procedures for the constantan-based pressure sensor array appear in Supplementary Note 2.*

IV. Vertically stacking of multilayer electronics

Preparation of PDMS stamp with micro patterns

81. Clean Si wafers with acetone and IPA

82. Define PDMS pattern using photoresist (AZ 4620, 2000 rpm)

83. Deep reactive-ion etching of Si

84. Remove photoresist in Nanostrip

85. Pour PDMS (1:10) onto Si mold, cure at 70 °C for 1 h, detach PDMS from Si mold

86. Deposit parylene-C (4 μm in thickness) on PDMS stamp

Stacking electrode array (DEVICE 1) with temperature sensor array (DEVICE 2)

87. Spin coat PI2545 (3000 rpm)

88. Place PDMS stamp onto uncured PI

89. Align uncured PI pattern on PDMS stamp to **DEVICE 2**

90. Align **DEVICE 1** to **DEVICE 2** with uncured PI as the adhesive layer

91. Bake at 110 °C for 1 h, dissolve water soluble tape on **DEVICE 1** with warm water

92. Bake at 150 °C for 300 s, fully cure PI

Stacking electrode & temperature sensor arrays (DEVICE 1&2) with pressure sensor array (DEVICE 3)

93. UVO treatment of the top surface of **DEVICE 3** and bottom surface of **DEVICE 1&2** for 4 min

94. Align **DEVICE 1&2** to **DEVICE 3**, bake at 70 °C for 10 min

V. Instrument on balloon catheters and wire connection

95. Bond connectors and ACF cables to the stacked multilayer electronics

96. Dip-coating a thin layer of Ecoflex 0030 on balloon catheters (deflated silicone balloon or inflated PU balloon)

97. Cure Ecoflex 0030 with hot air at 100 °C

98. Corona treatment of balloon catheters for 1 min and UVO treatment of the stacked multilayer electronics for 4 min

99. Laminate multilayer electronics on balloon catheters, bake at 70 °C for 10 min

100. Dissolve water soluble tape with warm water

Supplementary Note 2: Scaling law for tissue ablation

In the present study, three physical fields (electric currents, bioheat transfer, and electrical circuit) were considered to predict the tissue ablation in COMSOL software. Simulations suggest that the resistance

heating and heat transfer mainly dominate the tissue ablation. Therefore, the governing equation for electric currents dictates

$$\begin{aligned} &\nabla \cdot \mathbf{J} = 0 \\ &\mathbf{J} = \sigma \mathbf{E} \\ &\mathbf{E} = -\nabla V \end{aligned} \quad \text{(eq1)}$$

where $\mathbf{J}, \mathbf{E}, \sigma,$ and V is current density, electric field intensity, electrical conductivity, and potential, respectively. The governing equation for bioheat transfer dictates

$$\begin{aligned} &\rho C_{\mathrm{p}} \frac{\partial T}{\partial t} + \nabla \cdot \mathbf{q} = Q_{\mathrm{e}} \\ &\mathbf{q} = -k \nabla T \\ &Q_{\mathrm{e}} = \mathbf{J} \cdot \mathbf{E} \end{aligned} \quad \text{(eq2)}$$

where $\rho, C_{\mathrm{p}}, \mathbf{q}, k,$ and Q_{e} is density, heat capacity, heat flux, thermal conductivity and resistance heating source, respectively.

Firstly, the substrate underneath the electrode was ignored, and steady-state heat transfer for bipolar ablation was considered. In conjunction with the boundary conditions, the temperature distribution in tissue follows $T - T_0 = f\left(V_0, \sigma, L, S, k, x, y, z\right)$ (eq3)

where $T_0, V_0, L,$ and S are the initial temperature, the applied potential on electrode, the electrode spacing, and the electrode size as shown in Supplementary Fig. 54a, respectively. Combination of (eq1)-(eq3) gives the scaling law

$$\frac{k\left(T - T_0\right)}{\sigma V_0^2} = f\left(\frac{S}{L}, \frac{x}{L}, \frac{y}{L}, \frac{z}{L}\right) \quad \text{(eq4).}$$

For normal tissue, the irreversible damage occurs quickly when the temperature larger than T_{c} = 60 °C. The FEA validation of the scaling law was shown in Supplementary Fig. 54b. Then, the bipolar lesion size can be obtain as an integration of a bool function,

$$\begin{cases} D = L\int \mathrm{Bool}\cdot d\dfrac{z}{L} \\ A = L^2\int \mathrm{Bool}\cdot d\dfrac{x}{L}d\dfrac{y}{L} \\ V = L^3\int \mathrm{Bool}\cdot d\dfrac{x}{L}d\dfrac{y}{L}d\dfrac{z}{L} \end{cases} \quad \text{(eq5)}$$

where $\mathrm{Bool}=\begin{cases}1 & T-T_c\geq 0\\ 0 & T-T_c<0\end{cases}$, D, A, and V are the lesion depth, area, and volume, respectively. Therefore, the scaling law for lesion size dictates

$$\begin{cases} D/L = g_1\left(\dfrac{S}{L},\dfrac{k\left(T_c-T_0\right)}{\sigma V_0^2}\right) \\ A/L^2 = g_2\left(\dfrac{S}{L},\dfrac{k\left(T_c-T_0\right)}{\sigma V_0^2}\right) \\ V/L^3 = g_3\left(\dfrac{S}{L},\dfrac{k\left(T_c-T_0\right)}{\sigma V_0^2}\right) \end{cases} \quad \text{(eq6).}$$

The FEA validation of the scaling law was shown in Supplementary Fig. 55, suggesting good consistency. For steady-state monopolar tissue ablation, the tissue thickness (H) has a significant influence. Similarly, the scaling law for monopolar lesion size dictates

$$\begin{cases} D/H = g_1\left(\dfrac{S}{H},\dfrac{k\left(T_c-T_0\right)}{\sigma V_0^2}\right) \\ A/H^2 = g_2\left(\dfrac{S}{H},\dfrac{k\left(T_c-T_0\right)}{\sigma V_0^2}\right) \\ V/H^3 = g_3\left(\dfrac{S}{H},\dfrac{k\left(T_c-T_0\right)}{\sigma V_0^2}\right) \end{cases}$$

(eq7).

The FEA validation of the scaling law was shown in Supplementary Fig. 56, suggesting a good consistency.

Secondly, the substrate underneath the electrode was considered. It was found that the thickness (H_{top}) and thermal conductivity (k_{top}) of the substrate underneath the electrode had a considerable influence on tissue ablation. Then, the scaling law for bipolar lesion size rewrites as

$$\begin{cases} D/L = g_1\left(\dfrac{S}{L}, \dfrac{k\left(T_c - T_0\right)}{\sigma V_0^2}, \dfrac{k_{top}}{k}, \dfrac{H_{top}}{L}\right) \\ A/L^2 = g_2\left(\dfrac{S}{L}, \dfrac{k\left(T_c - T_0\right)}{\sigma V_0^2}, \dfrac{k_{top}}{k}, \dfrac{H_{top}}{L}\right) \\ V/L^3 = g_3\left(\dfrac{S}{L}, \dfrac{k\left(T_c - T_0\right)}{\sigma V_0^2}, \dfrac{k_{top}}{k}, \dfrac{H_{top}}{L}\right) \end{cases} \quad \text{(eq8).}$$

The influence of the thickness (H_{top}) and thermal conductivity (k_{top}) of the substrate underneath the electrode on tissue ablation was shown in Supplementary Fig. 57.

Supplementary Note 3: Scaling law for electroporation in a potato model

A pulsed potential was applied during the bipolar potato electroporation, which contributes to the low temperature increase as shown in Supplementary Fig. 59. Therefore, only (eq1) governs the electric filed distribution during bipolar electroporation. In conjunction with the boundary conditions, the electric field intensity distribution in the potato follows

$$E = f\left(V_0, L, S, x, y, z\right) \quad \text{(eq9).}$$

Dimensional analysis gives the scaling law as follows

$$\frac{E}{V_0/L} = f\left(\frac{S}{L}, \frac{x}{L}, \frac{y}{L}, \frac{z}{L}\right) \quad \text{(eq10).}$$

The irreversible damage occurs when the electric field intensity larger than $E_c = 500\ \mathrm{V/cm}$. Then, the scaling law for lesion size in potato during bipolar electroporation dictates

$$\begin{cases} D/L = g_1\left(\dfrac{S}{L}, \dfrac{E_c L}{V_0}\right) \\ A/L^2 = g_2\left(\dfrac{S}{L}, \dfrac{E_c L}{V_0}\right) \\ V/L^3 = g_3\left(\dfrac{S}{L}, \dfrac{E_c L}{V_0}\right) \end{cases} \quad \text{(eq11).}$$

The FEA validation of the scaling law is shown in Supplementary Fig. 63, suggesting good consistency.

Supplementary Note4: Theoretical analysis of the temperature differences between the electrode and temperature sensor

In the present five-layer model (Supplementary Fig. 66a), the electrode and sensor layer were ignored due to their much smaller thickness in comparison to others. The steady-state heat transfer along the thickness was studied. The natural convection in the exterior boundary was considered. Firstly, full bonding between adjacent layers, namely, no thermal contact resistance between adjacent layers, was considered. The heat flux thorough each layer gives

$$Q = -\frac{k_i}{t_i}\left(T_i - T_{i-1}\right) + \frac{4t_i}{S}\cdot h\left(T_{\mathrm{a}} - \frac{T_i + T_{i-1}}{2}\right) \quad \text{(eq12)}$$

where k_i, t_i, T_i, T_{a}, h, and S is the thermal conductivity, thickness of layer i, the temperature at the interface of between layer i and layer i+1, the ambient temperature, the natural convective heat transfer coefficient, and the size of each layer, respectively. The boundary condition on the top surface of layer 5 gives

$$Q = -h(T_{\mathrm{a}} - T_5) \quad \text{(eq13)}$$

where T_5 is the top surface temperature of the layer 5 as shown in Supplementary Fig. 66a. Combination of (eq12) and (eq13), the temperature difference between the electrode and temperature sensor can be written as the function the thickness of layer 2, namely, $T_0 - T_3 = f\left(t_2\right)$. The FEA validation of the theoretical analysis is shown in Supplementary Fig. 66c,d, suggesting a good consistency.

The interlayer polymer (layer 2) may have a rough surface due to the preparation process, which could cause incomplete contact between layer 1 and layer 2, and between layer 2 and layer 3. In this condition, the thermal contact resistance between layer 1 and 2, layer 2 and 3 was considered, which would introduce two interfacial temperatures, namely, T_{12} and T_{23}. Then, the heat flux thorough each layer gives

$$\begin{cases} Q = -\dfrac{k_i}{t_i}\left(T_i - T_{i-1}\right) + \dfrac{4t_i}{S}\cdot h\left(T_{\mathrm{a}} - \dfrac{T_i + T_{i-1}}{2}\right) \text{ for layer } i,\ i = 1, 4, 5 \\ Q = -\dfrac{1}{R}\left(T_{12} - T_1\right) = -\dfrac{1}{R}\left(T_{23} - T_2\right) \text{ at interface between layer 1 and 2, layer 2 and 3} \\ Q = -\dfrac{k_2}{t_2}\left(T_2 - T_{12}\right) + \dfrac{4t_2}{S}\cdot h\left(T_{\mathrm{a}} - \dfrac{T_2 + T_{12}}{2}\right) \text{ for layer 2} \\ Q = -\dfrac{k_3}{t_3}\left(T_3 - T_{23}\right) + \dfrac{4t_3}{S}\cdot h\left(T_{\mathrm{a}} - \dfrac{T_3 + T_{23}}{2}\right) \text{ for layer 3} \end{cases} \quad \text{(eq14)}$$

where R is the thermal contact resistance at the interface between layer 1 and 2, and between layer 2 and 3. Combination of (eq13) and (eq14), the temperature difference between the electrode and sensor can be written as the function the thermal contact resistance, namely, $T_0 - T_3 = f\left(R\right)$. The FEA validation of the theoretical analysis is shown in Supplementary Fig. 66e, suggesting good consistency.

Supplementary Note 5: Fabrication procedures for the constantan-based pressure sensor array

Preparation of substrate

1. Clean Si wafers with acetone and IPA

2. Deposit Ti/Cu (10 nm/100 nm in thickness) as sacrificial layer

Bottom polymer

3. Spin coat PI2545 (1500 rpm, 40 s; bake at 110 °C for 180 s, 150 °C for 300 s; fully cure)

First metal layer (row selection, Au)

4. Define metal pattern using photoresist (AZ nLof 2035, 5000 rpm)

5. Oxygen plasma treatment for 1min (March RIE 190 mT, 100 W, 19 sccm)

6. Deposit Cr/Au (10 nm/100 nm in thickness) using electron-beam evaporation

7. Lift off in acetone (sonicate if necessary)

Second metal layer (pressure sensor, constantan)

8. Define reversed metal pattern using photoresist (AZ nLof 2035, 5000 rpm)

9. Oxygen plasma treatment for 1min (March RIE 190 mT, 100 W, 19 sccm)

10. Deposit Mg (500 nm in thickness) using electron-beam evaporation

11. Lift off in acetone (sonicate if necessary)

12. Deposit Cr/constantan (10 nm/100 nm in thickness) using sputter at 100 °C

13. Dissolve Mg in hot water (sonicate if necessary)

Middle polymer

14. Spin coat PI2545 (6000 rpm, 40 s; bake at 110 °C for 180 s, 150 °C for 300 s; fully cure)

Via

15. Define via pattern using photoresist (AZ 4620, 2000 rpm)

16. Oxygen plasma etching of PI2545 (March RIE 200 mT, 200 W, 20 sccm)

17. Remove photoresist in acetone

Third metal layer (column selection, Au)

18. Deposit Cr/Au (10 nm/100 nm in thickness) using sputter to cover the side walls

19. Define metal pattern using photoresist (S1813, 4000 rpm)

20. Etch Au/Cr with gold and chromium etchant

21. Remove photoresist in acetone

Top polymer

22. Spin coat PI2545 (6000 rpm, 40 s; bake at 110 °C for 180 s, 150 °C for 300 s; fully cure)

23. Deposit Cu (100 nm in thickness) as hard mask

24. Define top polymer pattern using photoresist (S1813, 4000 rpm)

25. Etch Cu with diluted copper etchant

26. Oxygen plasma etching of PI2545 (March RIE 200 mT, 200 W, 20 sccm)

**The remaining steps follow the procedures for fabrication of Au-based pressure sensor array described in Supplementary Note 1.*

Supplementary Table 1. Comparison of the multiplexing strategies.

	Conventional Strategy	Our Strategy
Components at each pixel	transistors + sensors	only sensors
Positions of the active components	inside the array	outside of the array
Total number of wires (8 by 8 array)	24	8 (electrode) 16 (temperature/pressure sensor)
Fabrication procedures	microfabrication transfer printing	assembly on printed circuit board

Supplementary Table 2. Parameters used in FEA for tissue ablation.

Material	ρ (kg/m^3)	k (W/(m·K))	σ (S/m)	C_p (J/(kg·K))
Au	19300	317	$4.56*10^7$	129
Ecoflex	909	0.21	0	2100
Polystrene	1280	0.24	0	1250
Tissue	1079	$0.533+0.0028*(T-T_0)$	0.2, T<100 ºC	3870
			0, T>100 ºC	
Hydrogel	1000	k_0	$0.1+0.002*(T-T_0)$, T<100 ºC	4200
			0, T>100 ºC	
Cu	8960	400	$5.998*10^7$	385

k_0 = -0.869083936+0.00894880345*T-1.58366345E-5*T^2+7.97543259E-9*T^3.

Supplementary Table 3. Technical specification of the instrumented catheter system.

	Requirements	Instrumented Catheter System	Commercial Catheters
			HD 56 (Abbott) [1]
Electrogram mapping			
Spatial resolution	the higher the better	>0.5 mm^{-2} (64 pixels)	>0.3 mm^{-2} (56 pixels)
Temporal resolution	1 ms is sufficient	0.05 ms	1 ms
Impedance	the lower the better	~9 kΩ @ 1 kHz	/
			7F/4mm Blazer™ [2]
RF ablation			
Lesion depth	usually in mm scale	~0.2-3.2 mm	in mm scale
Lesion width	usually in mm scale	~0.5-10 mm^2	/
Temperature	>50 °C	>50 °C	>50 °C
Power to reach 50 °C	no requirement	0.44 W	~10 W
			20-mm-diameter 7F circular catheter [3]
IRE ablation			
Lesion depth	usually in mm scale	~0.6 mm @ 200 V	in mm scale
Lesion width	usually in mm scale	~2 mm @ 200 V	> 2 mm
Eclectic field intensity	>500 V/cm	>500 V/cm	>500 V/cm
Voltage to reach 500 V/cm	no requirement	<200 V	~1000 V
			THERMOCOOL®
Temperature mapping			
Spatial resolution	the higher the better	>0.5 mm^{-2} (64 pixels)	single pixel
Temporal resolution	0.1 s is sufficient	~0.025 s	/
Temperature range	30-80 °C	30-80 °C	can cover the range
Sensitivity	no requirement	0.17% $°C^{-1}$	/
			SMARTTOUCH®
Pressure mapping			
Spatial resolution	the higher the better	>0.5 mm^{-2} (64 pixels)	single pixel
Temporal resolution	0.1 s is sufficient	~0.025 s	/
Pressure range	0-30 kPa	0-30 kPa	can cover the range
Sensitivity	no requirement	8.2×10^{-5} kPa^{-1}	/

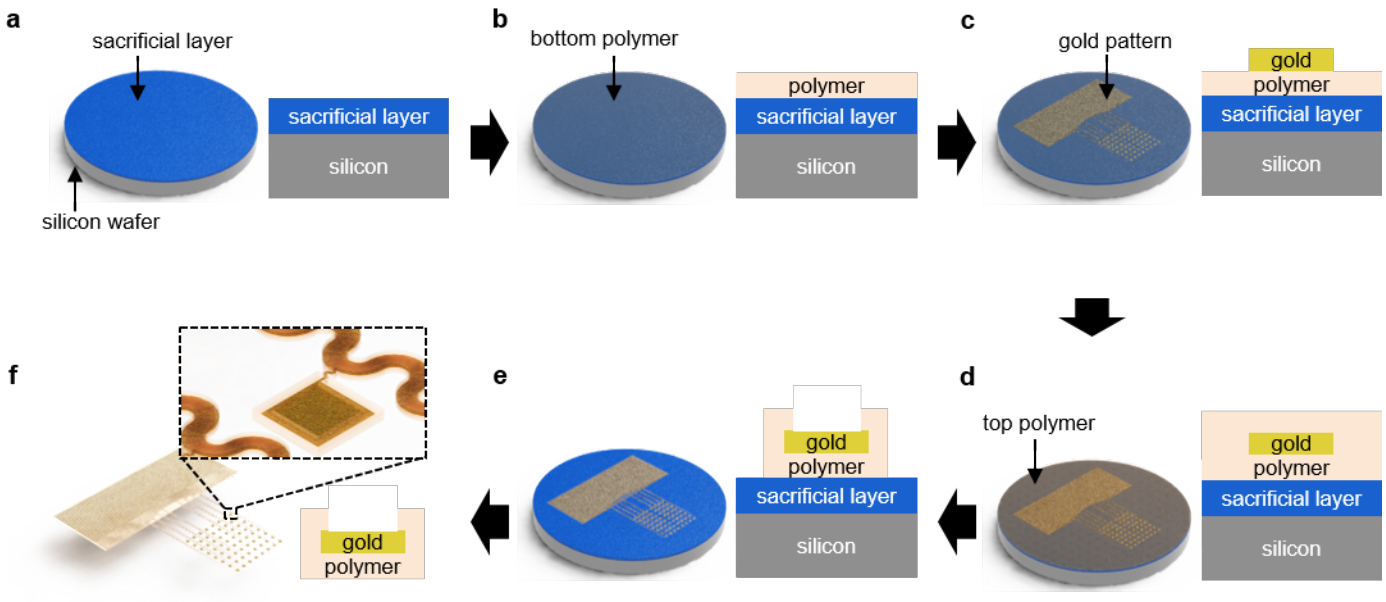

Supplementary Figure 1. Schematic illustration of the fabrication procedures for the electrode array. a, Prepare sacrificial layer on silicon wafer. **b,** Coat bottom polymer layer. **c,** Define gold pattern. **d,** Coat top polymer layer. **e,** Define polymer pattern. **f,** Undercut the sacrificial layer to release the electrode array.

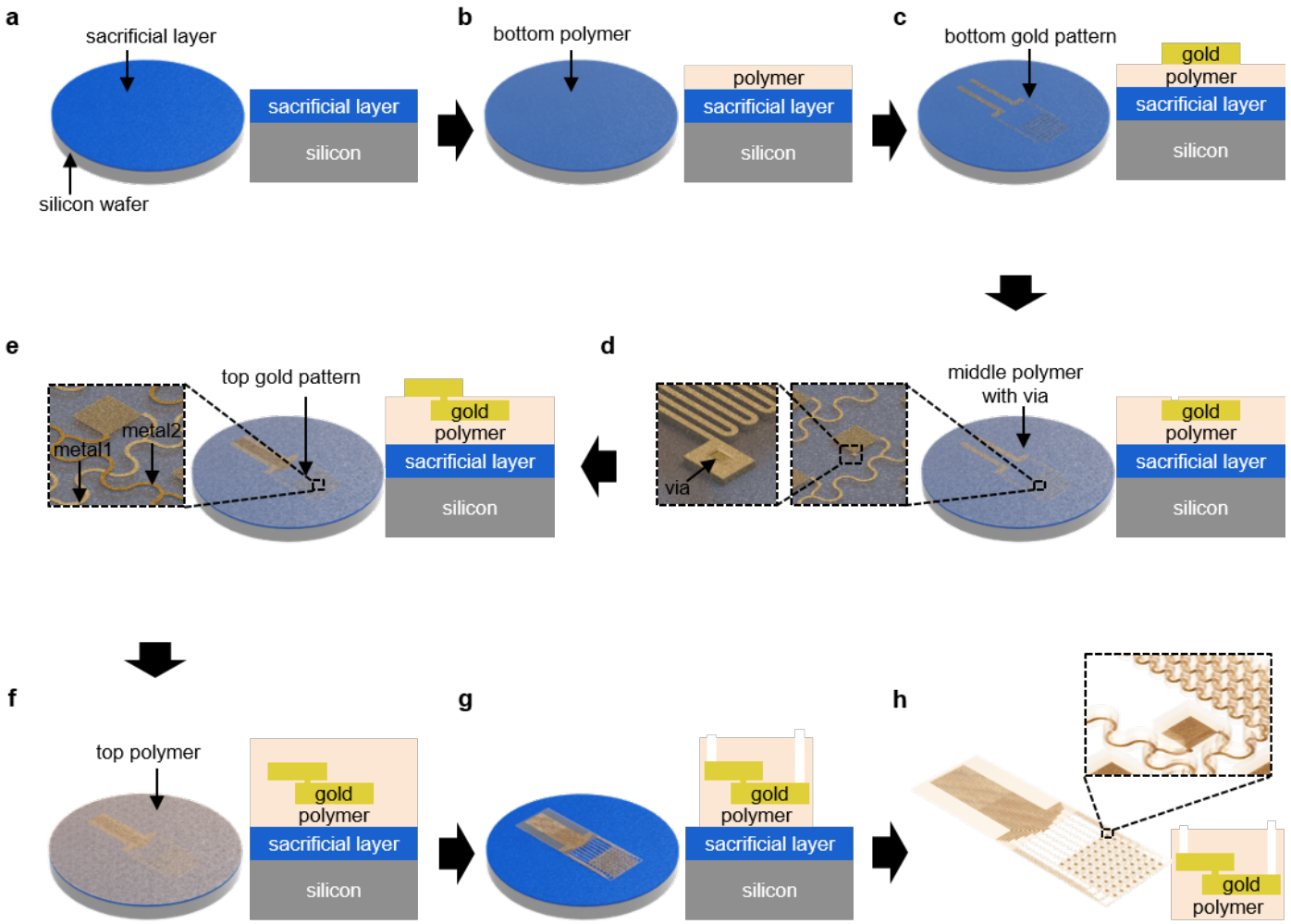

Supplementary Figure 2. Schematic illustration of the fabrication procedures for the temperature sensor array. a, Prepare sacrificial layer on silicon wafer. **b,** Coat bottom polymer layer. **c,** Define bottom gold pattern. **d,** Coat middle polymer layer and pattern via. **e,** Define top gold pattern. **f,** Coat top polymer layer. **g,** Define polymer pattern. **h,** Undercut the sacrificial layer to release the temperature sensor array.

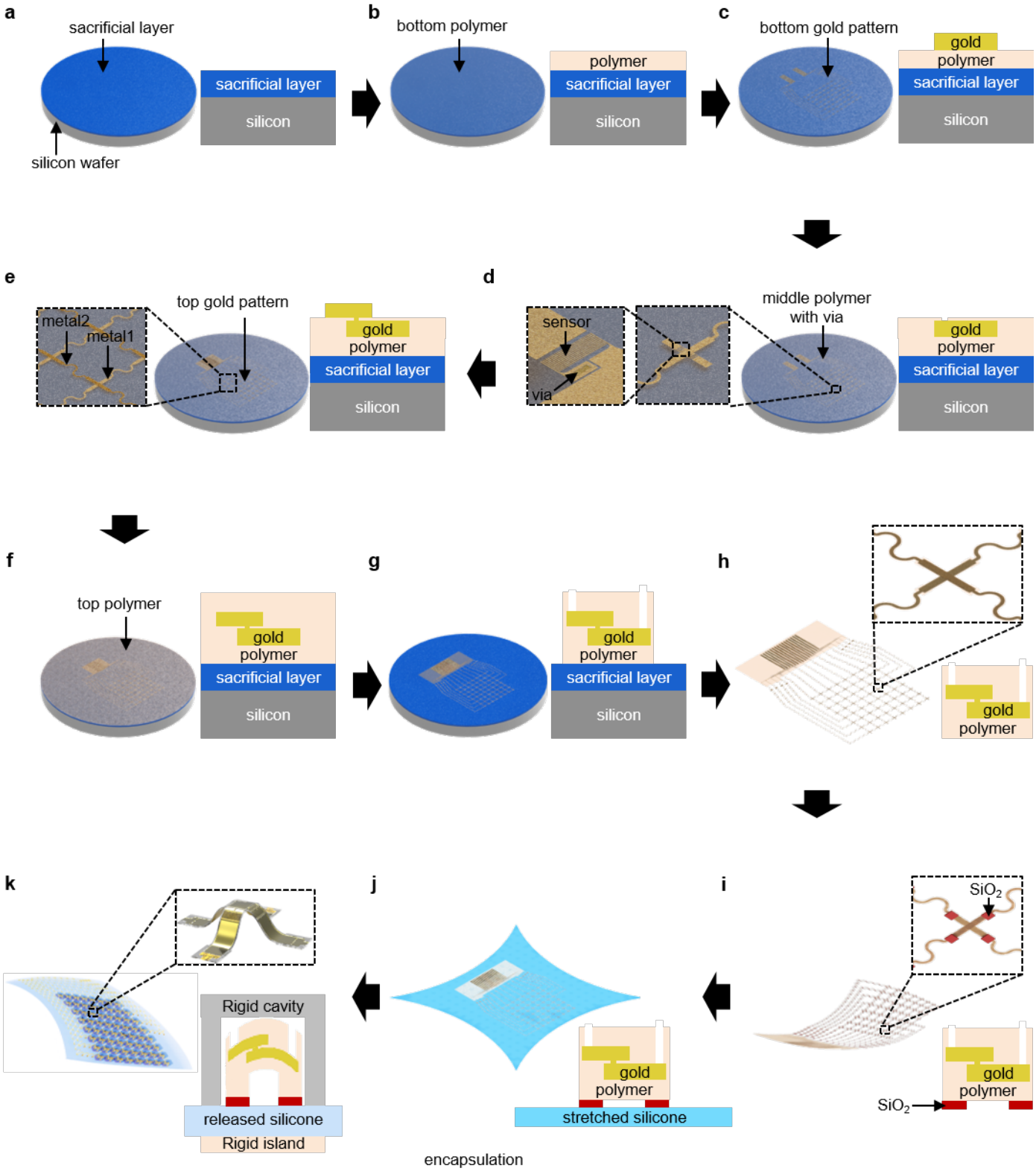

Supplementary Figure 3. Schematic illustration of the fabrication procedures for the pressure sensor array. a, Prepare sacrificial layer on silicon wafer. **b,** Coat bottom polymer layer. **c,** Define bottom gold pattern. **d,** Coat middle polymer layer and pattern via. **e,** Define top gold pattern. **f,** Coat top polymer layer. **g,** Define polymer pattern. **h,** Undercut the sacrificial layer to release the temperature sensor array. **i,** Define bonding sites via shadow mask. **j,** transfer to prestretched elastomer. **k,** Release the elastomer to form 3D mesostructures, bond rigid cavities and rigid islands.

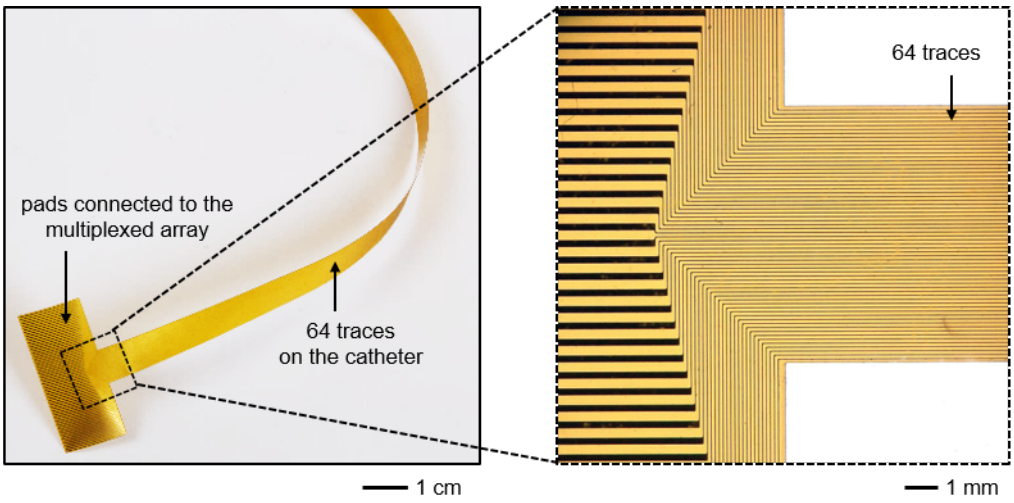

Supplementary Figure 4. Optical images of the flexible PCB connector.

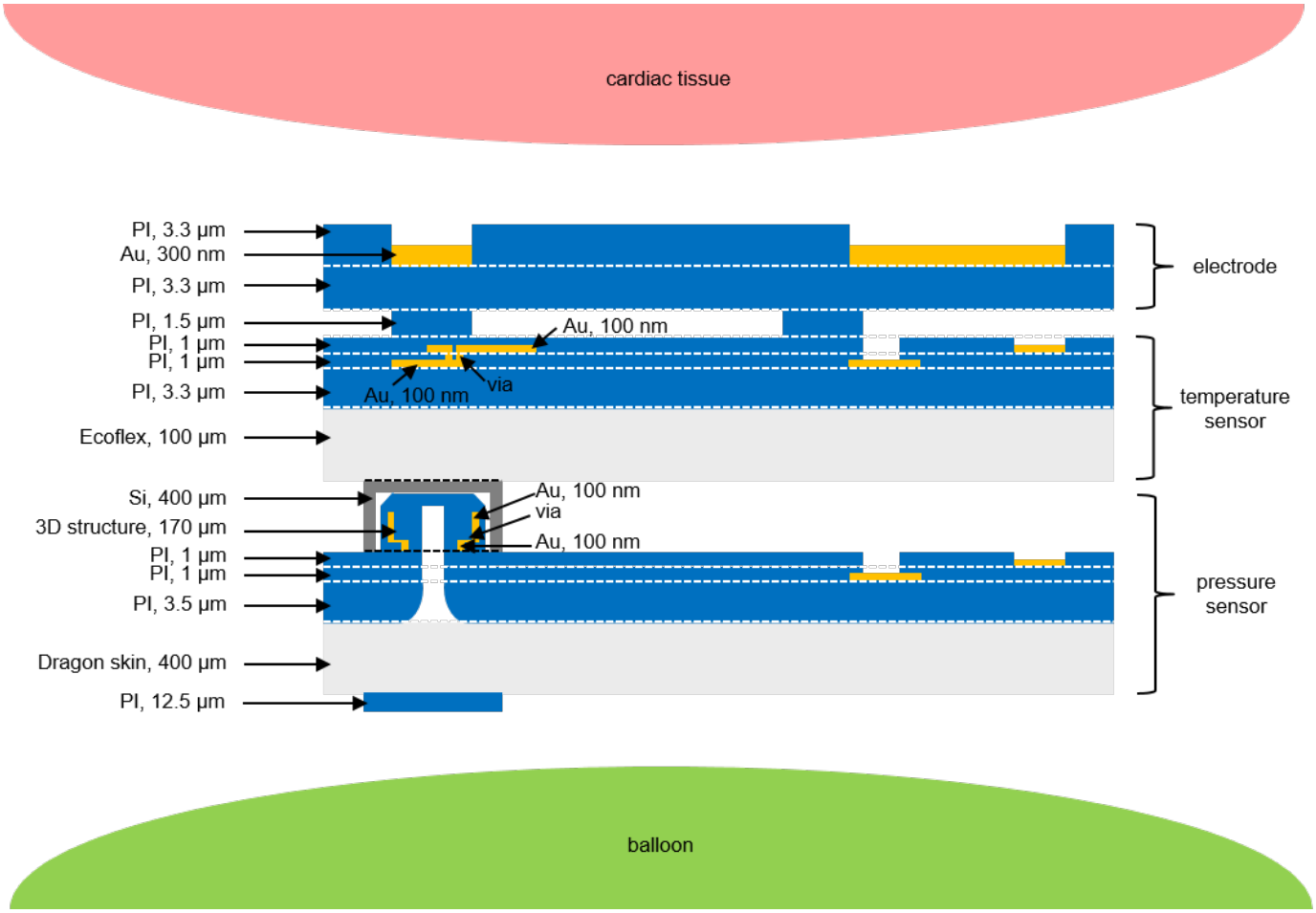

Supplementary Figure 5. Schematic illustration of the cross-section of the multifunctional, multiplexed electronics instrumented on a balloon catheter.

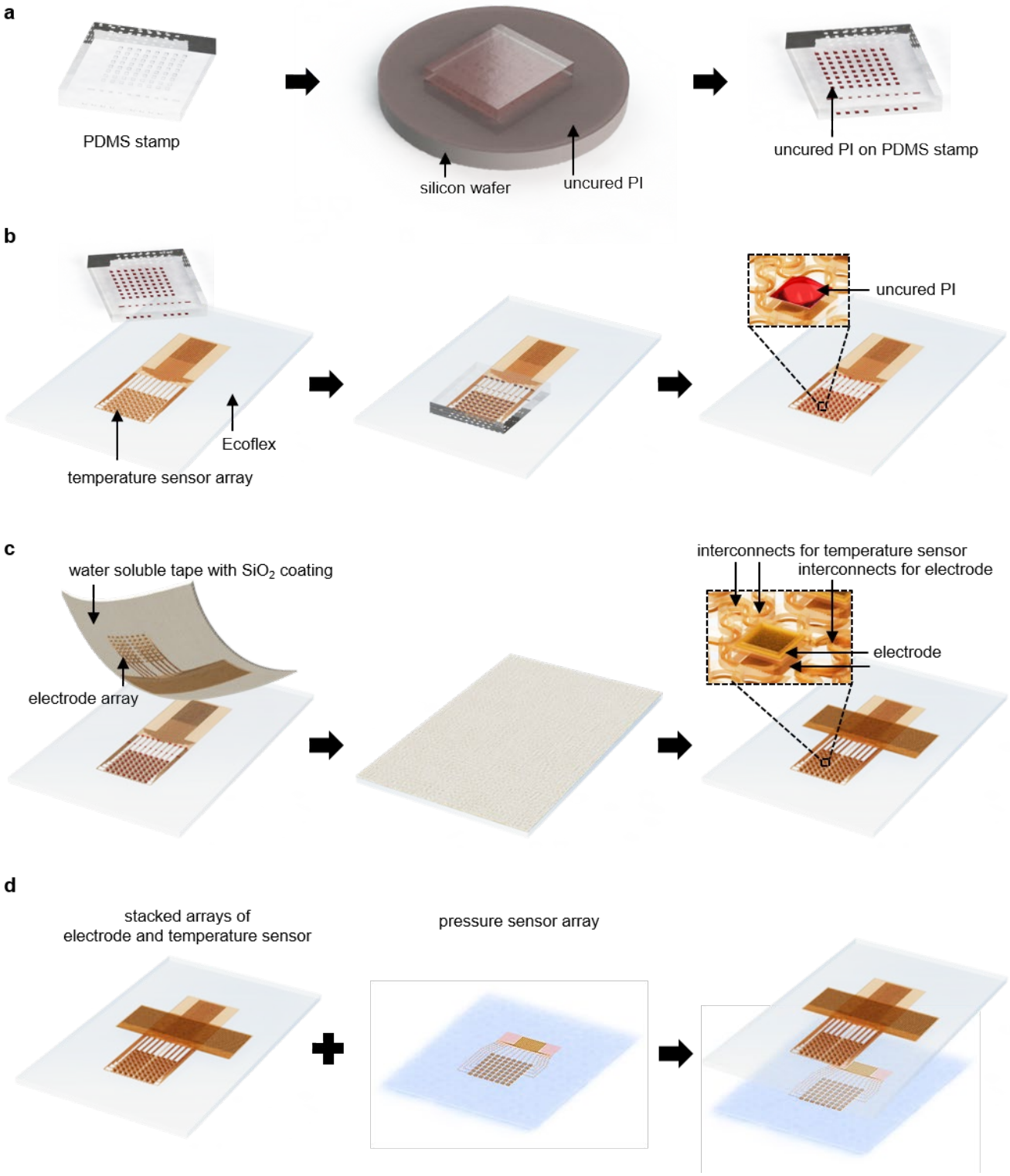

Supplementary Figure 6. Schematic illustration of the fabrication procedures for stacking multilayers of multiplexed electronics. a, Prepare PDMS stamp (left), attach PDMS stamp to uncured PI (middle), and detach PDMS stamp to get uncured PI pattern (right). **b,** Transfer the uncured PI pattern to temperature sensor array by attaching (left and middle) and detaching (right) the PDMS stamp. **c,** Align electrode array on water soluble tape to the temperature sensor array with uncured PI pattern (left and middle), and dissolve the water soluble tape (right). **d,** Align pressure sensor array to stacked layers of temperature sensor and electrode.

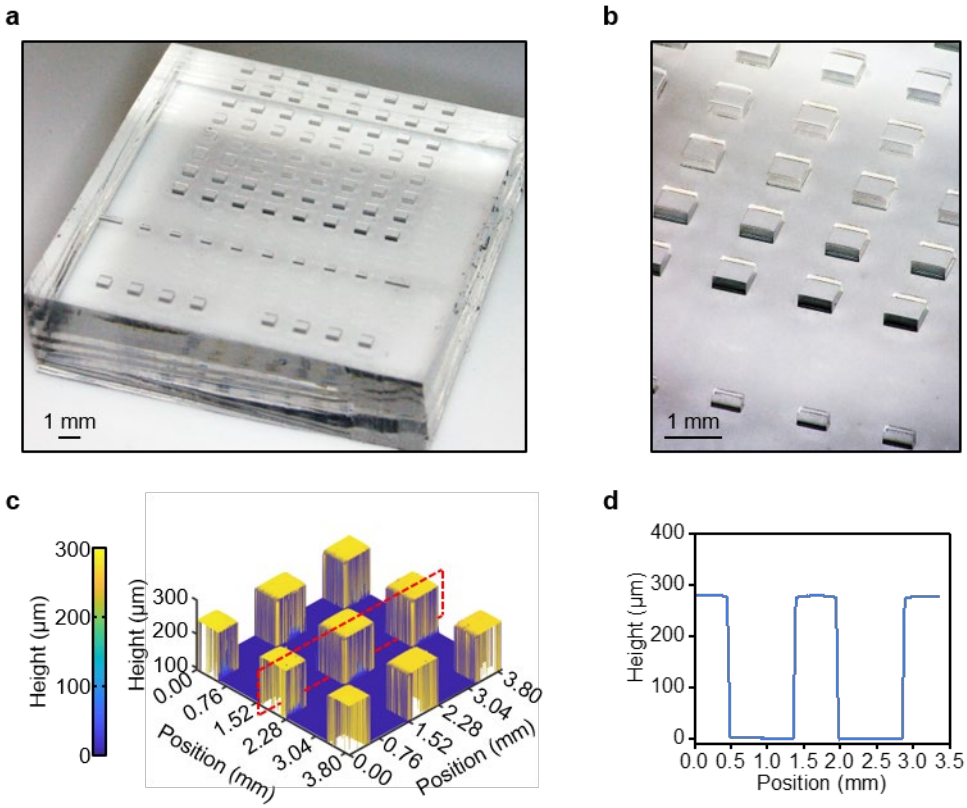

Supplementary Figure 7. PDMS stamp for stacking the electrode array and temperature sensor array. a,b, Optical images of the PDMS stamp. **c,** Height distribution of the PDMS stamp measured using a 3D Optical Profiler. **d,** Height distribution of the PDMS stamp along the red dashed box in (**c**).

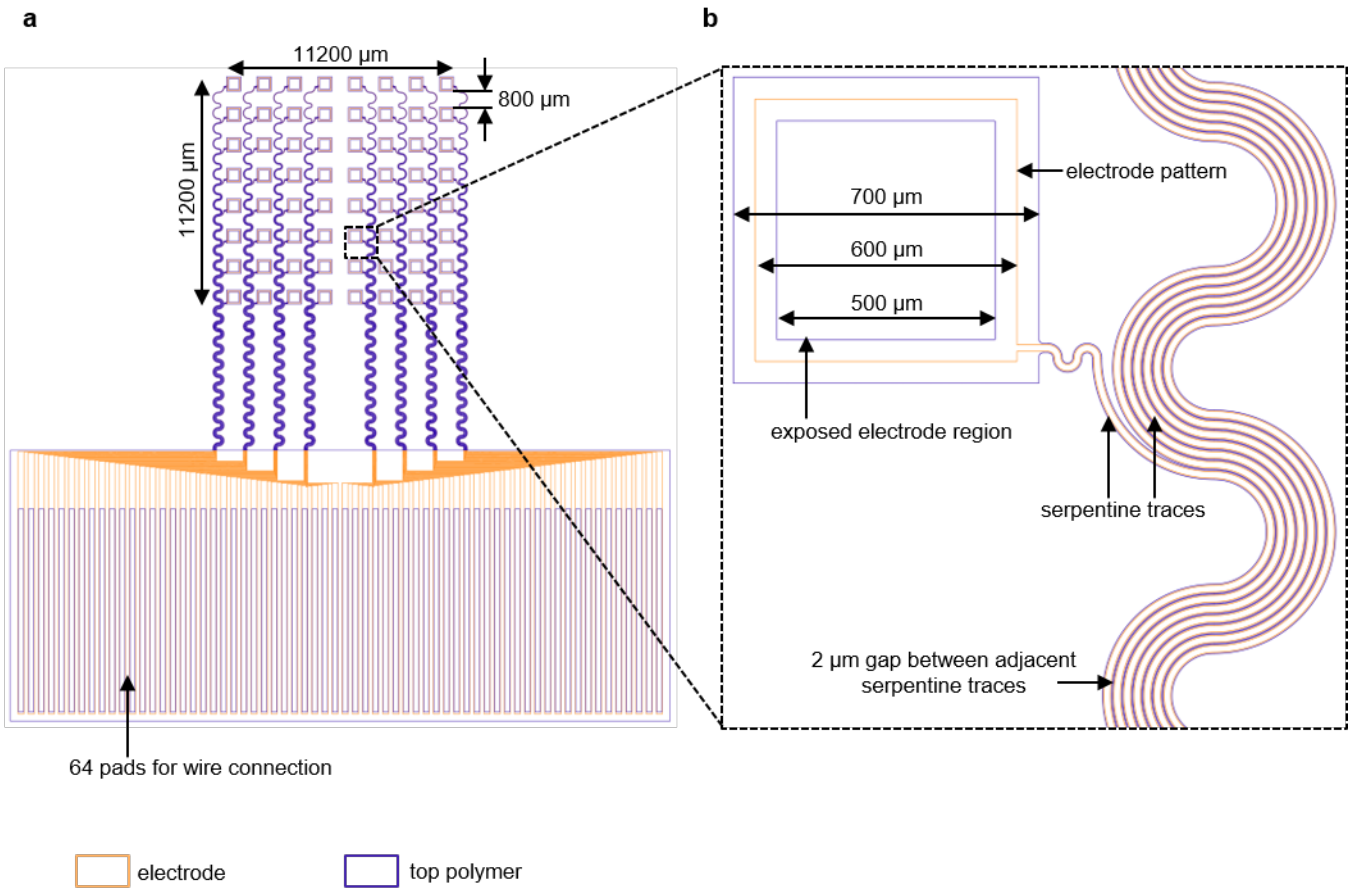

Supplementary Figure 8. Layout of the electrode array. a, An 8 by 8 array. **b,** A unit cell.

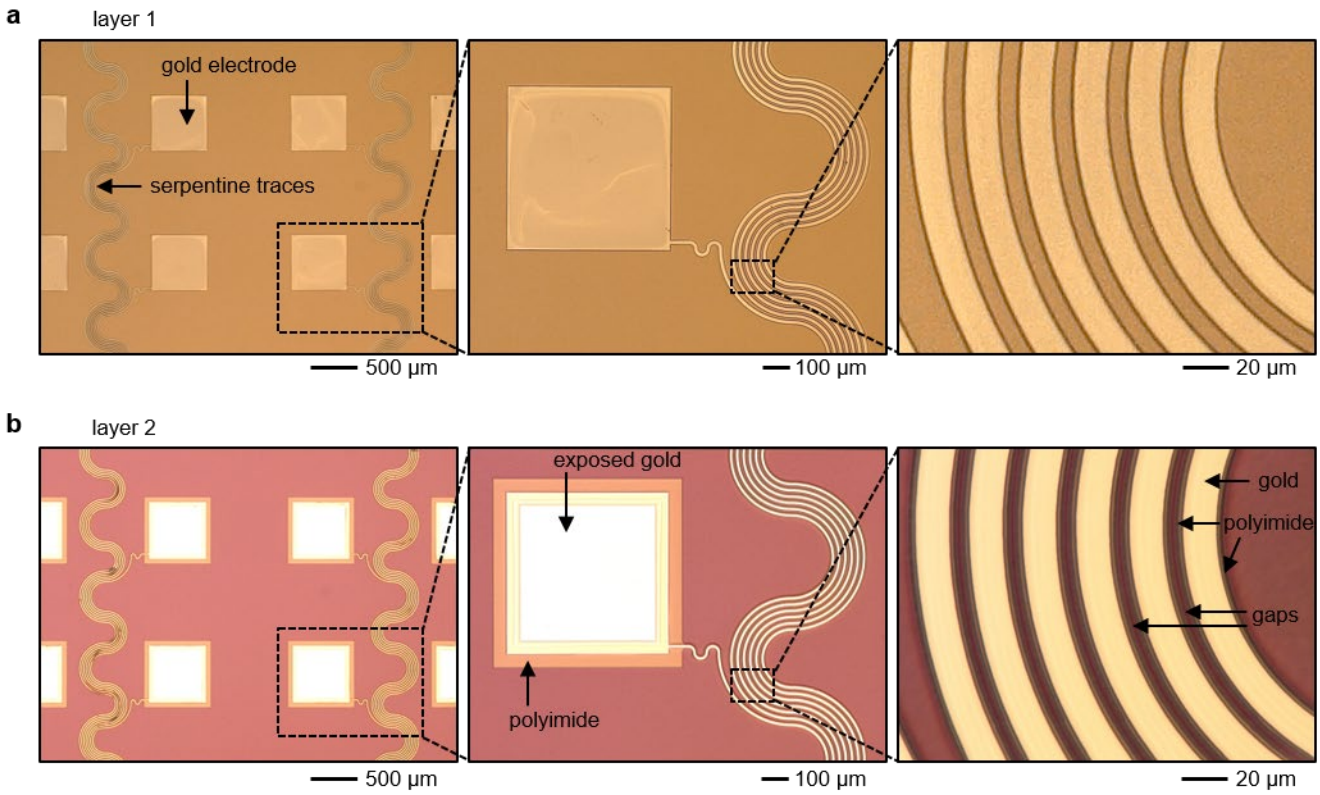

Supplementary Figure 9. Optical images of the electrode array at different stages of the fabrication. a, Layer of electrodes. **b,** Layer of polymer.

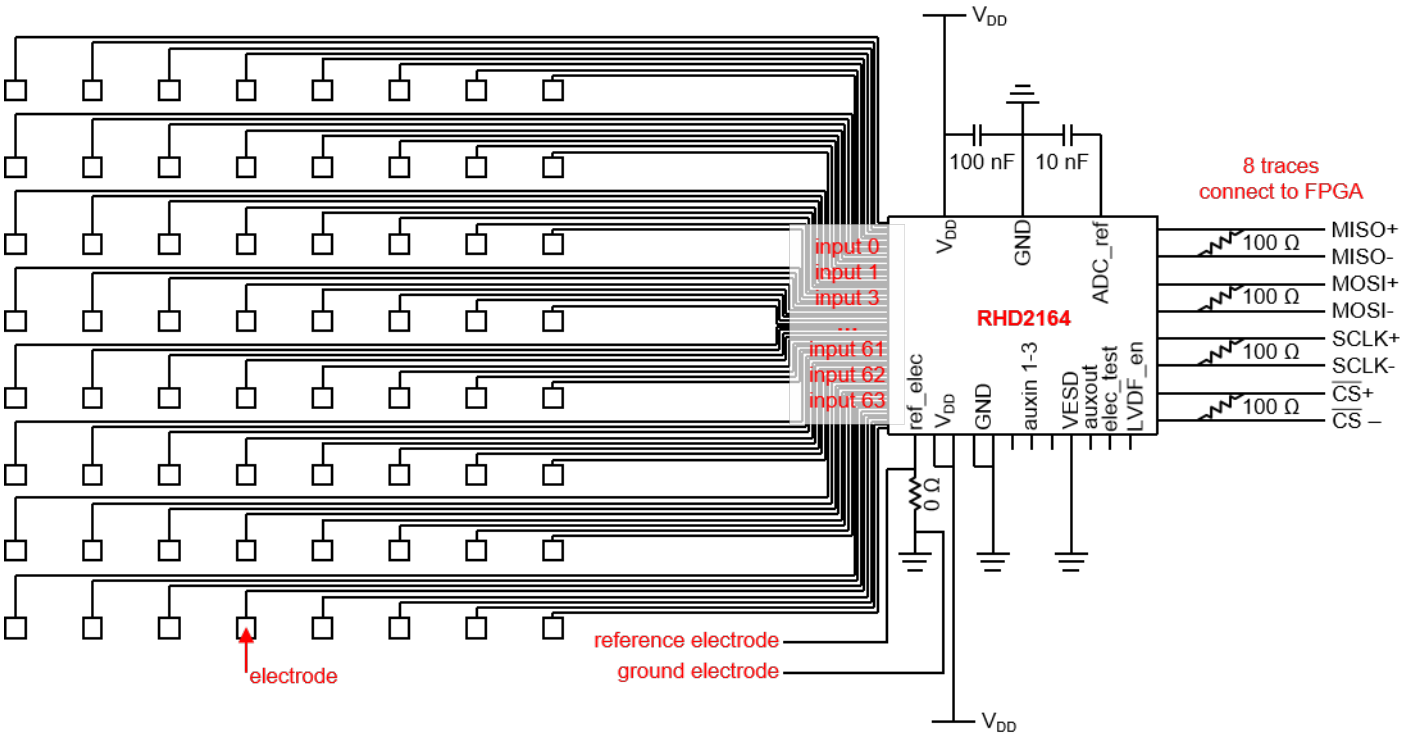

Supplementary Figure 10. Multiplexing circuit for the 8 by 8 electrode array.

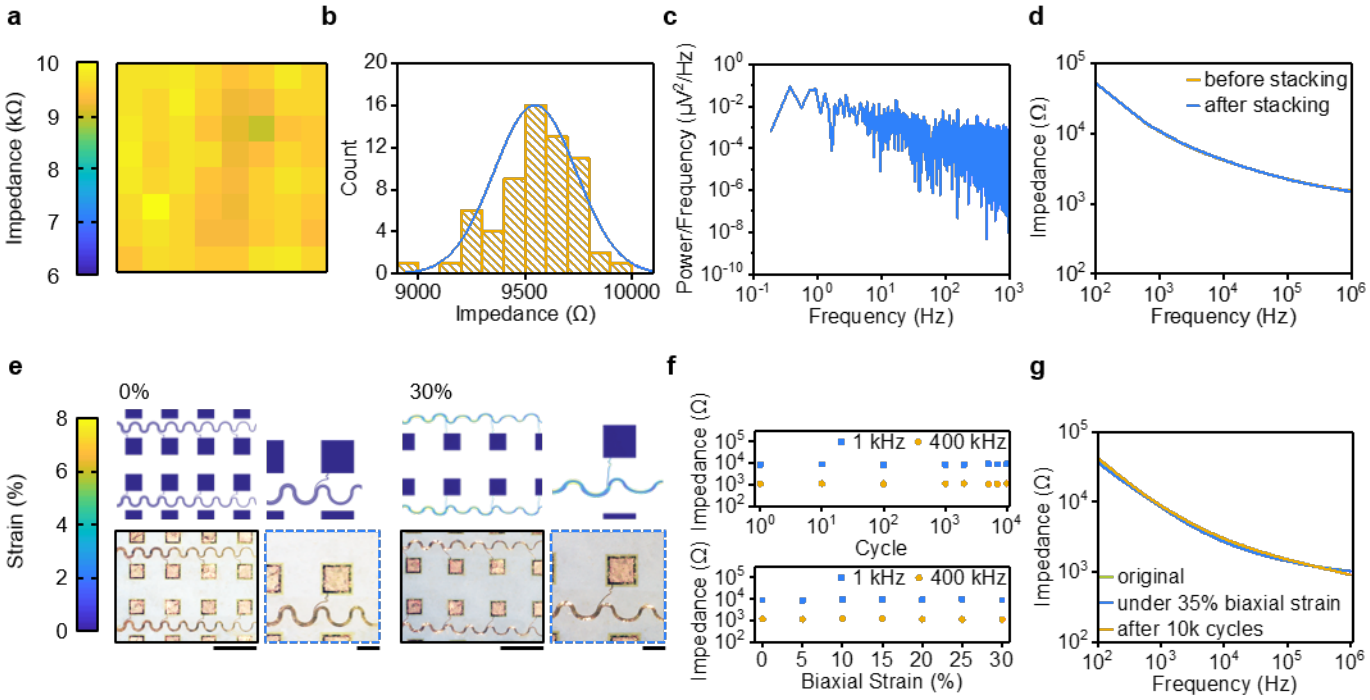

Supplementary Figure 11. Characterizations of the electrode array. a, Spatial map of the impedances of the electrode array at 1 kHz in 0.1 M phosphate-buffered saline (PBS) at room temperature (RT). **b,** Histogram and Gaussian lineshape fitting of the electrode impedances. **c,** Power spectral density of the noise signal from the electrode. **d,** Impedance spectra of the electrode before and after stacking with other functional layers. **e,** FEA results (top) and optical images (bottom) of the electrode array under biaxial strains of 0% and 30%. **f,** Impedance of the electrode under cyclic 20% uniaxial stretching (top) and different biaxial strains (bottom). **g,** Impedance spectra of the electrode at various conditions. Scale bars, 2 mm for the images in black squares, 500 μm for images in blue dashed squares.

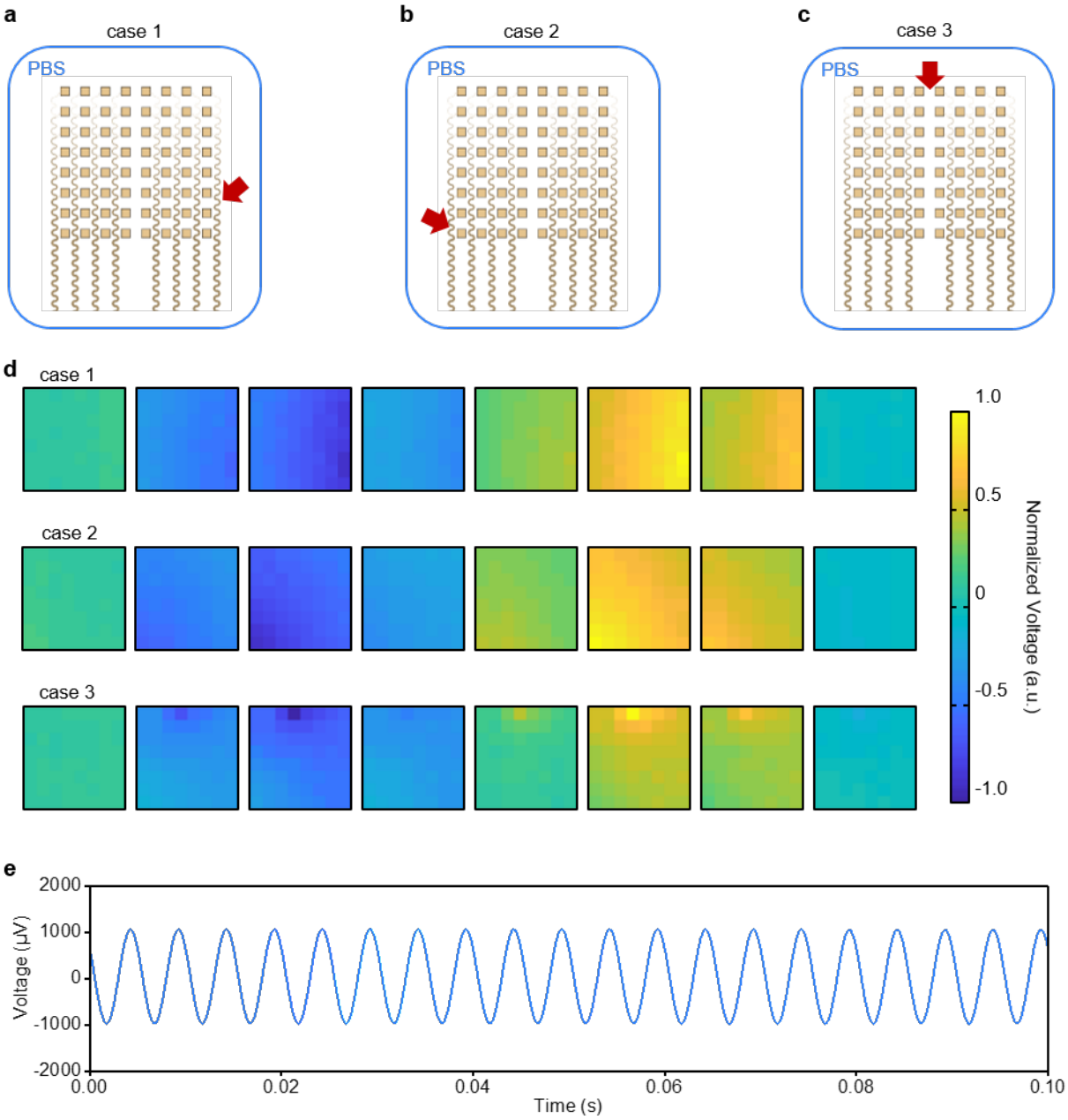

Supplementary Figure 12. Mapping performance of the electrode array in PBS (0.1 M), demonstrating the 100% yield of the device. a-c, Schematic illustrations of the setup. Red arrows indicate the positions of the electrodes with input signals (sinusoidal wave, 200 Hz). **d,** Corresponding normalized electrical mapping results at different time points. Frame interval: 0.75 ms. **e,** Time-domain response of a electrode to the input signal.

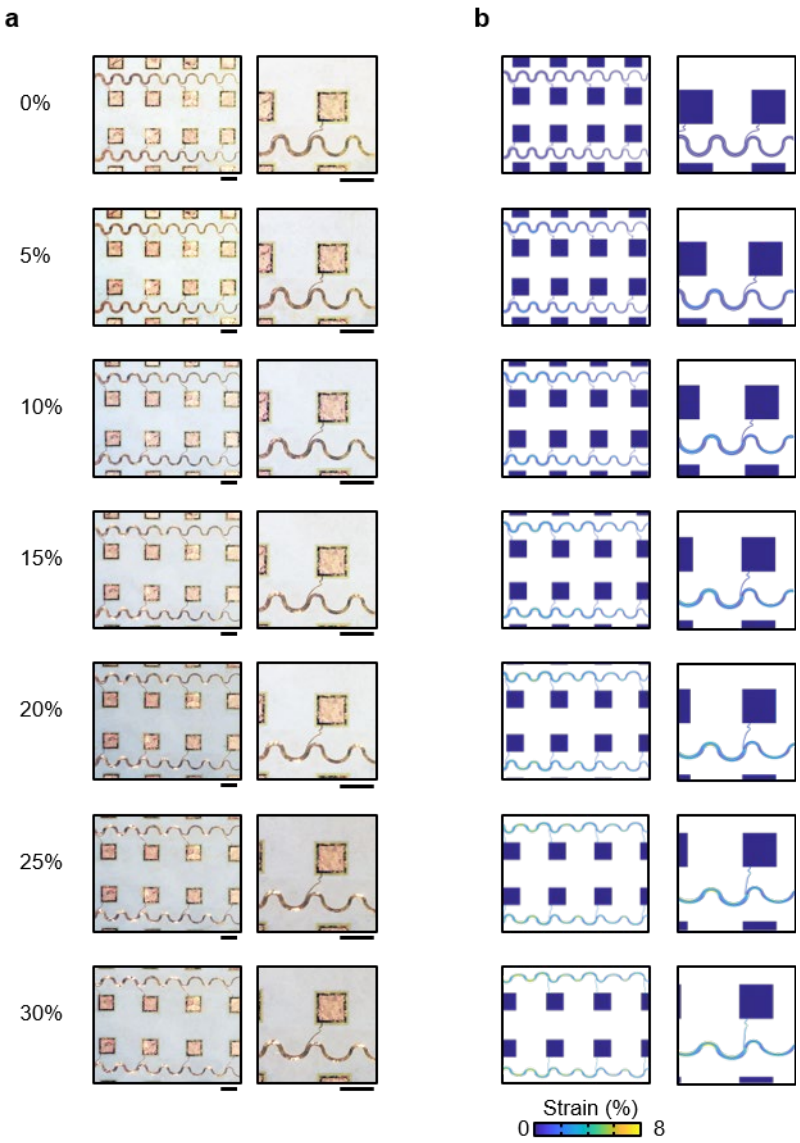

Supplementary Figure 13. Electrode array under biaxial stretching. a, Optical images. **b,** FEA results. Scale bars, 700 μm.

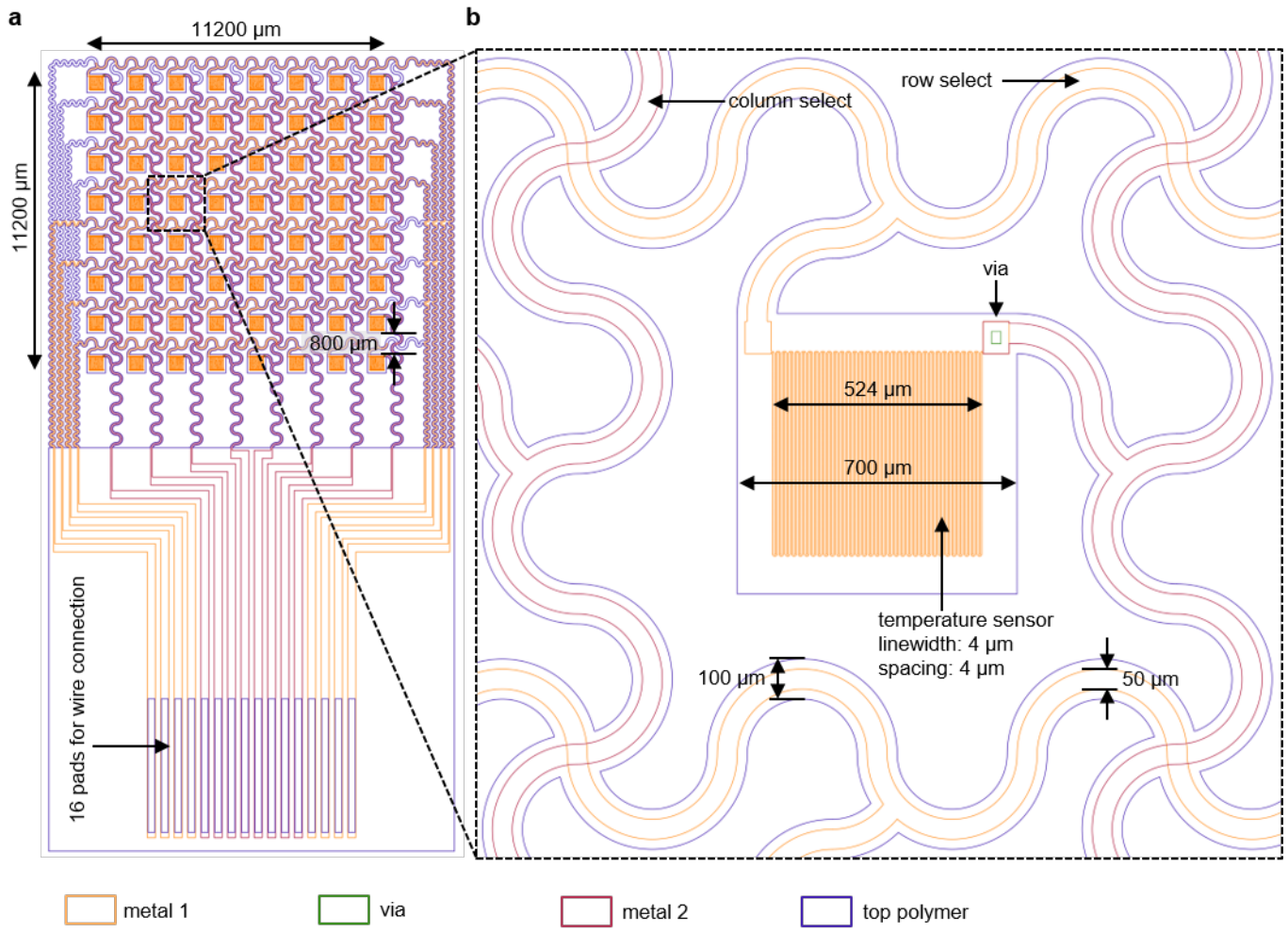

Supplementary Figure 14. Layout of the temperature sensor array. a, An 8 by 8 array. **b,** A unit cell.

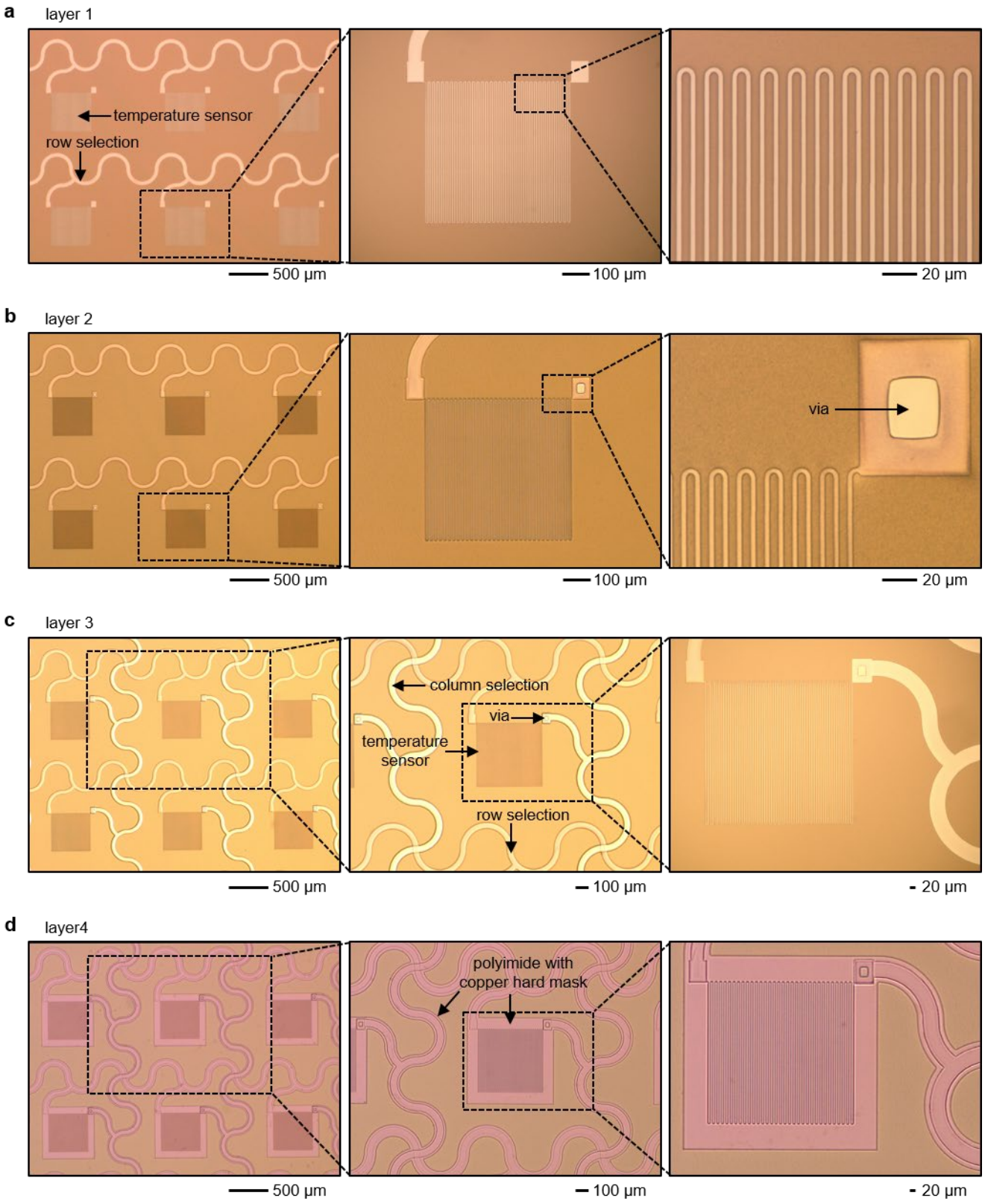

Supplementary Figure 15. Optical images of the temperature sensor array at different stages of the fabrication. a, Layer of temperature sensors and row selection lines. **b,** Layer of via. **c,** Layer of column selection. **d,** Layer of polymer.

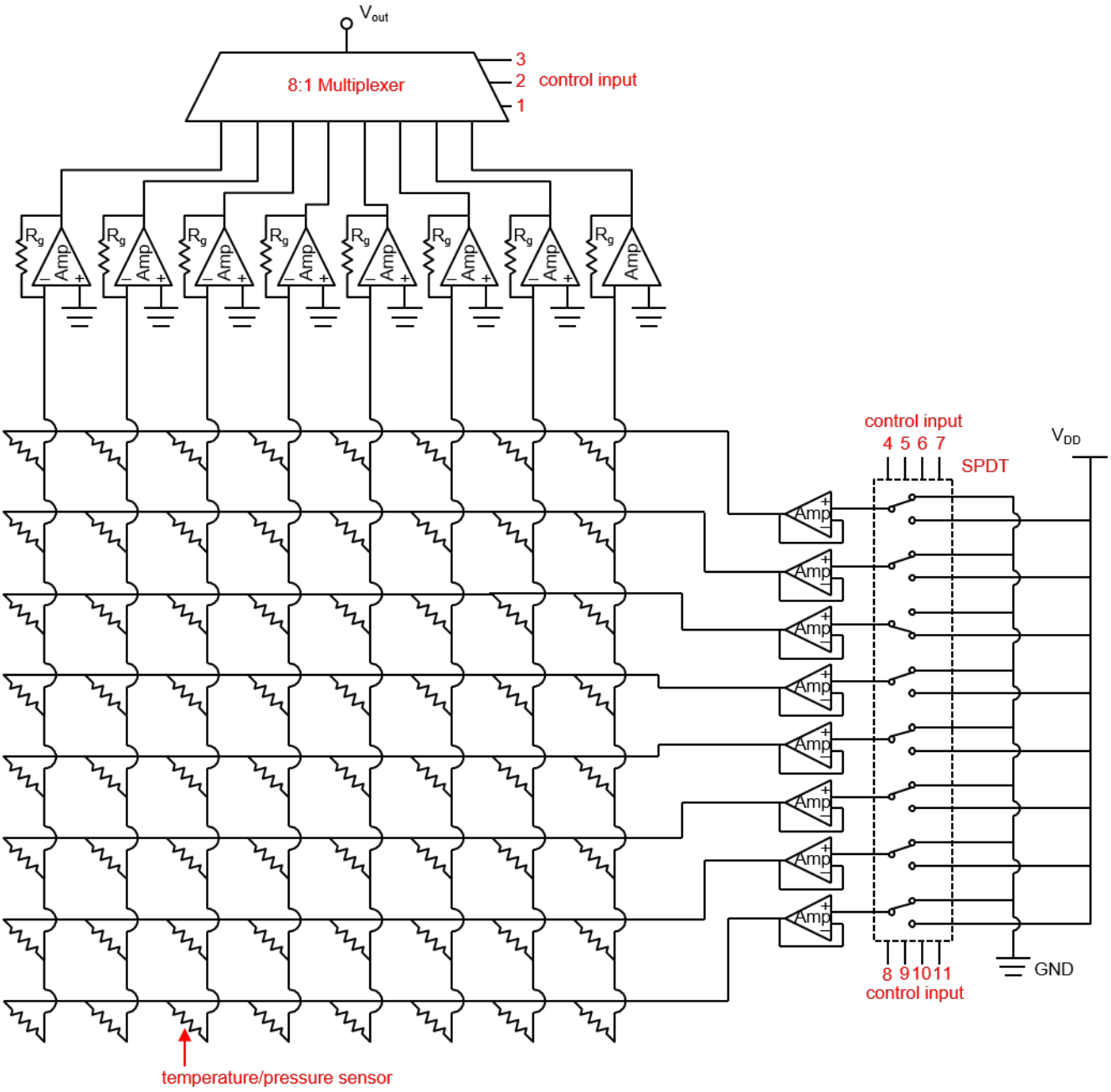

Supplementary Figure 16. Multiplexing circuit for the 8 by 8 temperature and pressure sensor arrays.

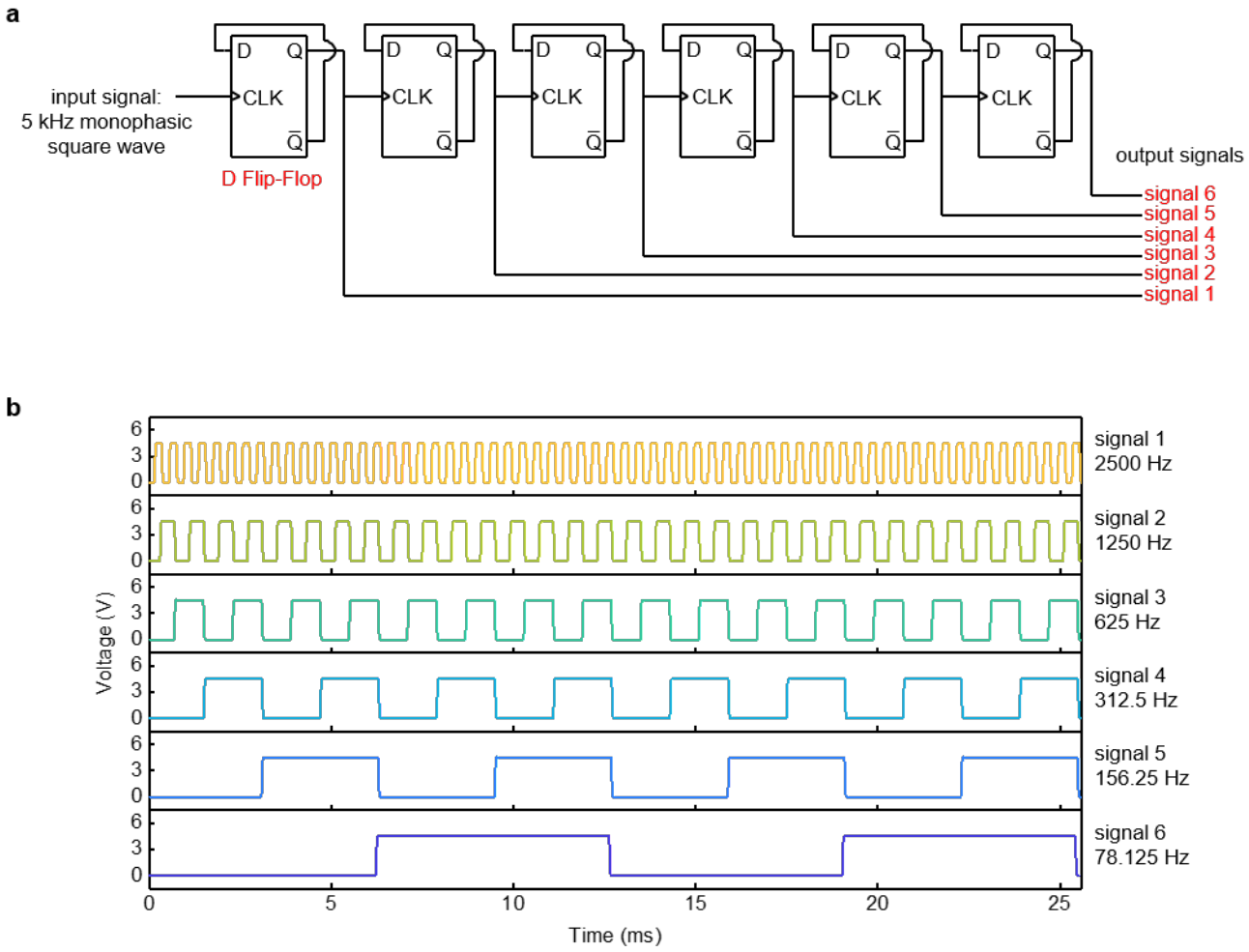

Supplementary Figure 17. Control input for the multiplexers. a, Circuit diagram. **b,** Waveforms of the output signals.

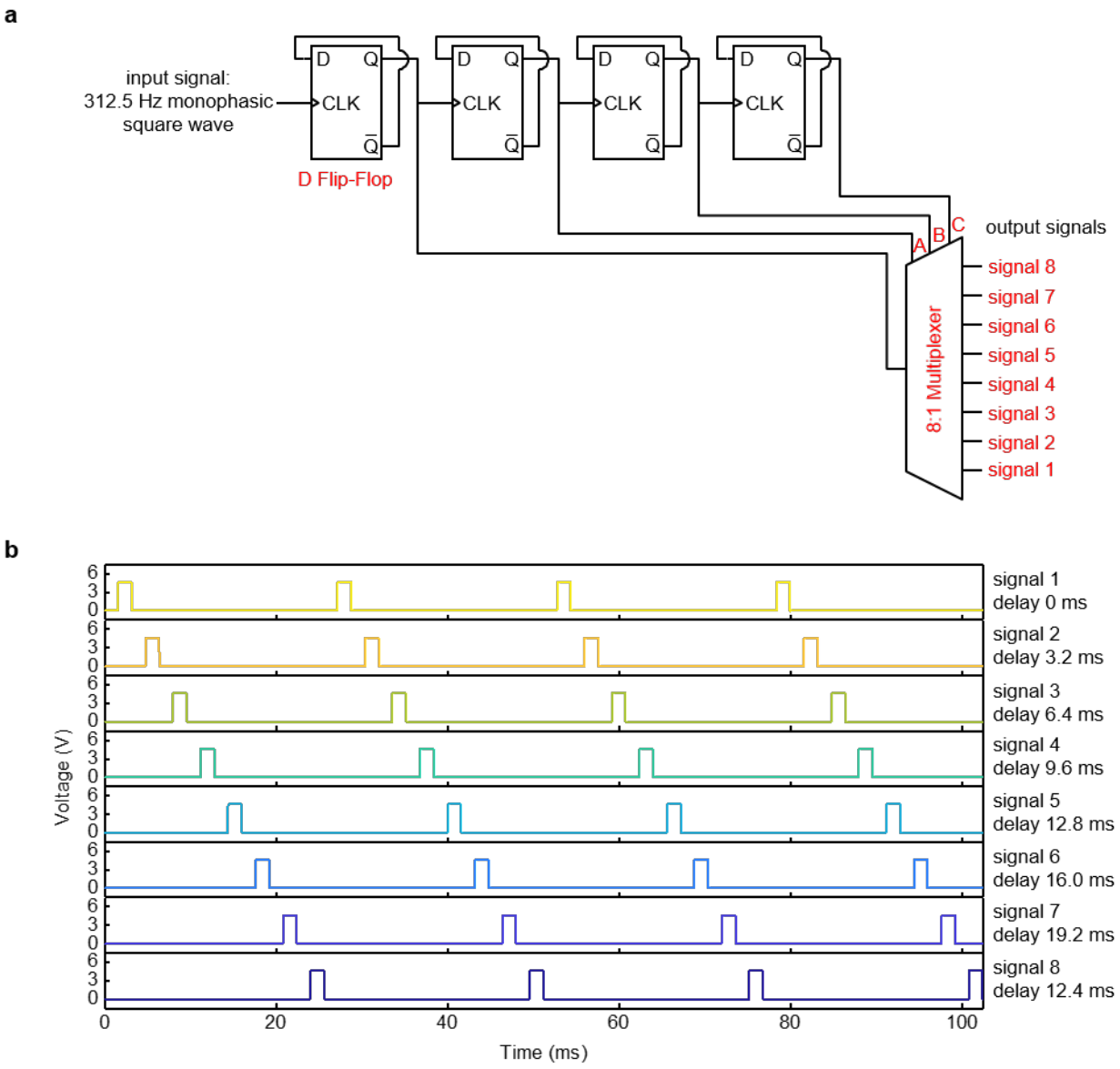

Supplementary Figure 18. Control input for the single pole double throw (SPDT) switches. a, Circuit diagram. **b,** Waveforms of the output signals.

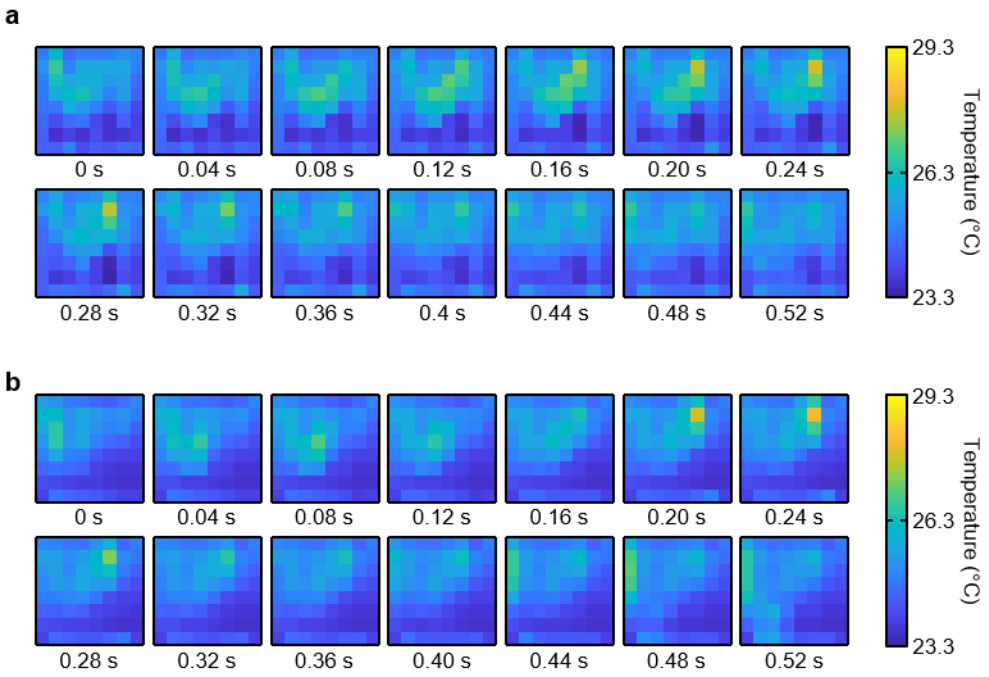

Supplementary Figure 19. Temperature mapping with proper grounding to eliminate the crosstalk. a, Temperature distribution measured from the 8 by 8 temperature sensor array. **b,** Temperature distribution measured from an IR camera.

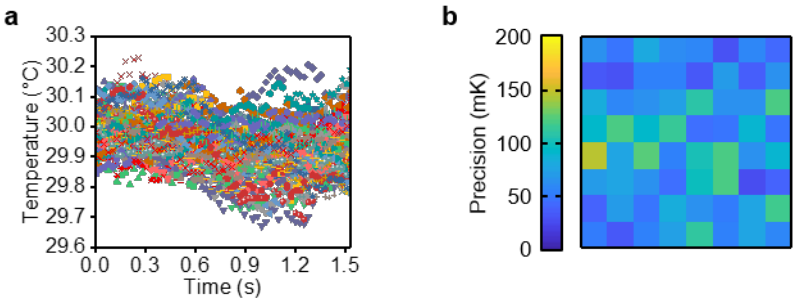

Supplementary Figure 20. Measurement precision associated with the temperature sensor array. a, Responses of the sixty-four temperature sensors on a hotplate. Standard deviation ranges from ~24 to ~147 mK. **b,** Precision map of the temperature sensors, calculated from the standard deviation of 61 points.

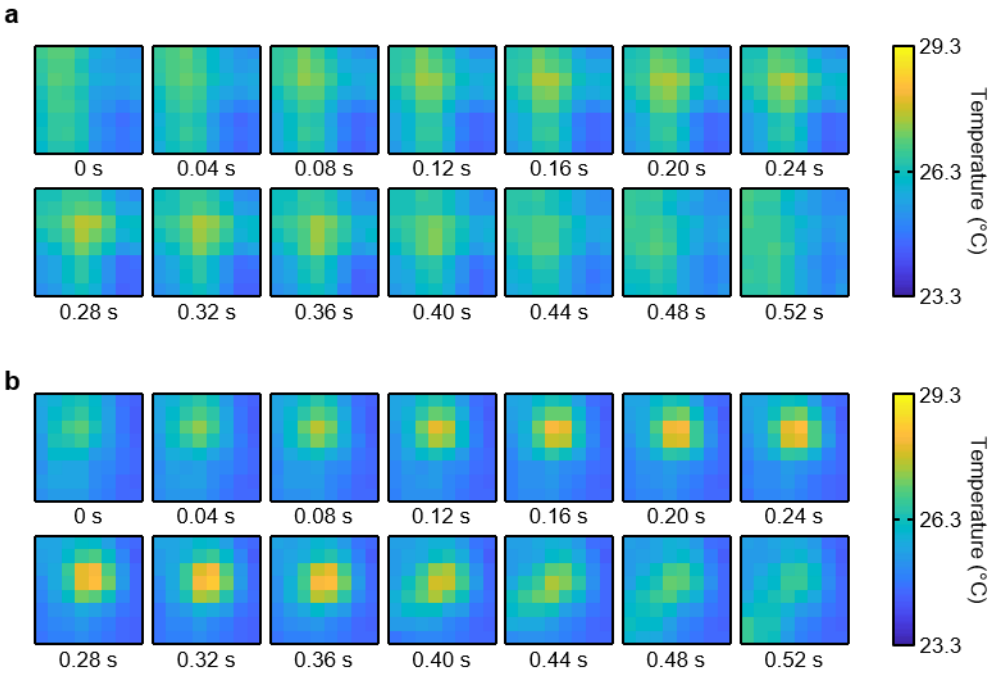

Supplementary Figure 21. Temperature mapping from the circuit with crosstalk. a, Temperature distribution measured from the 8 by 8 temperature sensor array. **b,** Temperature distribution measured from an IR camera.

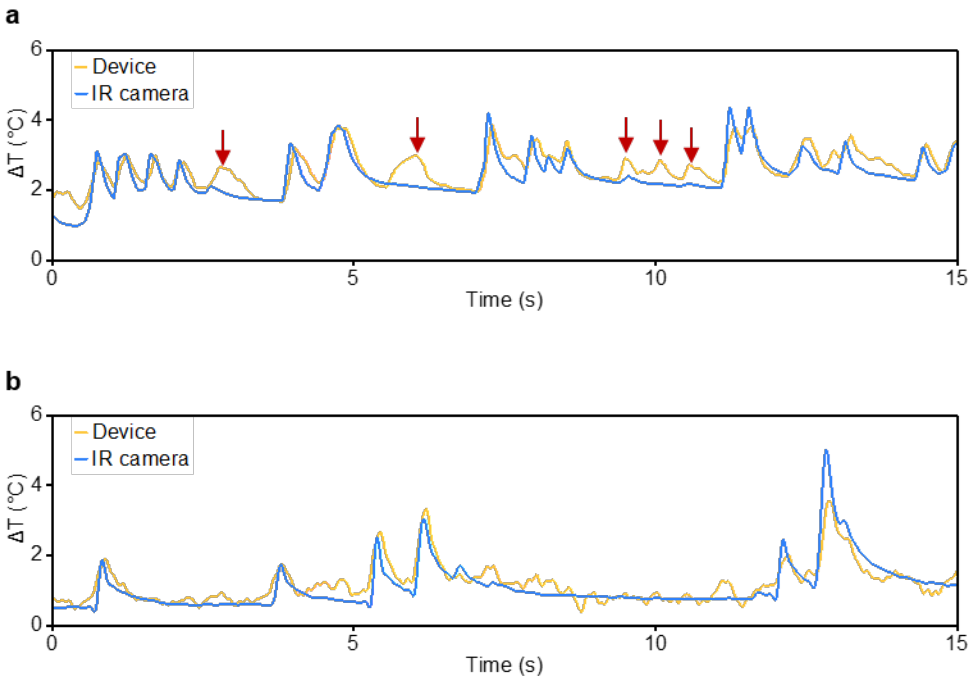

Supplementary Figure 22. Comparison of the results from the infrared camera and the stretchable temperature sensor array. a, Results from the circuit with crosstalk. Red colors indicate inaccurate temperature increase due to the crosstalk. **b,** Results from the circuit with proper grounding to eliminate the crosstalk.

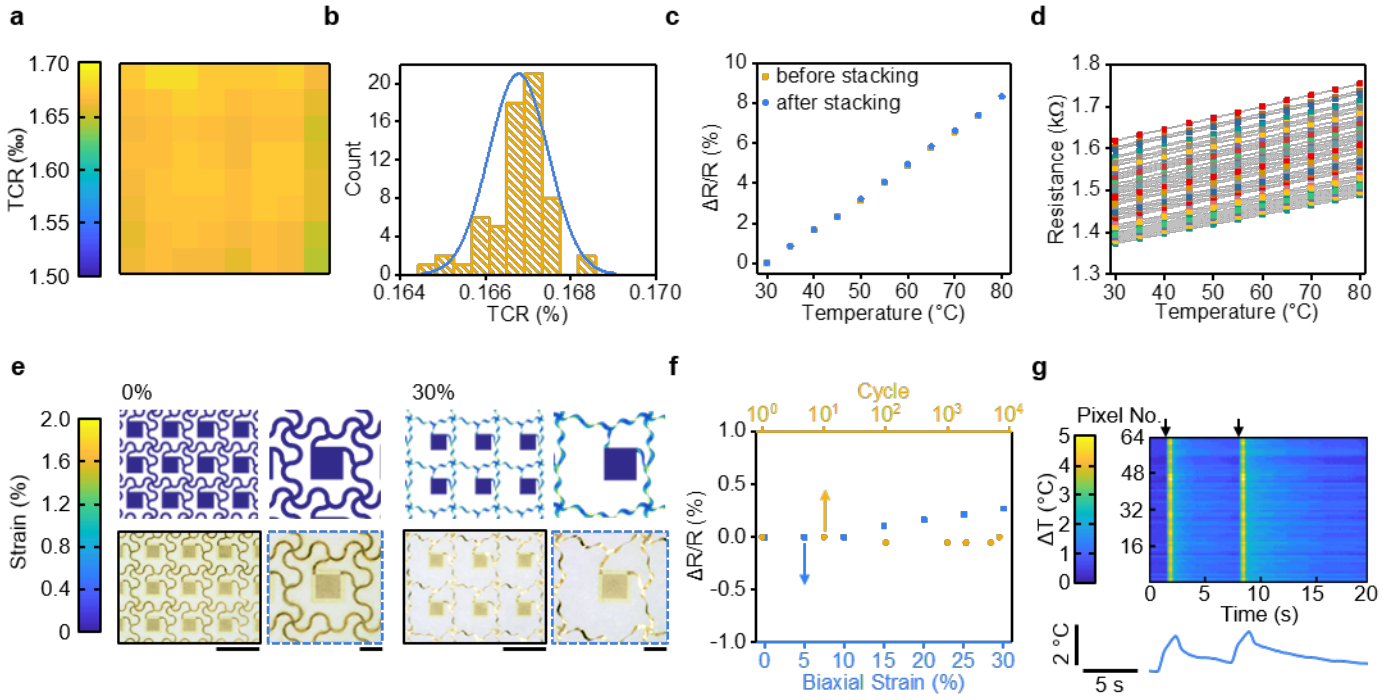

Supplementary Figure 23. Characterization results for the temperature sensor array. a, Spatial map of the TCRs of the temperature sensors in the array. **b,** Histogram and Gaussian lineshape fitting of the TCRs. **c,** Fractional change of resistance of the temperature sensor at different temperatures before and after stacking with other functional layers. **d,** Resistances of the sixty-four temperature sensors at temperatures from 30 to 80 °C. **e,** FEA results (top) and optical images (bottom) of the temperature sensor array under biaxial strains of 0% and 30%. **f,** Fractional change of resistance of a temperature sensor under cyclic 20% uniaxial stretching (orange points) and different biaxial strains (blue points). **g,** Responses of the sixty-four temperature sensors under hot air (top), and time-domain temperature curve of a single temperature sensor (bottom). Black arrows indicate the application of hot air. Scale bars, 2 mm for the images in black squares, 500 μm for images in blue dashed squares.

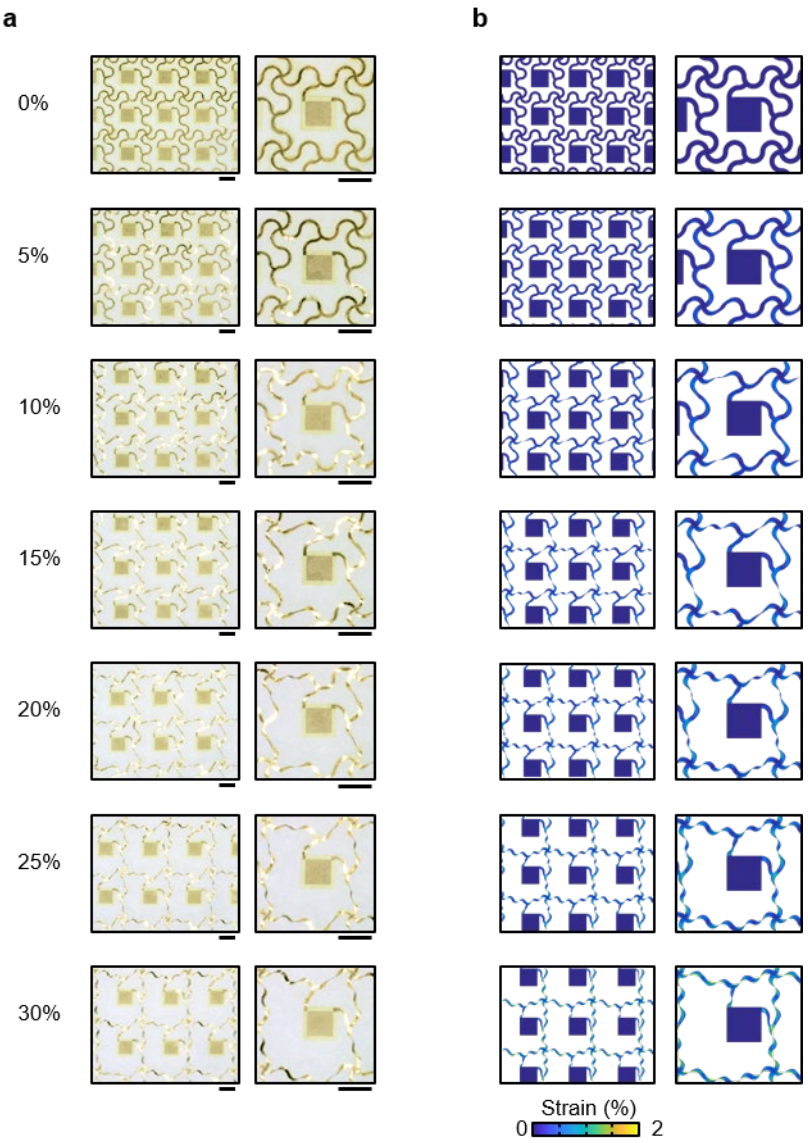

Supplementary Figure 24. Temperature sensor array under biaxial stretching. a, Optical images. **b,** FEA results. Scale bars, 700 μm.

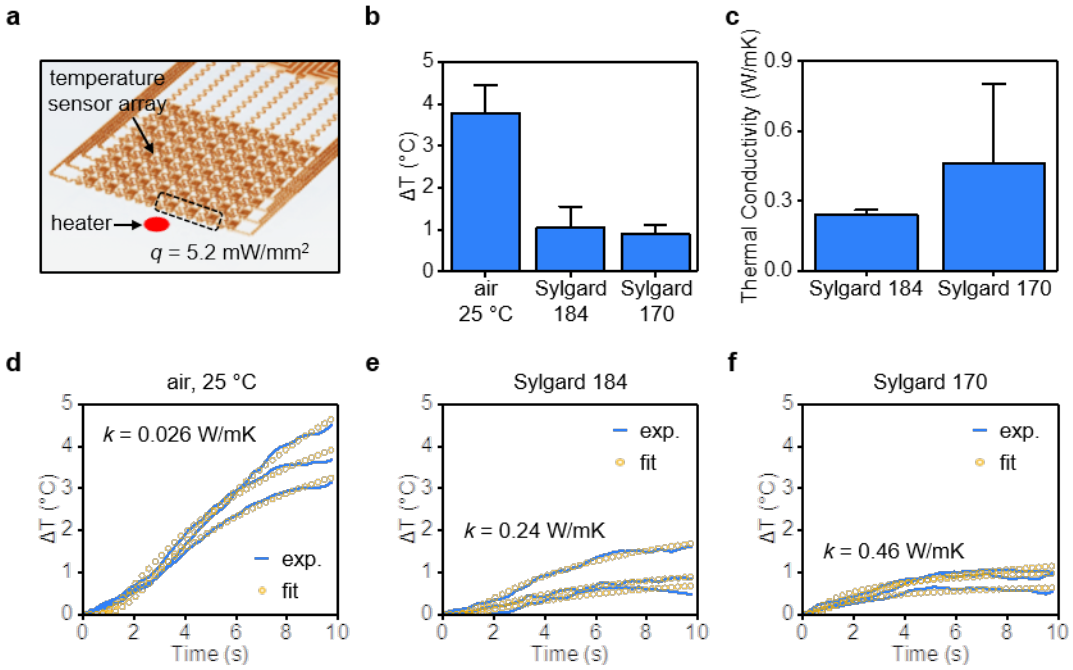

Supplementary Figure 25. Assessment of thermal conductivities using a heater and the arrays of temperature sensors. **a,** Schematic illustration of the setup. **b,** Averaged temperature change (ΔT) at 10 s when placing the temperature sensor array in air and laminating layers of silicone (Sylgard 184 and Sylgard 170) onto the array. ΔT is measured from three temperature sensors in the black dashed square in (**a**). **c,** Calculated thermal conductivities (*k*) using transient plane source analysis. Air serves as the reference material with known thermal properties. Fitting the time-domain temperature profiles yield *k* for Sylgard 184 and Sylgard 170. **d-e,** Time-domain temperature profiles in different conditions (temperature sensor array in air (**d**), temperature sensor array laminated with a layer of Sylgard 184 (**e**) and Sylgard 170 (**f**)) measured from the temperature sensors in the black dashed square in (**a**).

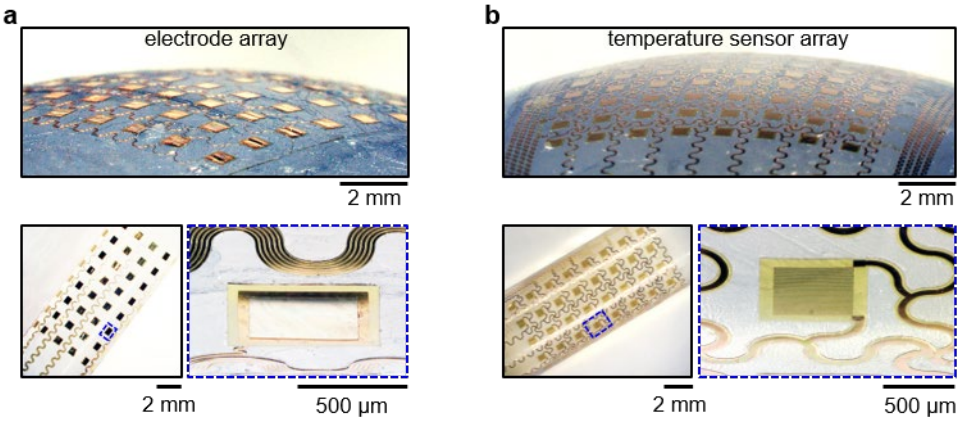

Supplementary Figure 26. Optical images of the arrays on various curvilinear surfaces. a, Electrode array. b, Temperature sensor array.

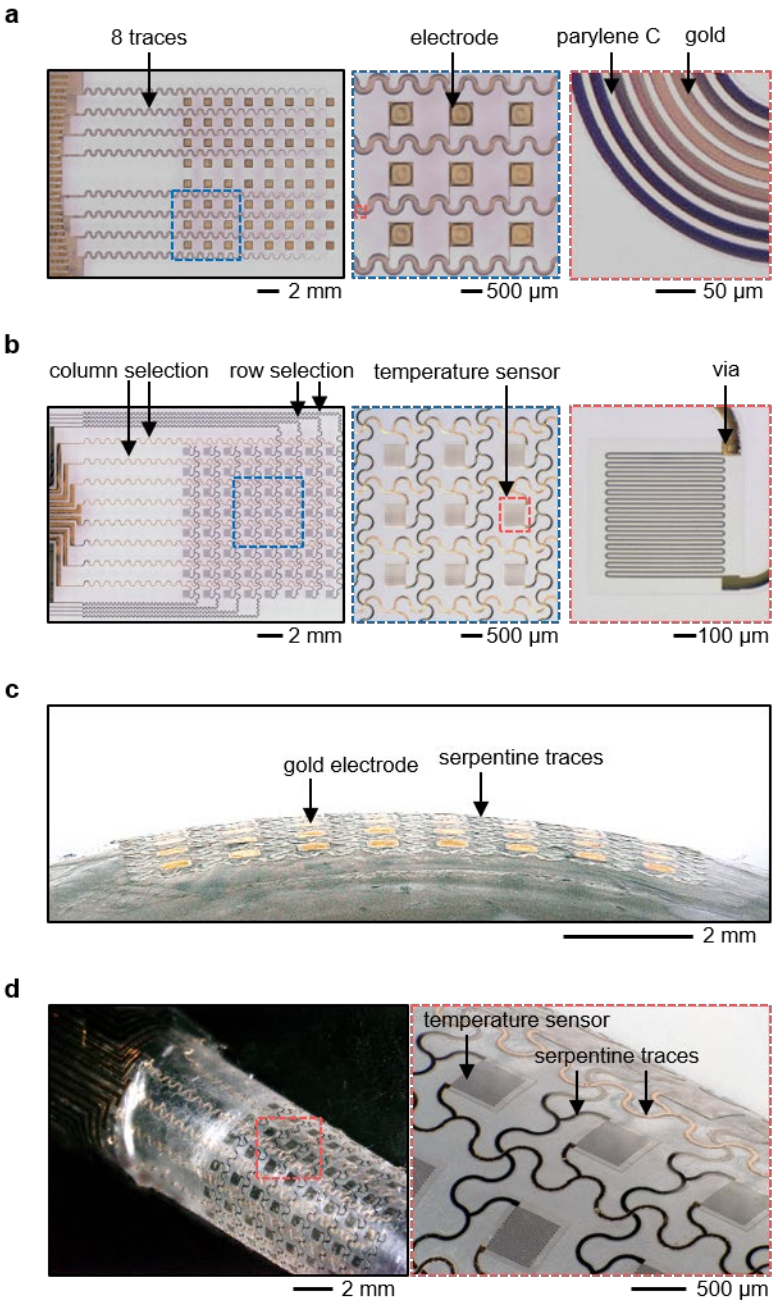

Supplementary Figure 27. Optical images of the parylene-C-based multiplexed devices. a, Electrode array on planar substrate. **b,** Temperature sensor array on planar substrate. **c,** Electrode array on planar curvilinear surface. **d,** Temperature sensor array on curvilinear surface.

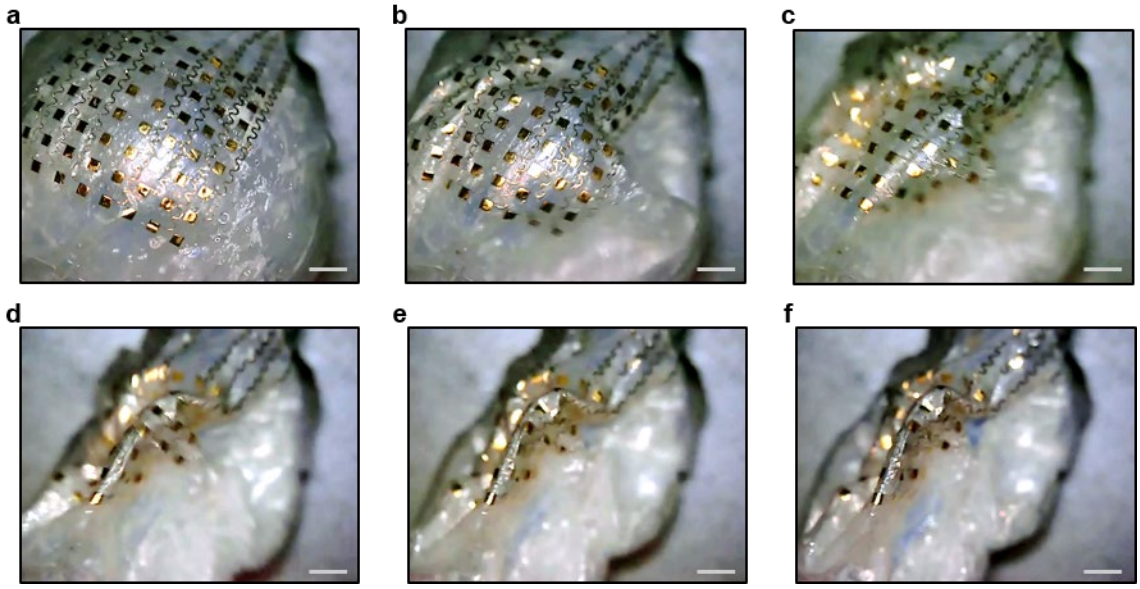

Supplementary Figure 28. Optical images of the electrode array on a commercial balloon catheter in polyurethane. a, Fully inflated. **b,c,** Partially inflated. **d,e,** Partially deflated. **f,** Fully deflated. Scale bars, 2 mm.

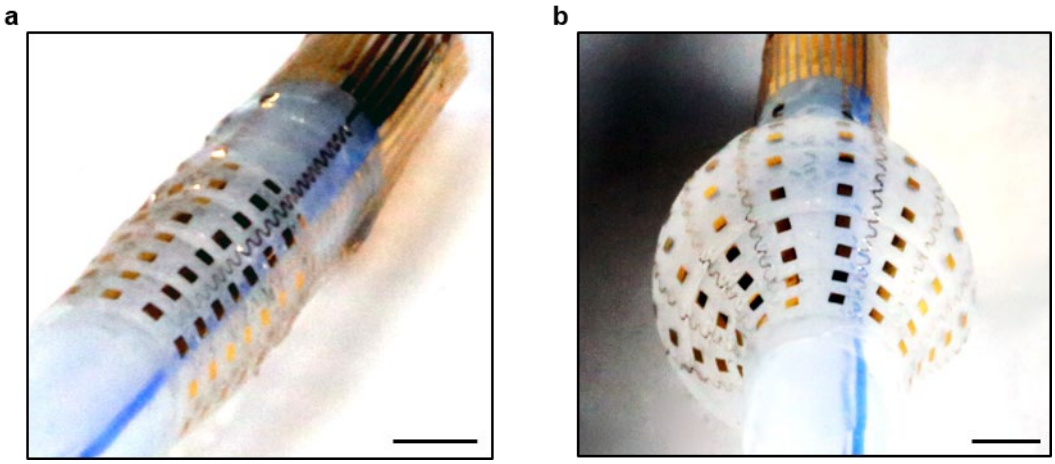

Supplementary Figure 29. Optical images of the electrode array on a commercial balloon catheter in silicone. a, Deflated. **b,** Inflated. Scale bars, 2 mm.

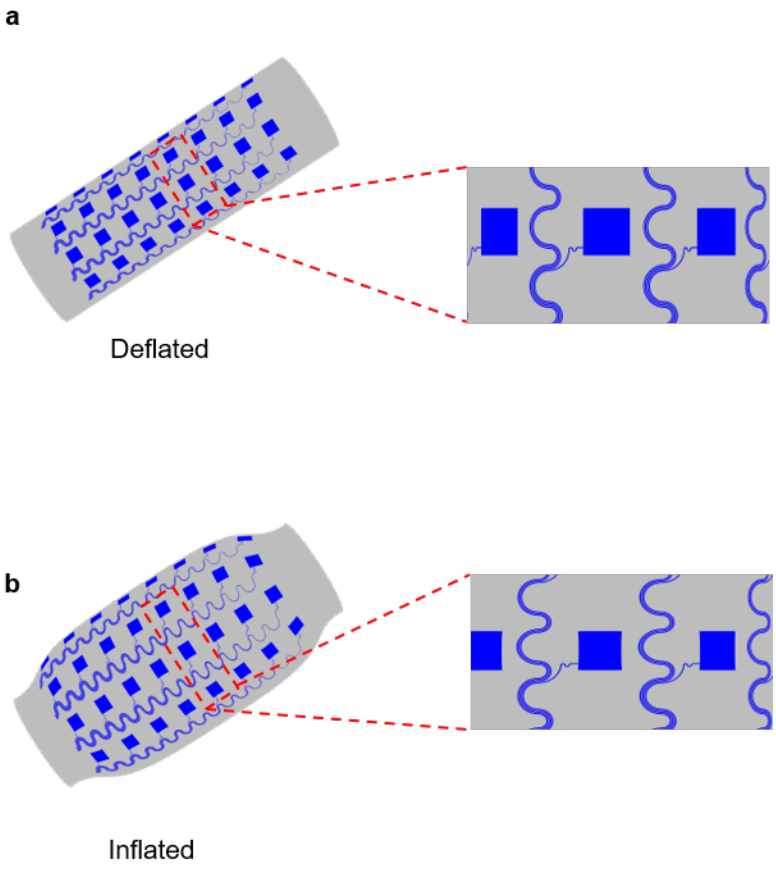

Supplementary Figure 30. FEA results of the balloon in silicone instrumented with an electrode array. a, Deflated. **b,** Inflated.

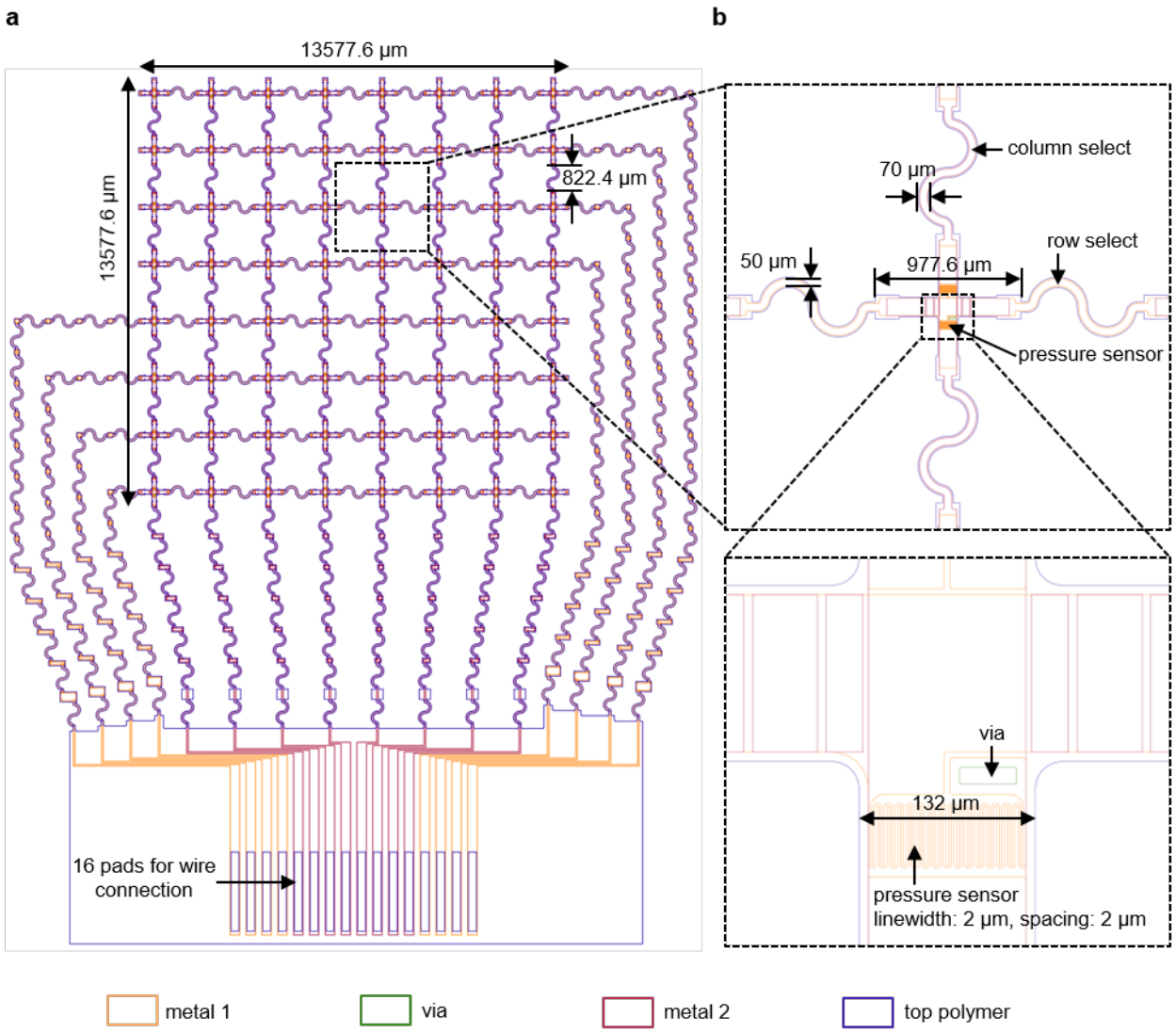

Supplementary Figure 31. Layout of the pressure sensor array. a, An 8 by 8 array. **b,** A unit cell.

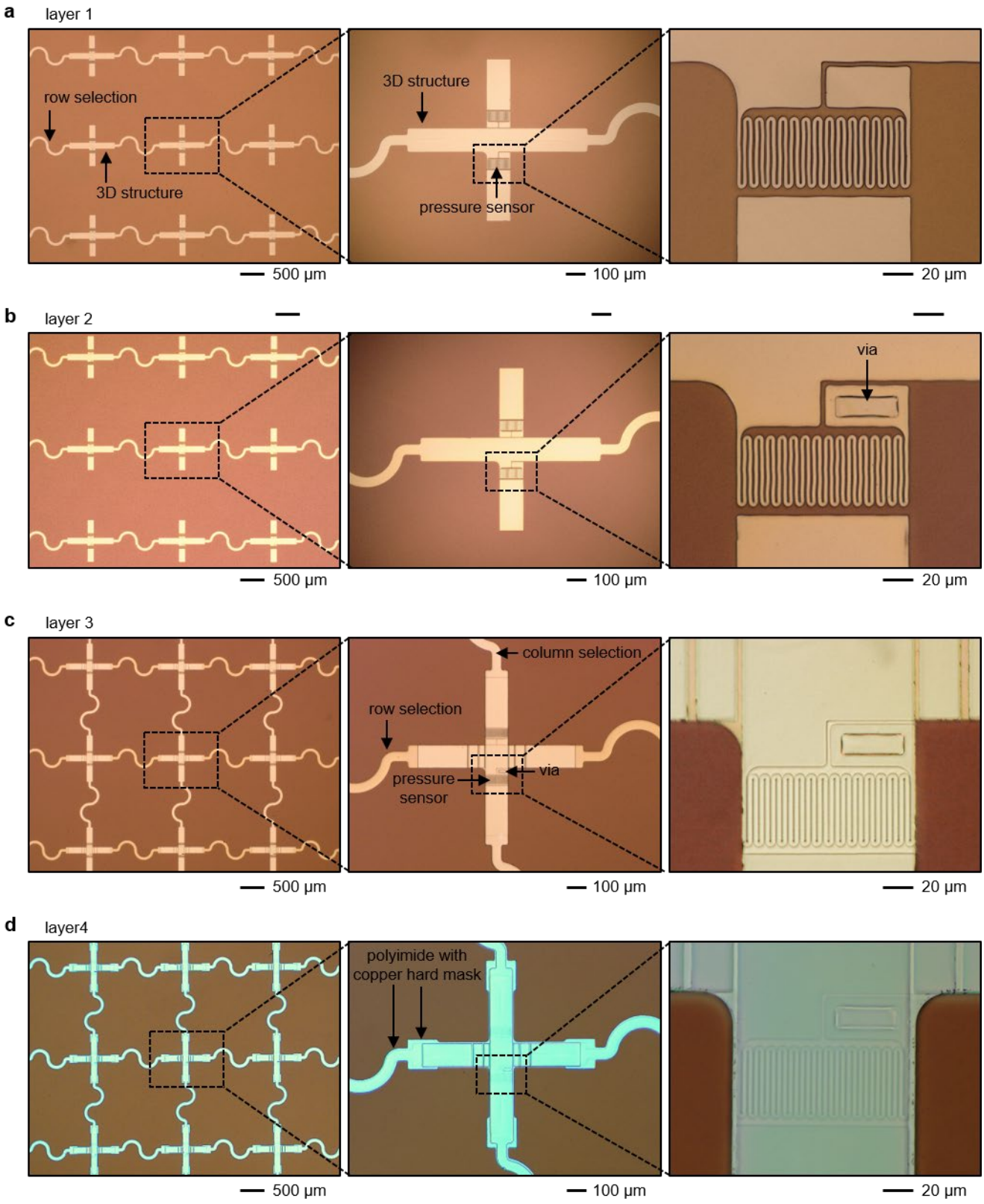

Supplementary Figure 32. Optical images of the pressure sensor array at different stages of the fabrication. a, Layer of temperature sensor and row selection. **b,** Layer of via. **c,** Layer of column selection. **d,** Layer of polymer.

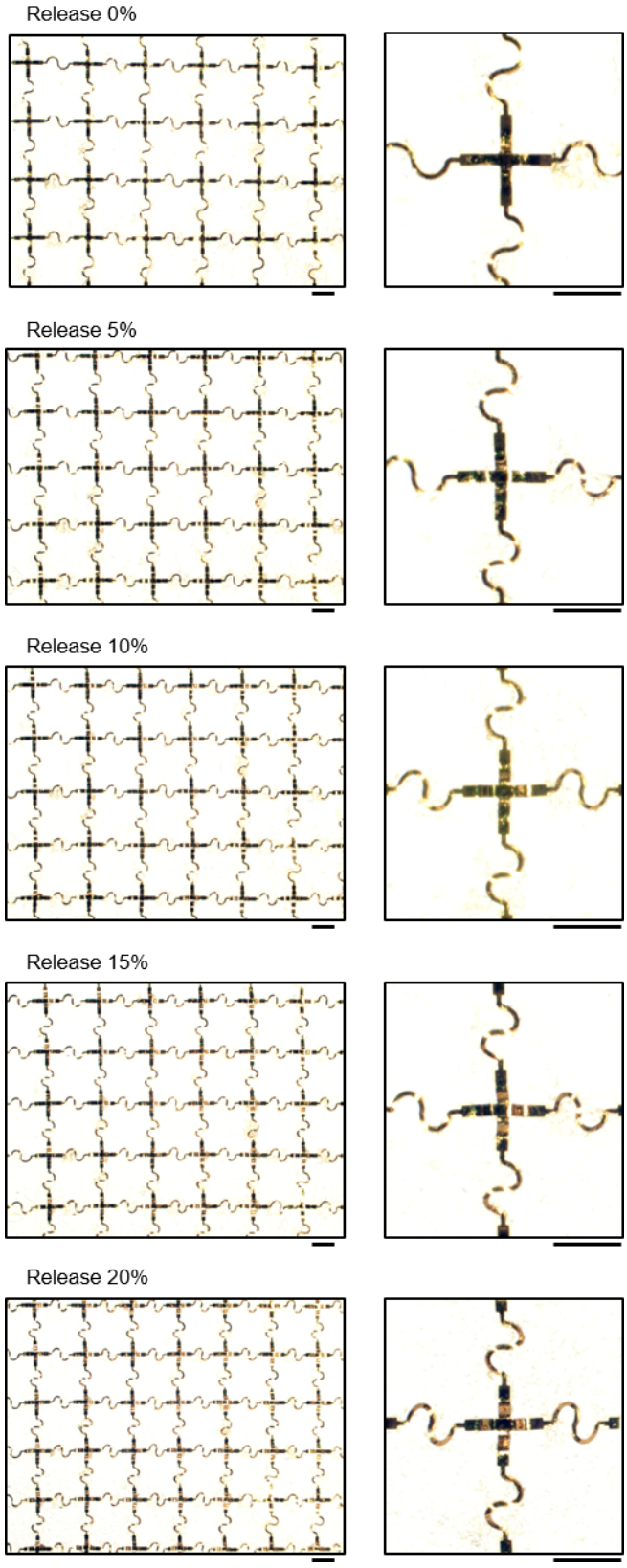

Supplementary Figure 33. Optical images of the pressure sensor array during the compressive buckling process. Scale bars, 700 μm.

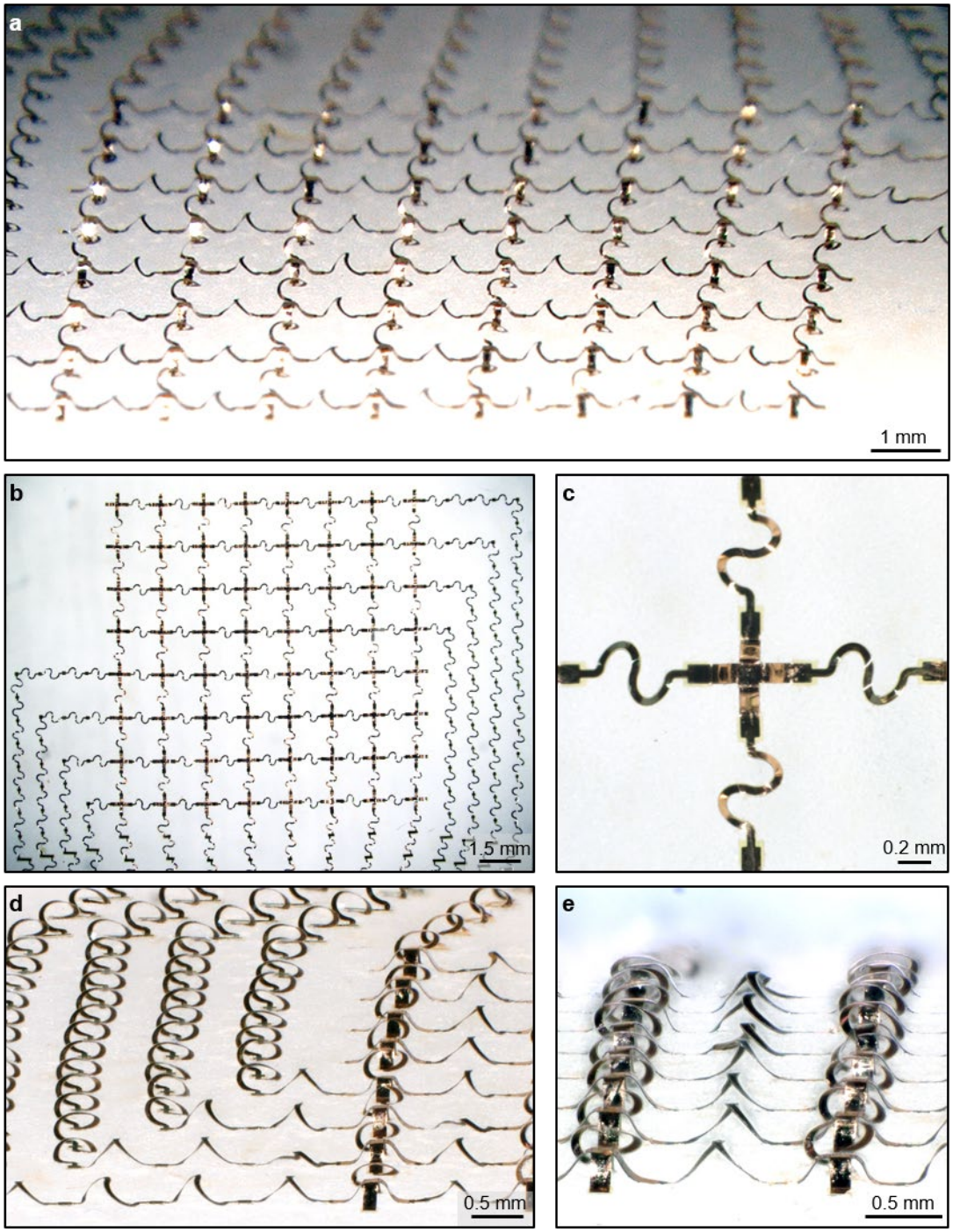

Supplementary Figure 34. Optical images of the pressure sensor array before attaching silicon cavities. a, Tilted view of the array. **b,** Top view of the array. **c,** Top view of one device. **d,e,** The 3D helical interconnects.

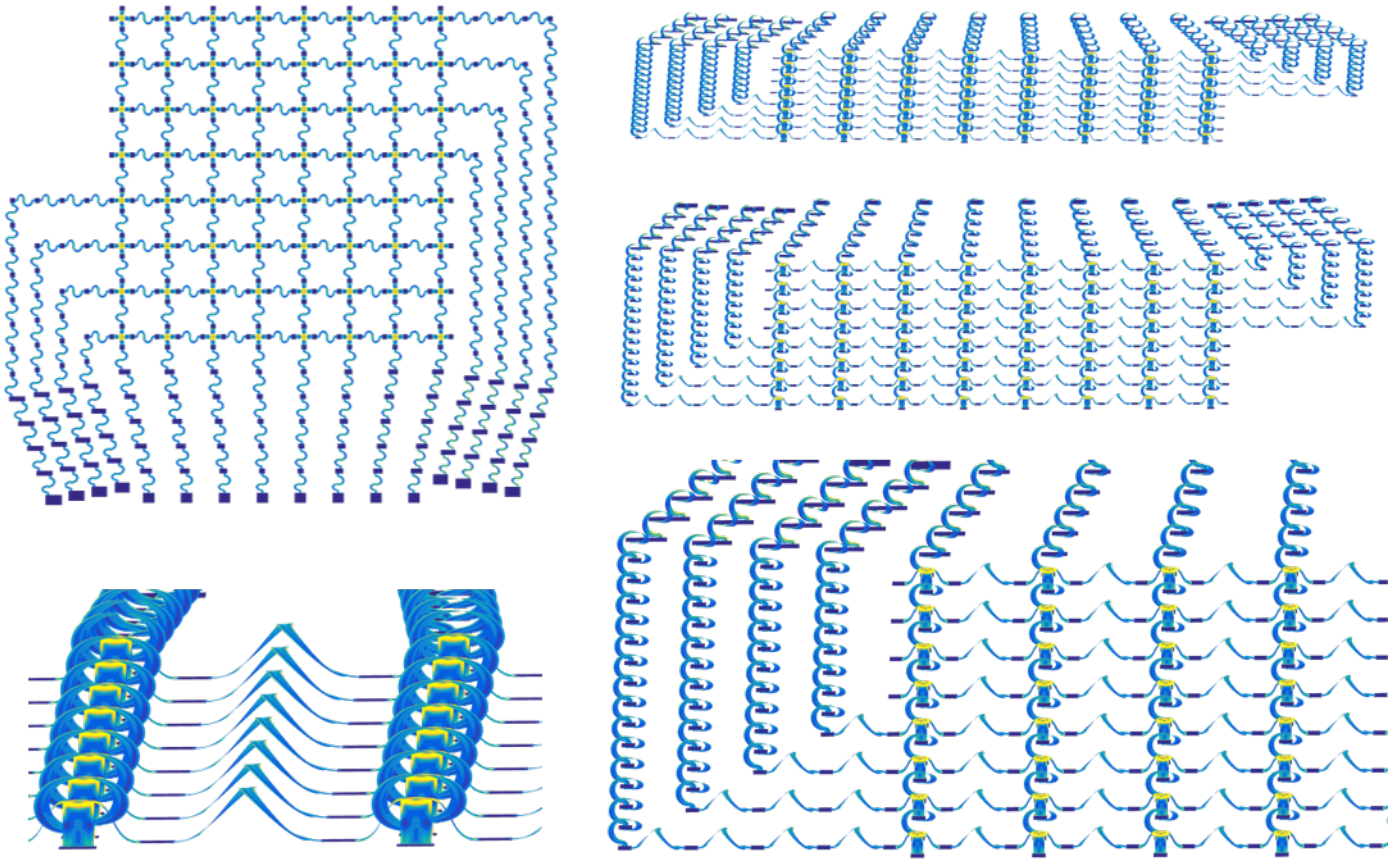

Supplementary Figure 35. FEA results of the 3D structures in the pressure sensor array.

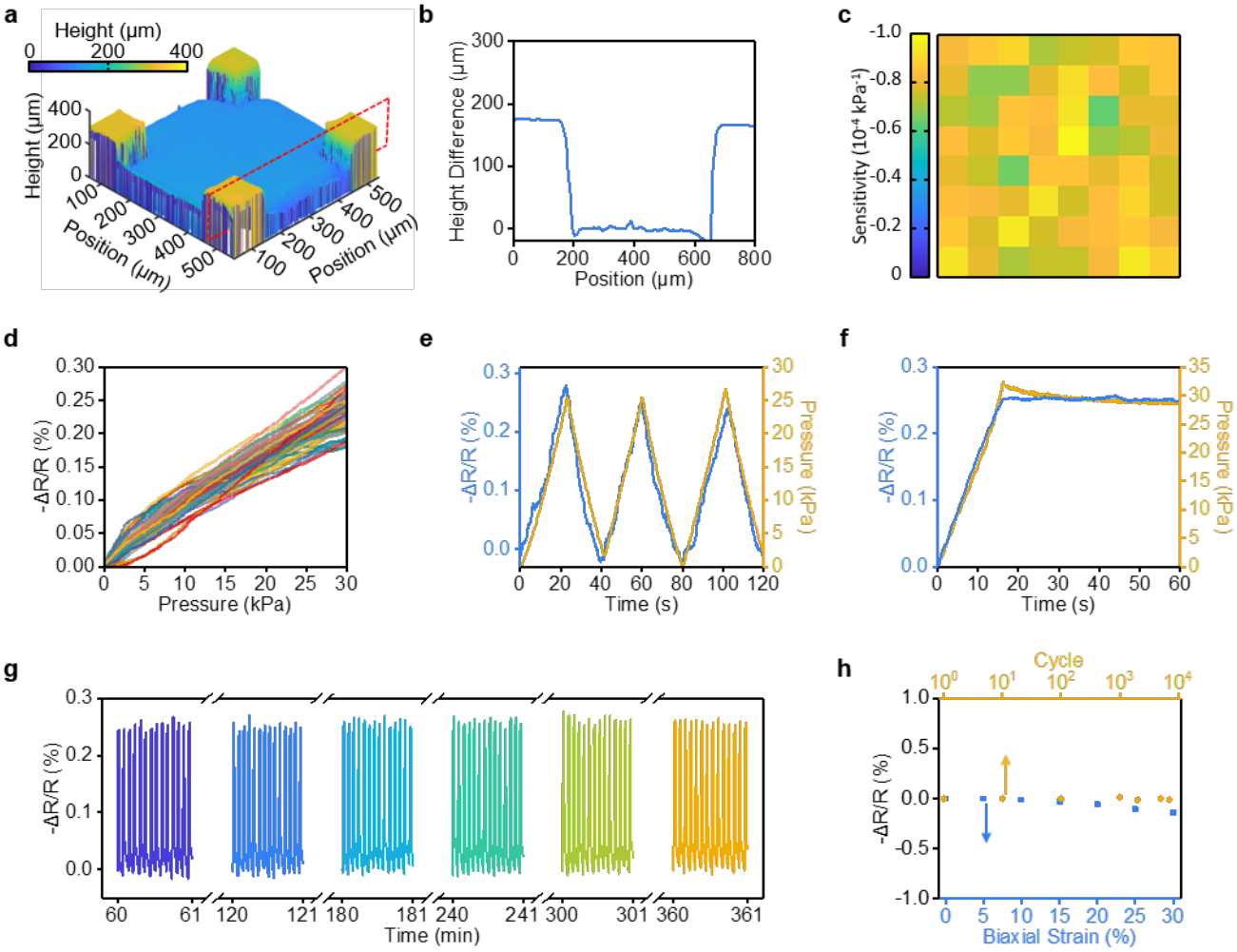

Supplementary Figure 36. Additional characterization results for the pressure sensor array. a, Height distribution of the silicon cavity measured from a 3D optical profiler. **b,** Height distribution of the silicon structure along the red dashed box in (**a**). **c,** Spatial map of the sensitivities of the array. **d,** Fractional changes of resistance of the sixty-four pressure sensors at pressure from 0 to 30 kPa. **e,** Time-domain fractional change of resistance of the sensor under cyclic loading and unloading with overlapped pressure curve measured from a commercial force gauge. **f,** Time-domain fractional change of resistance of the sensor under constant pressure (blue curve) and pressure measured from a commercial force gauge (orange curve). **g,** Time-domain fractional change of resistance of the pressure sensor from 60 min to 360 min. **h,** Fractional change of resistance of the sensor under cyclic 20% uniaxial stretching (orange points) and different biaxial strains (blue points).

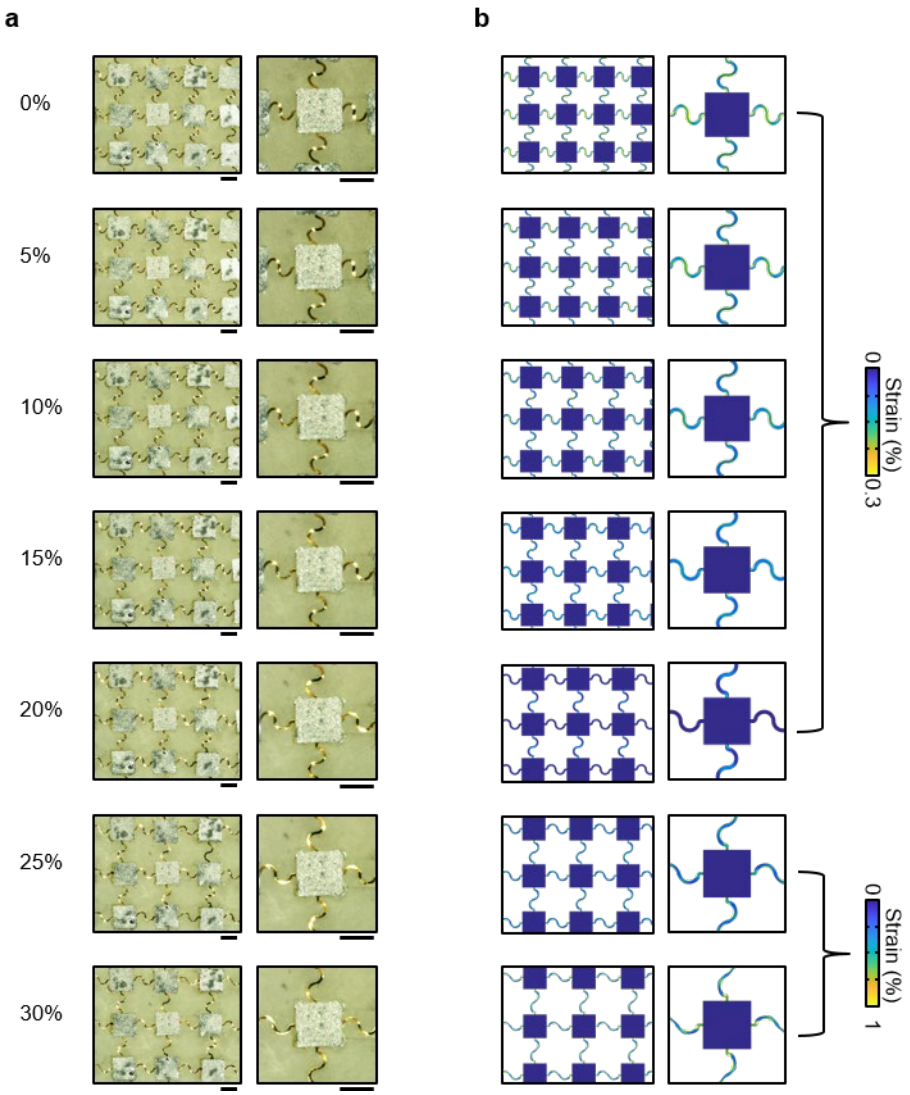

Supplementary Figure 37. Pressure sensor array under biaxial stretching. a, Optical images. **b,** FEA results. Scale bars, 700 μm.

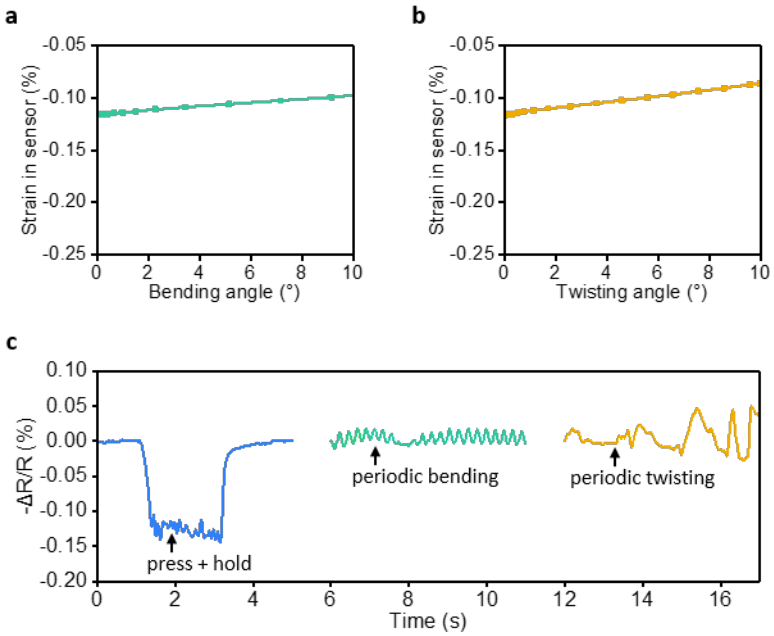

Supplementary Figure 38. Responses of a representative pressure sensor under twisting and bending. a, FEA results for the strain in the pressure sensor under twisting. **b,** FEA results for the strain in the pressure sensor under bending. **c,** Experimental results for the fractional change of resistance in the pressure sensor under various kinds of deformations.

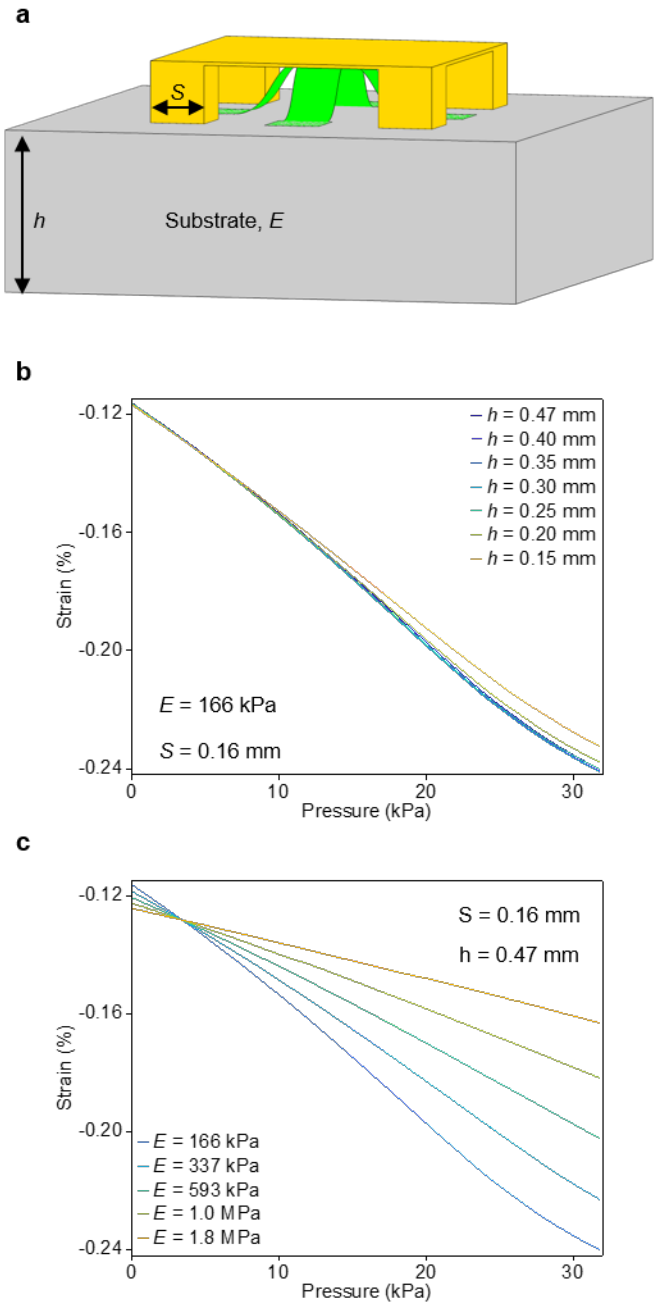

Supplementary Figure 39. FEA results for the sensitivities of the 3D pressure sensors for different design parameters. **a,** Schematic illustration. **b,** Influence of the substrate thickness (*h*). **c,** Influence of the substrate modulus (*E*).

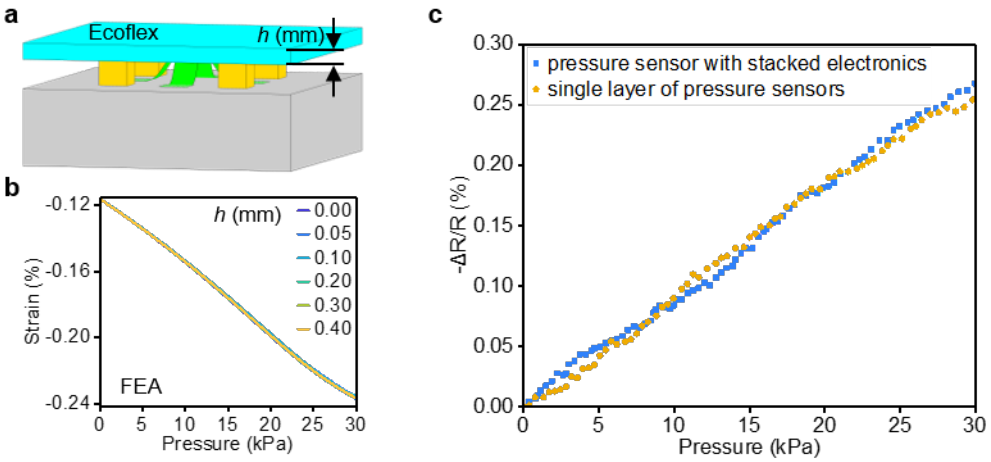

Supplementary Figure 40. Sensitivity of the 3D pressure sensors with and without top elastomeric layer. a, Schematic illustration. **b,** FEA results. **c,** Experimental results of the sensitivity before and after addition of layers with arrays of electrodes and temperature sensors. The elastomeric substrate for the electrode and temperature is Ecoflex (~100 μm in thickness).

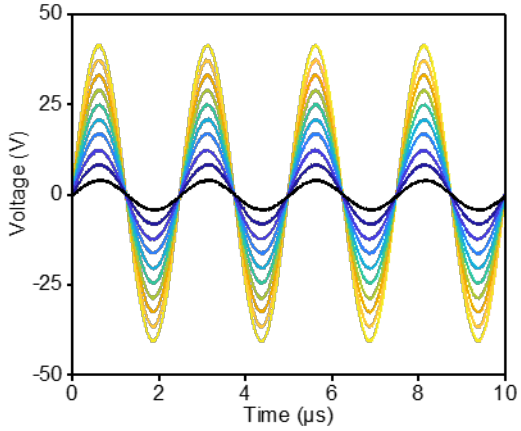

Supplementary Figure 41. Waveforms for different input signals for RF ablation.

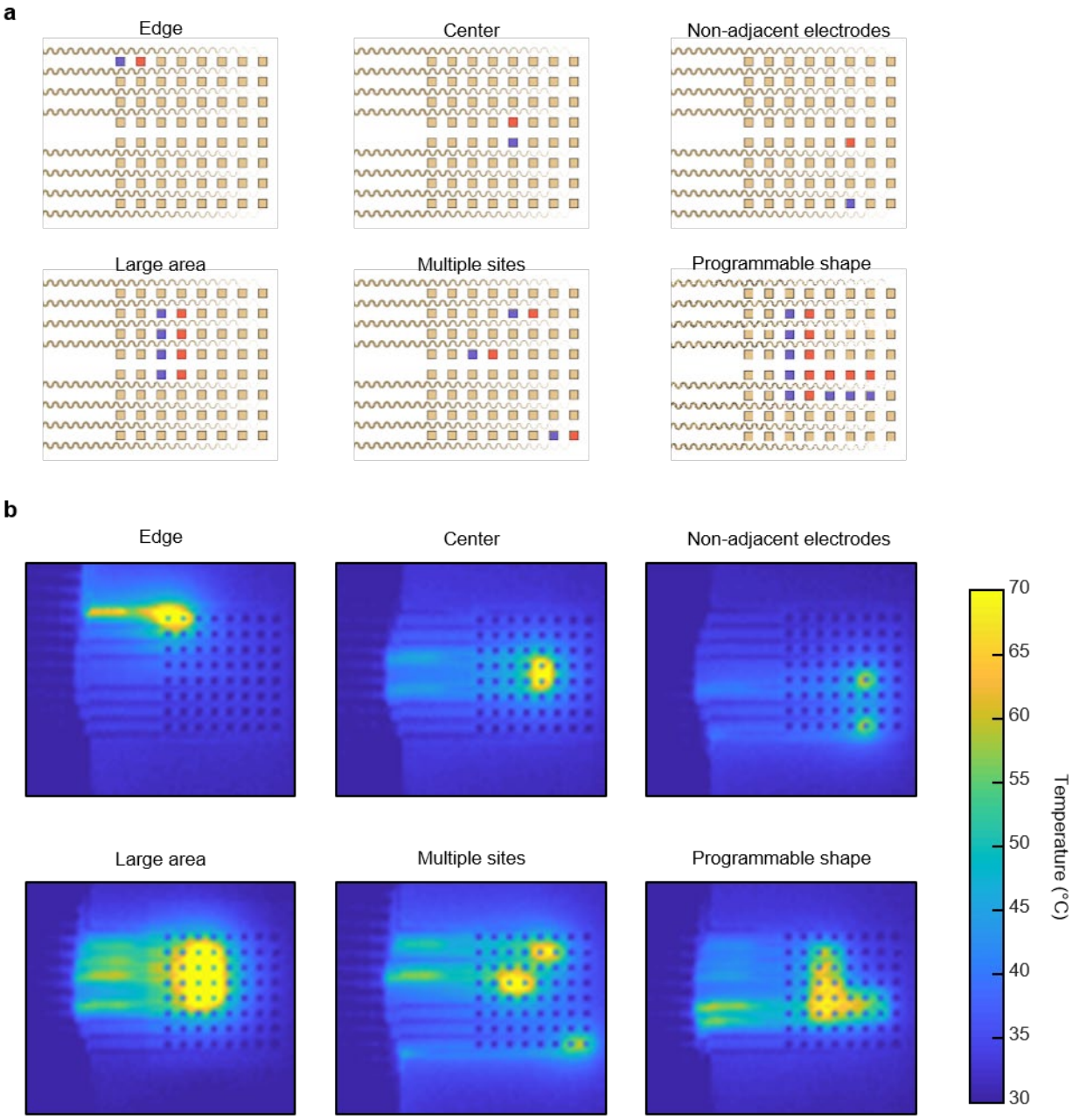

Supplementary Figure 42. Various spatial distributions of temperatures of bipolar RF ablation on agar hydrogel at 37 °C. a, Schematic illustrations. Red and blue squares indicate the electrodes connected to RF signal input and ground, respectively. **b,** Temperature distributions measured from an IR microscope.

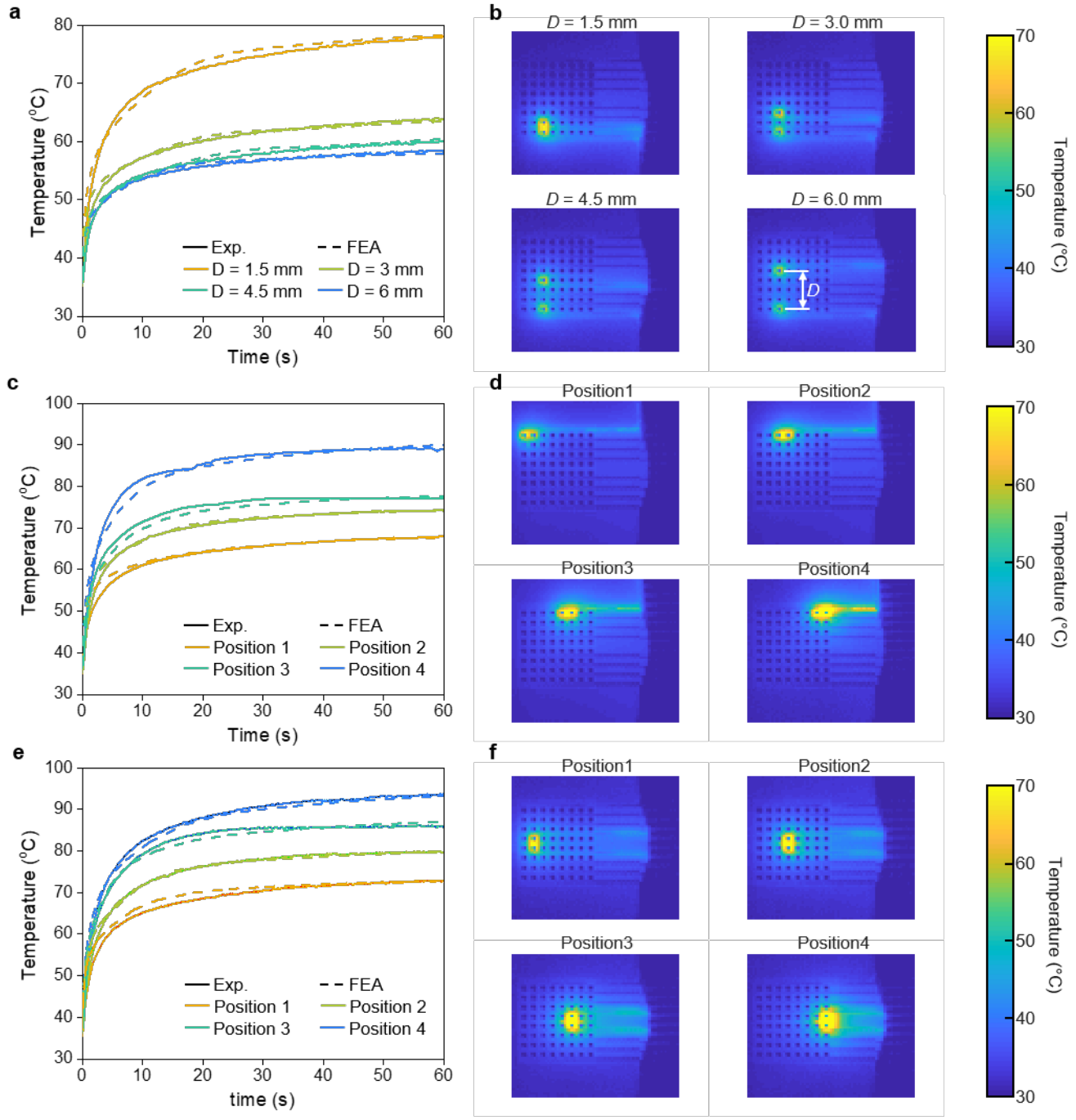

Supplementary Figure 43. Experimental results for temporal and spatial distributions of temperatures during bipolar RF ablation on agar hydrogel at 37 °C. a,b, Time-domain temperature profiles (**a**) and spatial temperature distributions (**b**) at different distances. **c,d,** Time-domain temperature profile (**c**) and spatial temperature distribution (**d**) at different positions (adjacent electrodes, adjacent wires). **e,f,** Time-domain temperature profile (**e**) and temperature distribution (**f**) at different positions (adjacent electrodes, non-adjacent wires, measured from an IR microscope). Solid and dashed lines in (**a**), (**c**) and (**e**) are experimental results measured with an IR microscope and FEA results, respectively. Temperature distributions in (**b**), (**d**) and (**f**) are experimental results measured from an IR microscope.

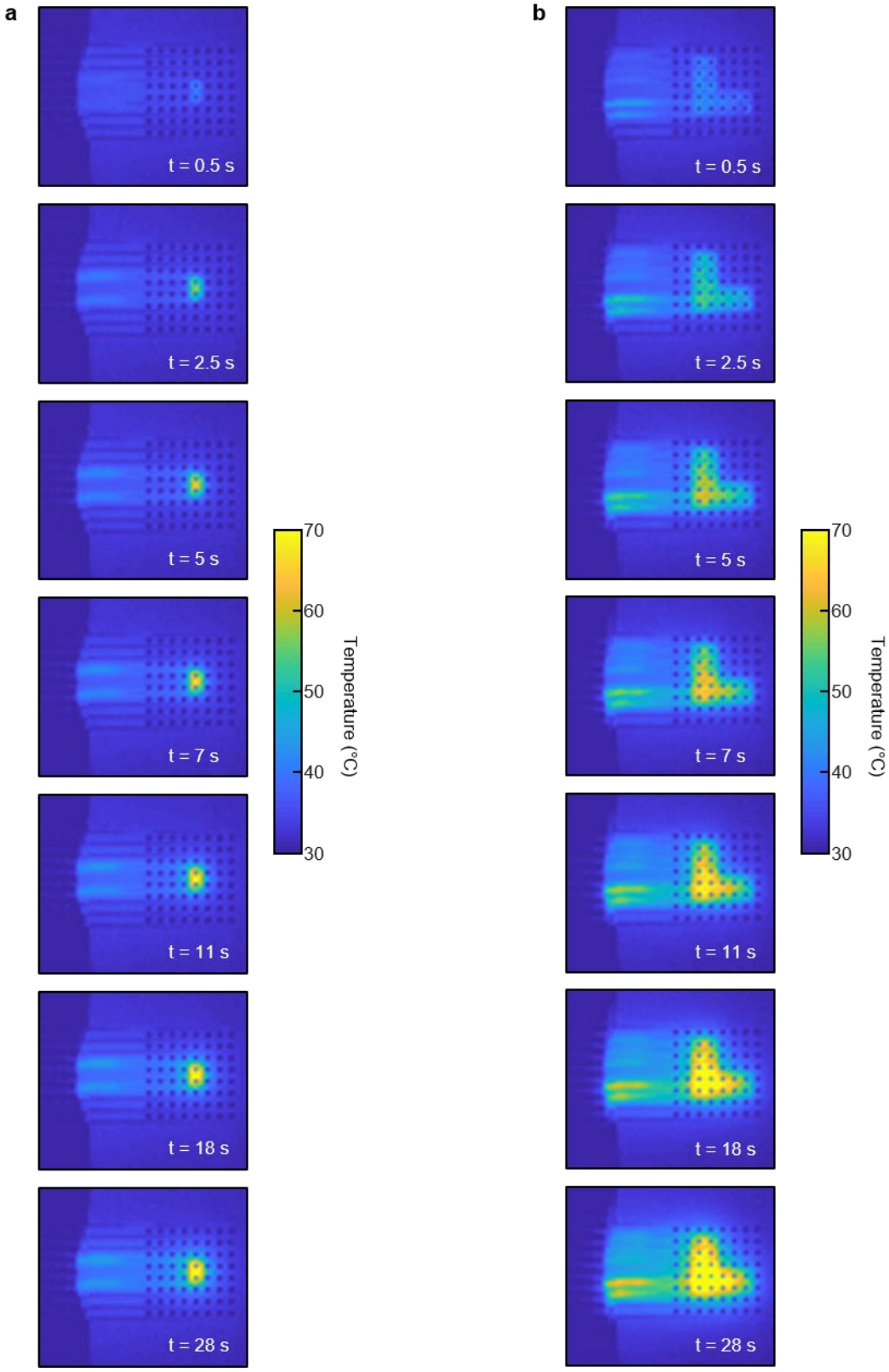

Supplementary Figure 44. Distributions of temperatures associated with bipolar RF ablation (agar hydrogel, 37 °C) at different time points (measured from an IR microscope). a, Ablation with two adjacent electrodes. **b,** Ablation with multiple electrodes.

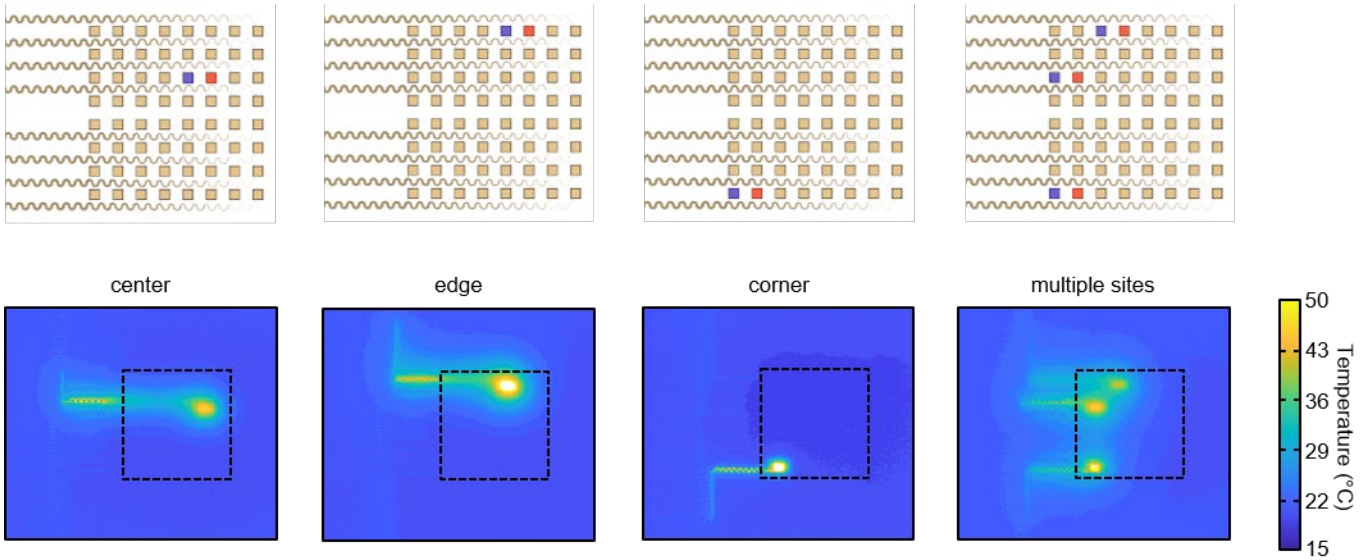

Supplementary Figure 45. Experimental results for bipolar RF ablation on PBS (0.1 M) at room temperature (measured from an IR microscope). Top frames are schematic illustrations. Red and blue squares indicate the electrodes connected to RF signal input and ground, respectively. Bottom frames are corresponding spatial distributions of temperatures. Black dashed boxes indicate positions of the electrode array.

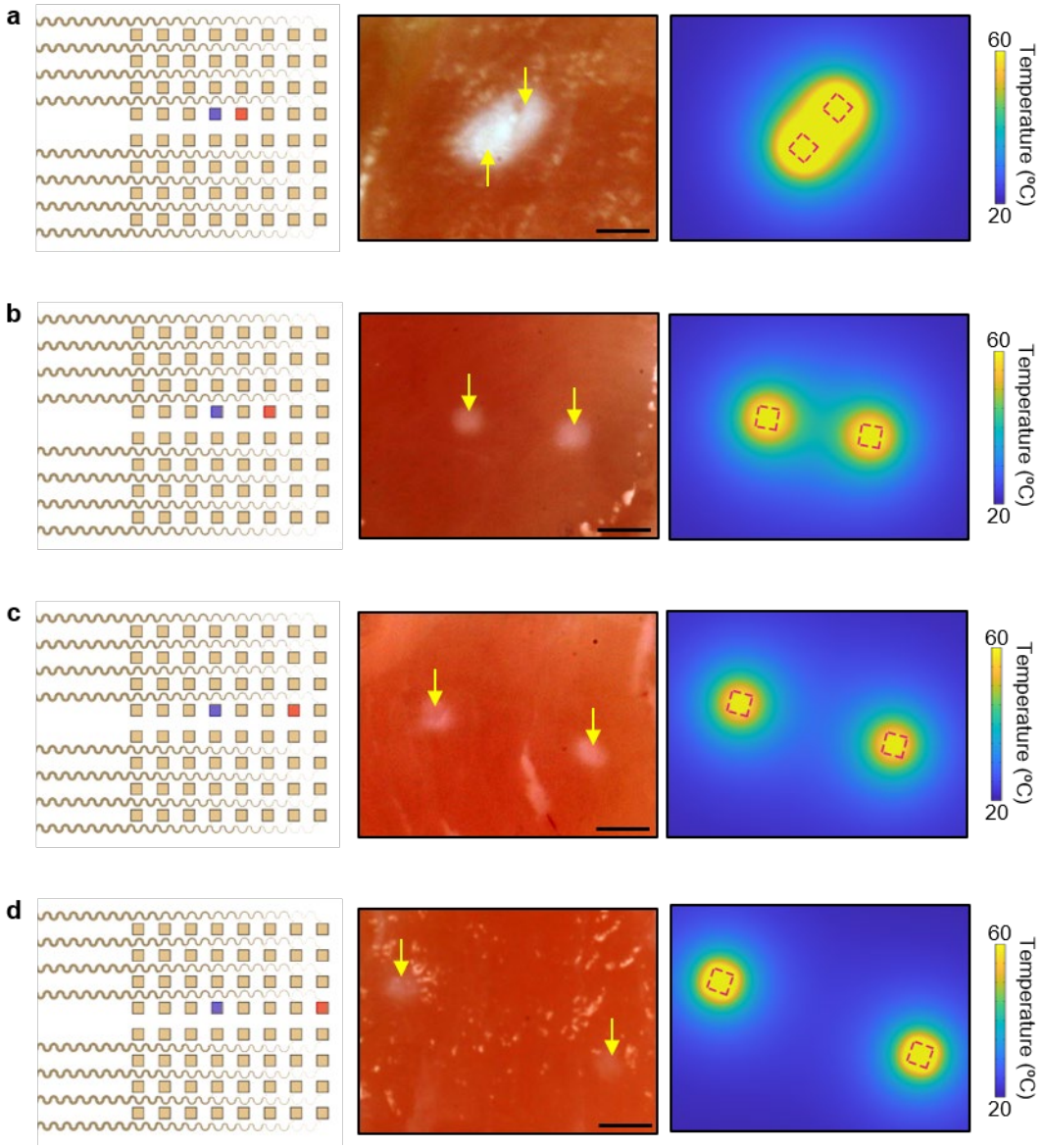

Supplementary Figure 46. Schematic illustrations (left), optical images of the lesions (middle) and FEA results of temperature distributions (right) of bipolar RF ablation on non-perfused tissues. a, Distance between two electrodes: 1.5 mm. **b,** Distance between two electrodes: 3.0 mm. **c,** Distance between two electrodes: 4.5 mm. **d,** Distance between two electrodes: 6.0 mm. Red and blue squares in the schematic illustrations indicate the electrodes connected to RF signal input and ground, respectively. Yellow arrows in the optical images indicate positions of the lesions. Scale bars, 1.5 mm.

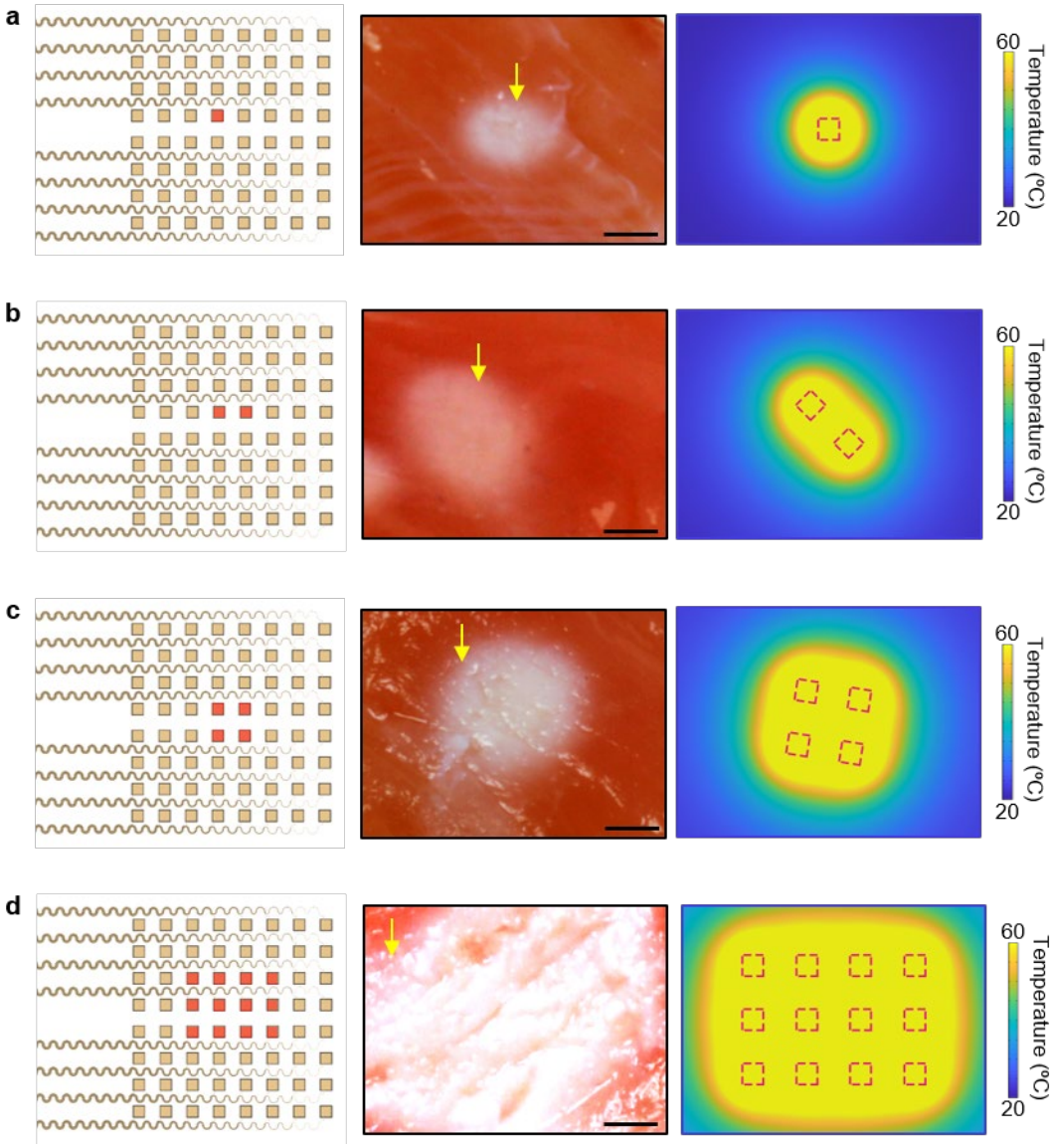

Supplementary Figure 47. Schematic illustrations (left), optical images of the lesions (middle) and FEA results of temperature distributions (right) for monopolar RF ablation on non-perfused tissues. a, One electrode. **b,** Two electrodes. **c,** Four electrodes. **d,** Twelve electrodes. Red squares in the schematic illustrations indicate the electrodes with RF signal input. Yellow arrows in the optical images indicate positions of the lesions. Scale bars, 1.5 mm.

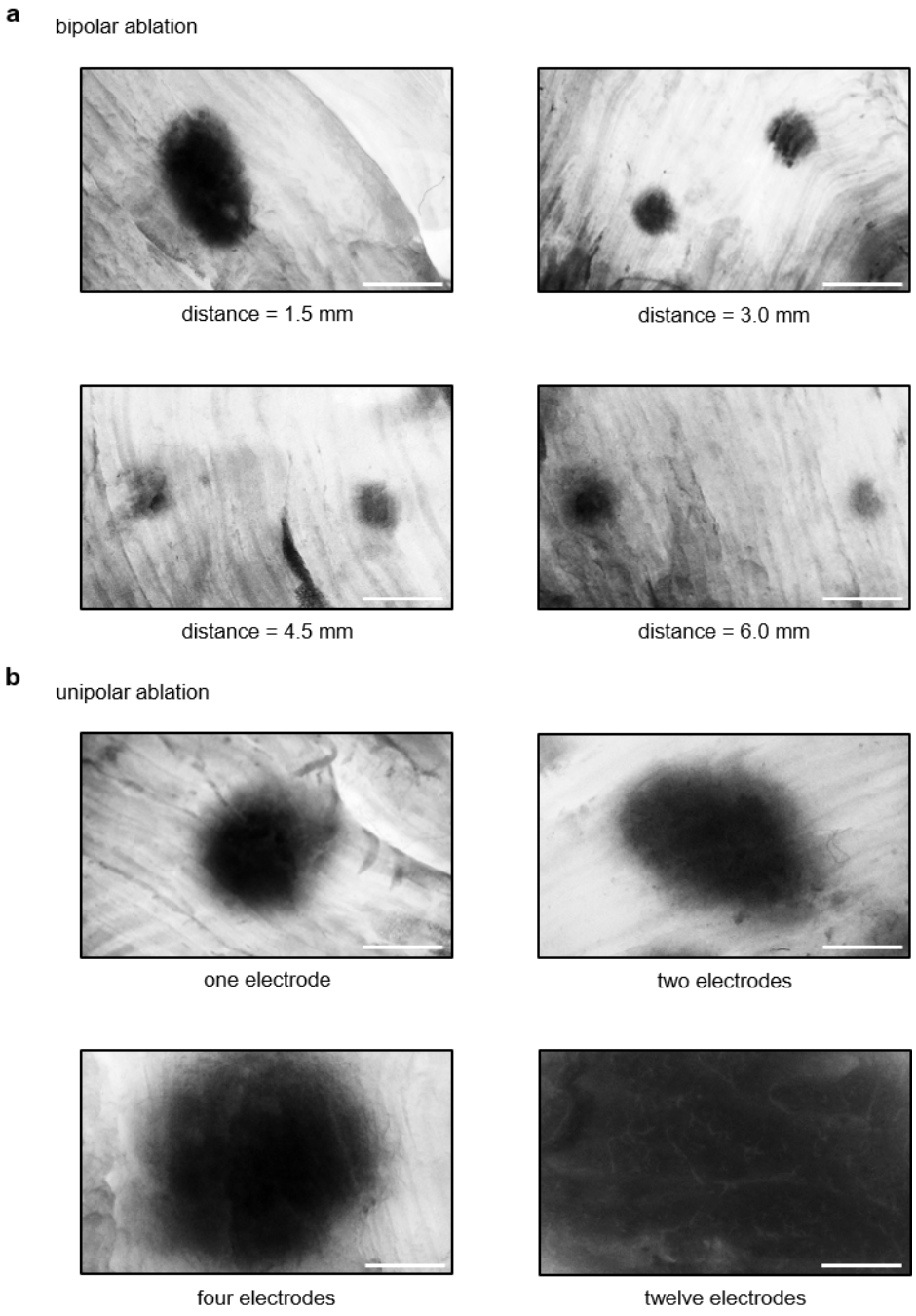

Supplementary Figure 48. Optical images of the lesions in Supplementary Figs. 44 and 45 using transmittance light. a, Bipolar ablation with different distances. **b,** Monopolar ablation with different numbers of electrodes. Scale bars, 1.5 mm.

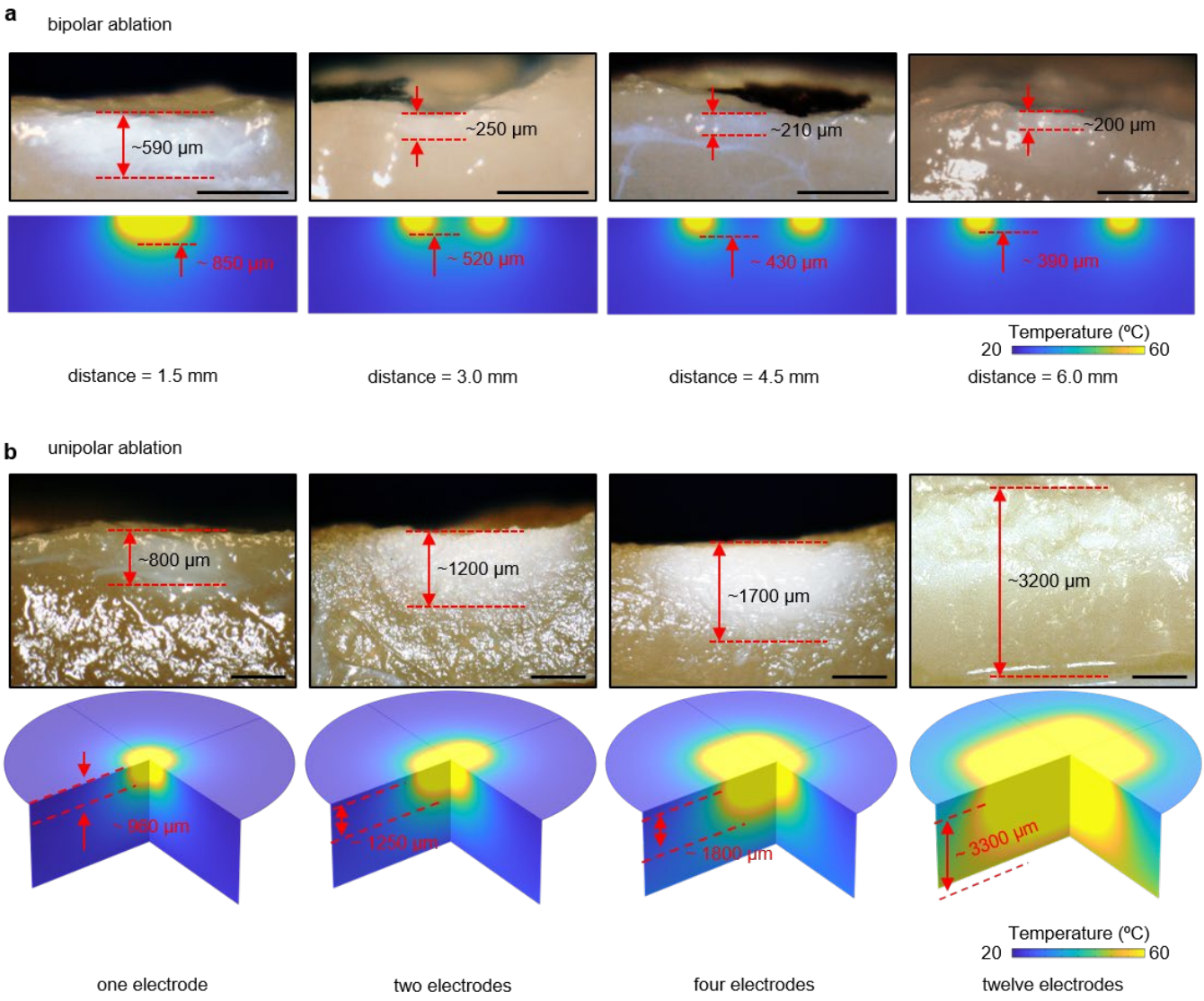

Supplementary Figure 49. Side view of the lesions in Supplementary Figs. 44 and 45. a, Optical images of the lesions (top) and FEA results of the temperature distributions (bottom) during bipolar ablation with different distances. **b,** Optical images of the lesions (top) and FEA results of the temperature distributions (bottom) during monopolar ablation with different numbers of electrodes. Scale bars, 1 mm.

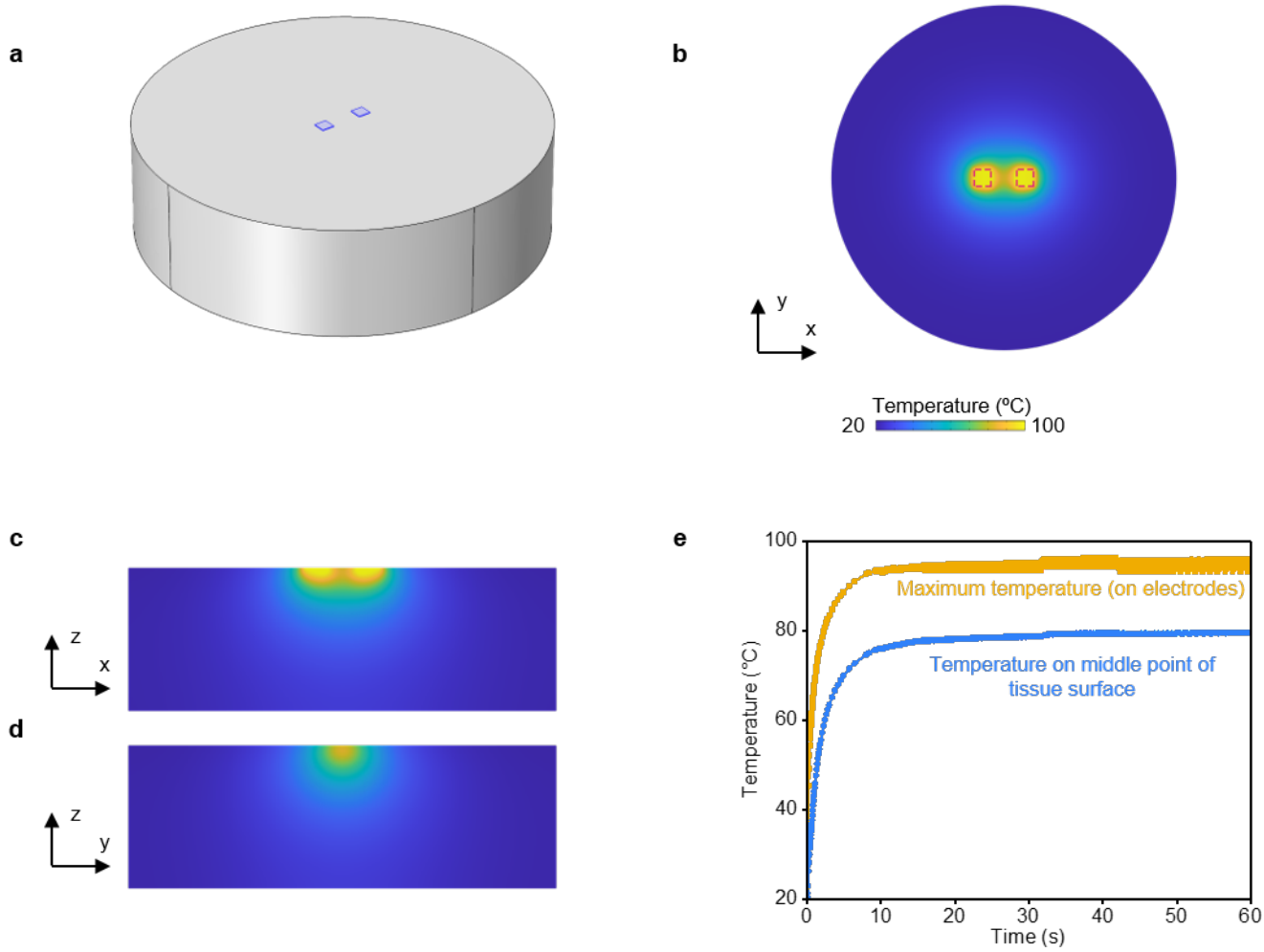

Supplementary Figure 50. FEA results of the temperature distribution determined by coupled thermal and electrical modelling of the ablation process. a, Schematic illustration of the model. **b,** Top view. **c,** Front view. **d,** Left view. **e,** Maximum temperature on electrodes and temperature on middle point of tissue surface during ablation.

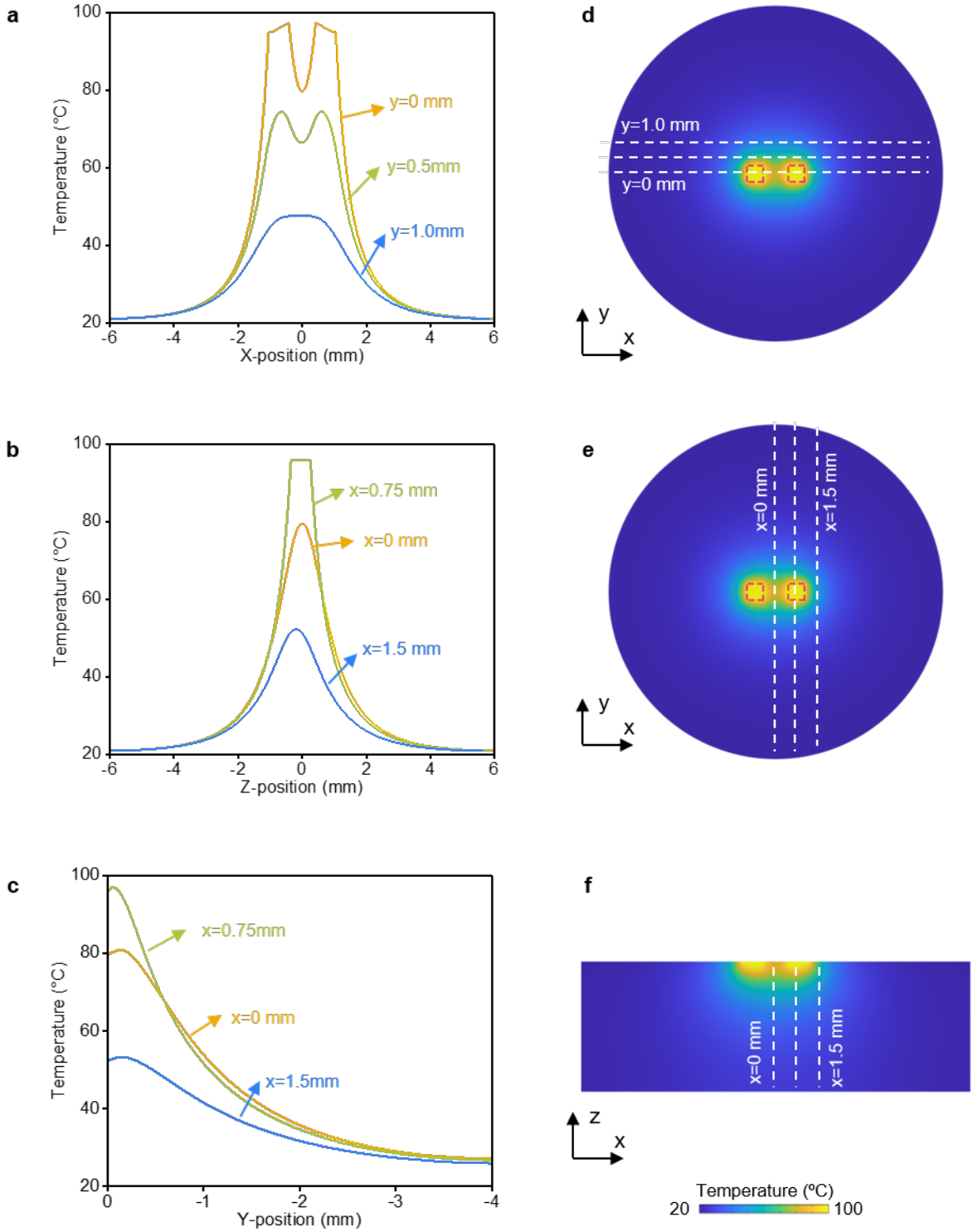

Supplementary Figure 51. FEA results of the temperature distributions in different directions. a, Along X-axis. **b,** Along Y-axis, **c,** Along Z-axis.

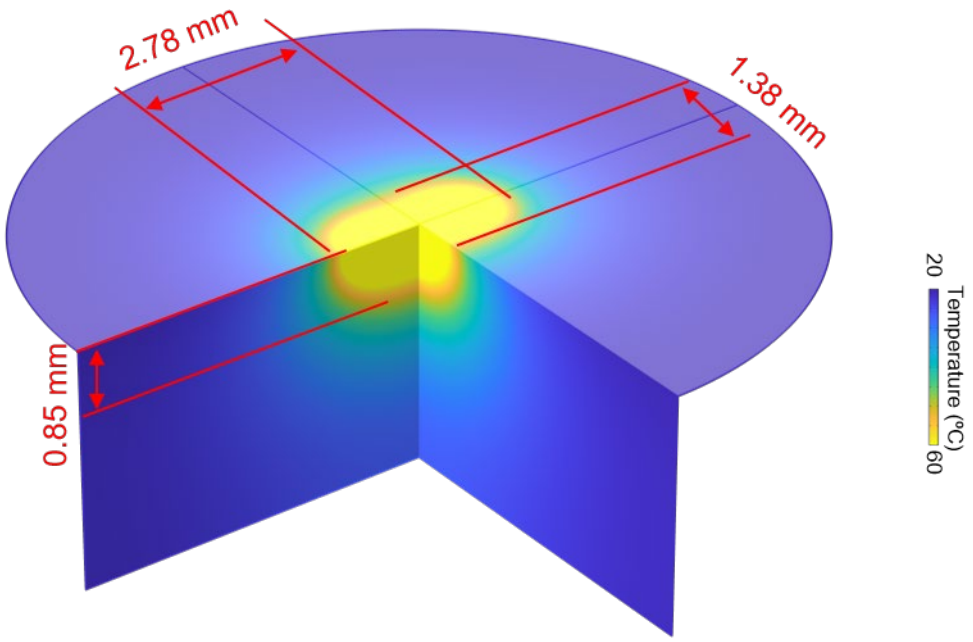

Supplementary Figure 52. FEA results of temperature distribution under bipolar RF ablation on non-perfused tissue.

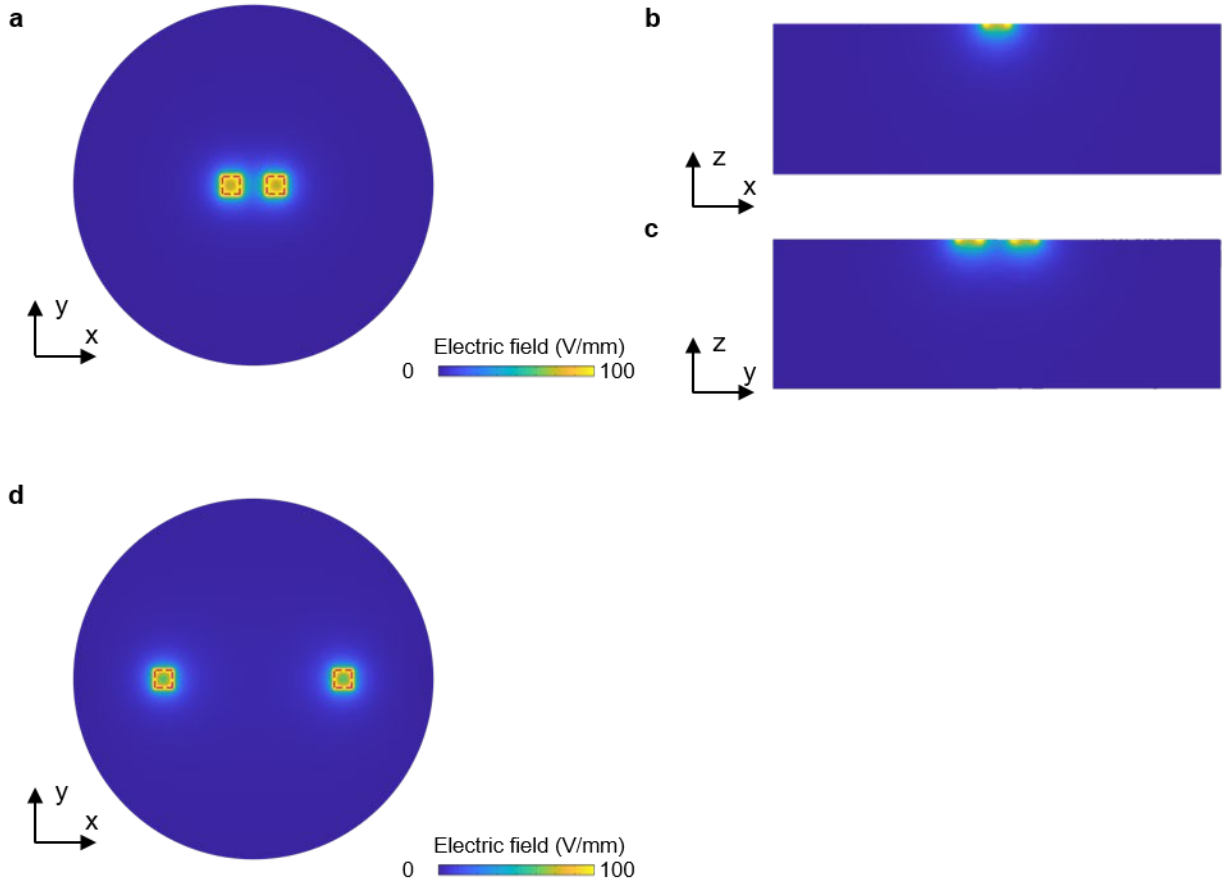

Supplementary Figure 53. FEA results of electric filed distributions determined by coupled thermal and electrical modelling of the ablation process. a-c, Top view (**a**), front view (**b**), and left view (**c**) with electrode spacing of 1.5 mm. **d,** Top view with electrode spacing of 6 mm.

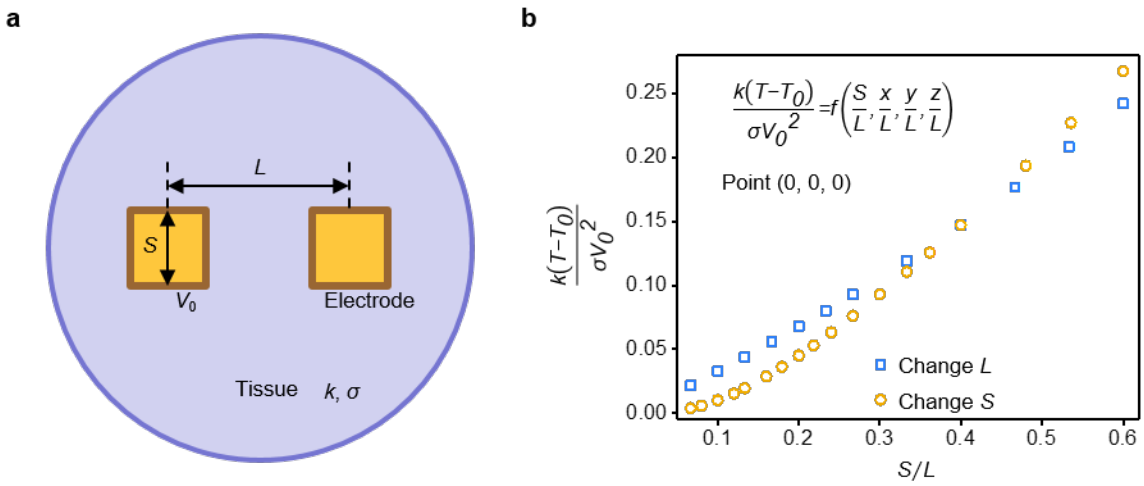

Supplementary Figure 54. FEA validation of the scaling law for steady-state bipolar tissue ablation without consideration of the substrate underneath the electrodes. a, Schematic illustration of the tissue ablation model. L is the distance between adjacent electrodes, S is the side length of the electrodes, V_0 is the applied potential, k and σ are thermal conductivity and electric conductivity of the tissue, respectively. **b,** Normalized temperature vs. normalized geometry parameters. T_0 is the initial temperature, T is the temperature after ablation, x, y, z are the positions in Cartesian coordinates, respectively. The results in (**b**) correspond to the case where x=y=z=0.

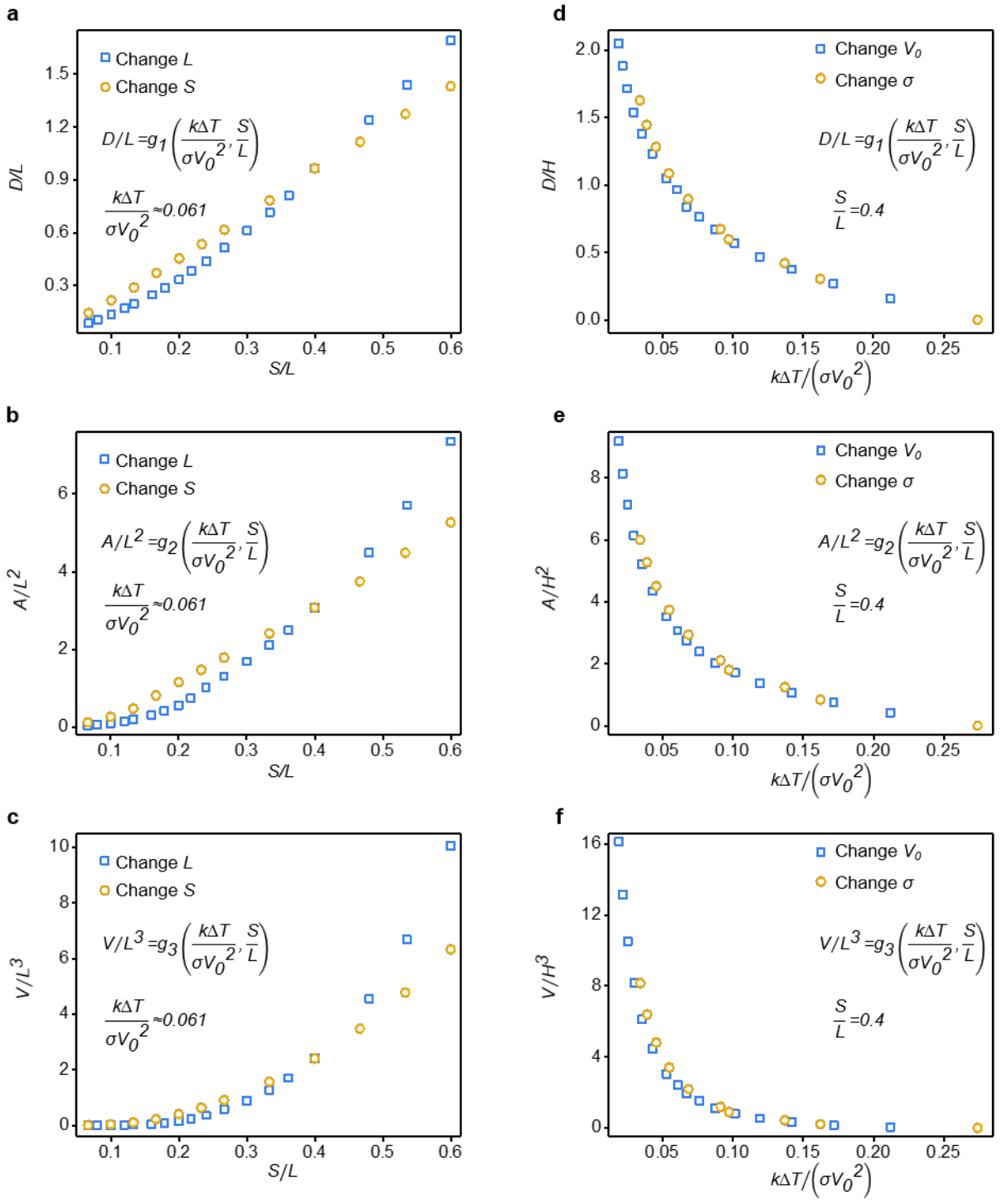

Supplementary Figure 55. FEA validation of the scaling law for steady-state bipolar tissue ablation without consideration of the substrate underneath the electrodes. a-c, Normalized lesion size vs. normalized geometry parameters. D, A, and V are the lesion depth (under the electrode), area, and volume, respectively. L is the distance between adjacent electrodes, S is the side length of the electrodes. **d-f,** Normalized lesion size vs. normalized physical parameters. V_0 is the applied potential, k and σ are thermal conductivity and electric conductivity of the tissue, respectively. ΔT is the temperature difference between lesion temperature (T_c=60 ℃) and the initial temperature (T_0).

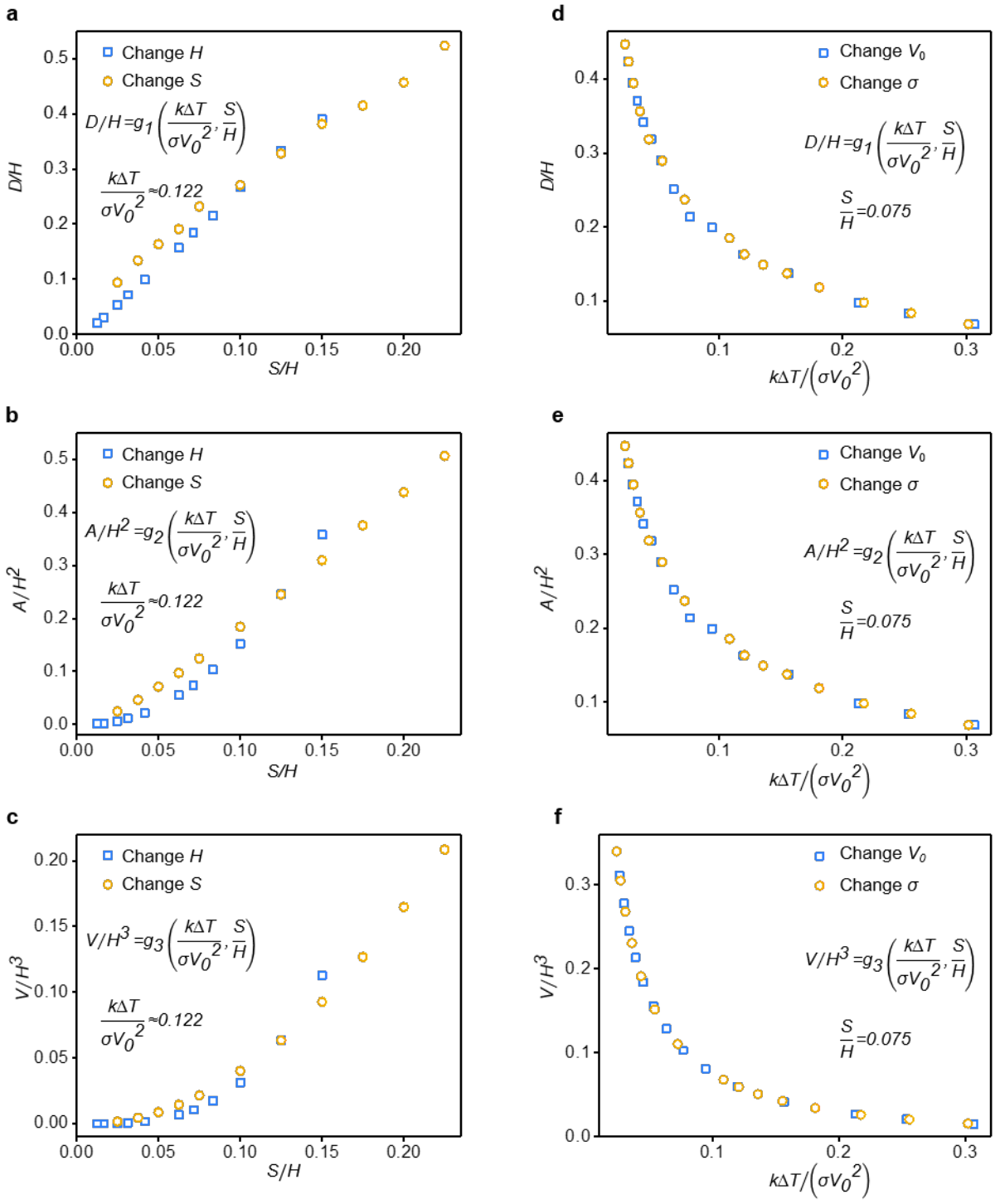

Supplementary Figure 56. FEA validation of the scaling law for steady-state monopolar tissue ablation without consideration of the substrate underneath the electrodes. a-c, Normalized lesion size vs. normalized geometry parameters. D, A, and V are the lesion depth (under the electrode), area, and volume, respectively. H is the tissue thickness, S is the side length of the electrodes. **d-f,** Normalized lesion size vs. normalized physical parameters. V_0 is the applied potential, k and σ are thermal conductivity and electric conductivity of the tissue, respectively. ΔT is the temperature difference between lesion temperature (T_c=60 °C) and the initial temperature (T_0).

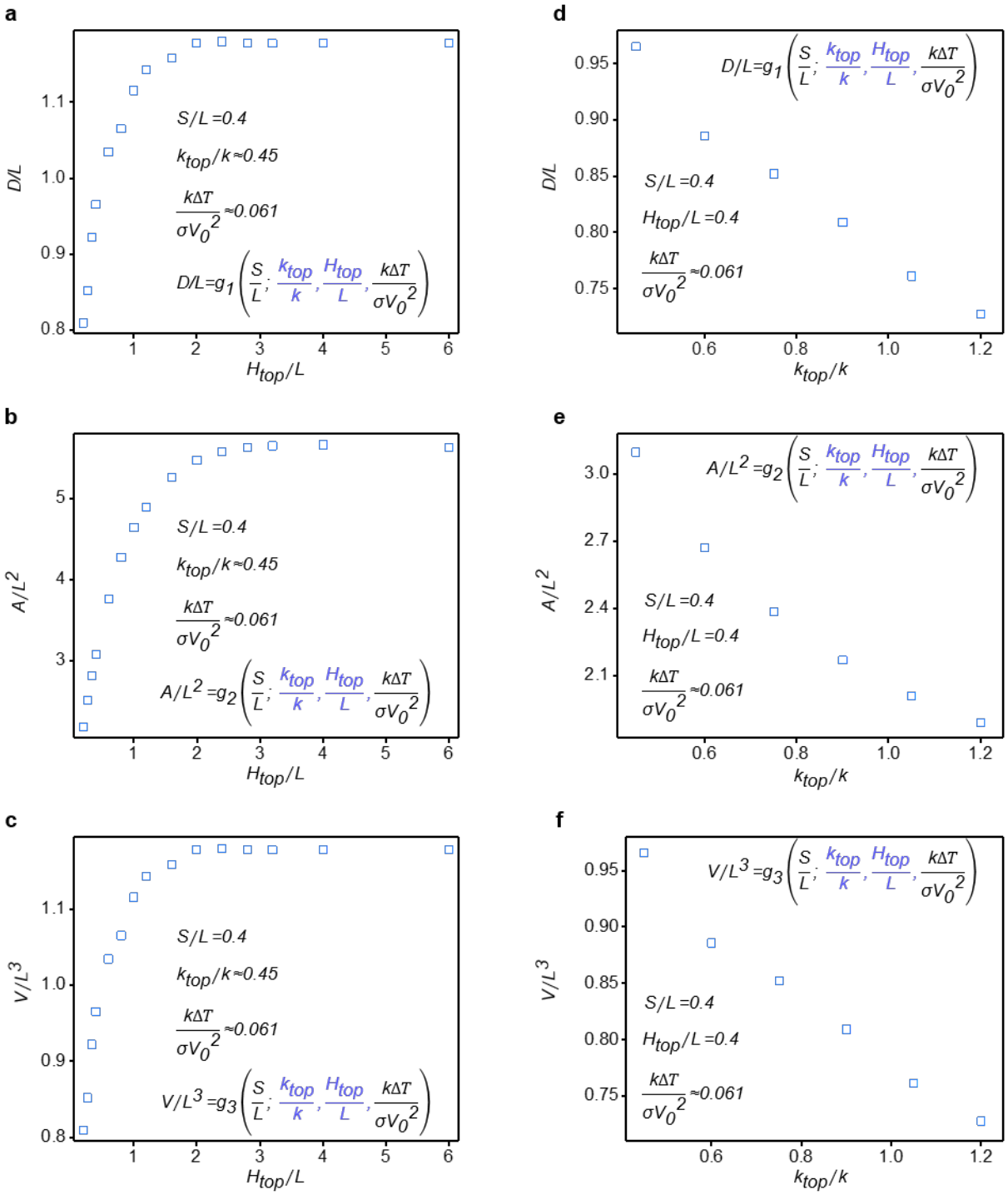

Supplementary Figure 57. Influence of substrate underneath the electrodes on steady-state bipolar tissue ablation. **a-c,** Normalized lesion size vs. normalized thickness of substrate under the electrode. D, A, and V are the lesion depth (under the electrode), area, and volume, respectively. H_{top} is the thickness of the substrate under the electrodes, L is the distance between adjacent electrodes, S is the side length of the electrodes. **d-f,** Normalized lesion size vs. normalized thermal conductivity of substrate under the electrode. k_{top} is the thermal conductivity of the substrate under the electrode, k and σ are thermal conductivity and electric conductivity of the tissue, respectively. V_0 is the applied potential. ΔT is the temperature difference between the lesion temperature (T_c=60 °C) and the initial temperature (T_0).

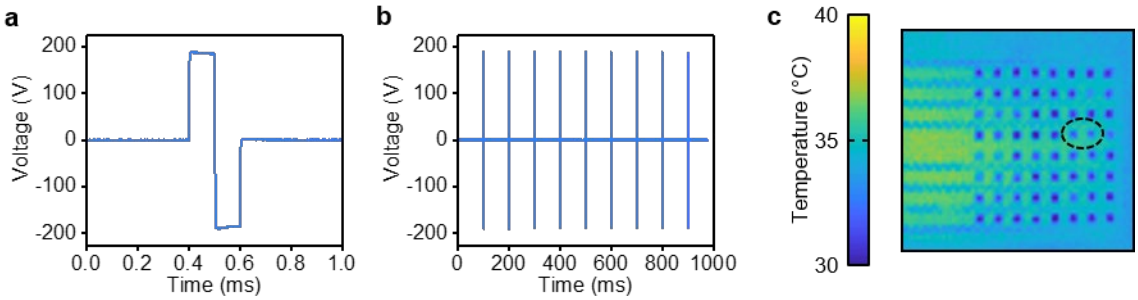

Supplementary Figure 58. Typical input signal for electroporation. a, Waveform of the input pulse for electroporation**. b,** Waveform of the input pulses applied at a frequency of 10 Hz. **c,** Temperature distribution (measured from an IR microscope) during electroporation with 1 Hz, ~200 V biphasic pulses (pulse duration: 100 μs). The black dashed circle indicates the electrodes with input pulse for electroporation.

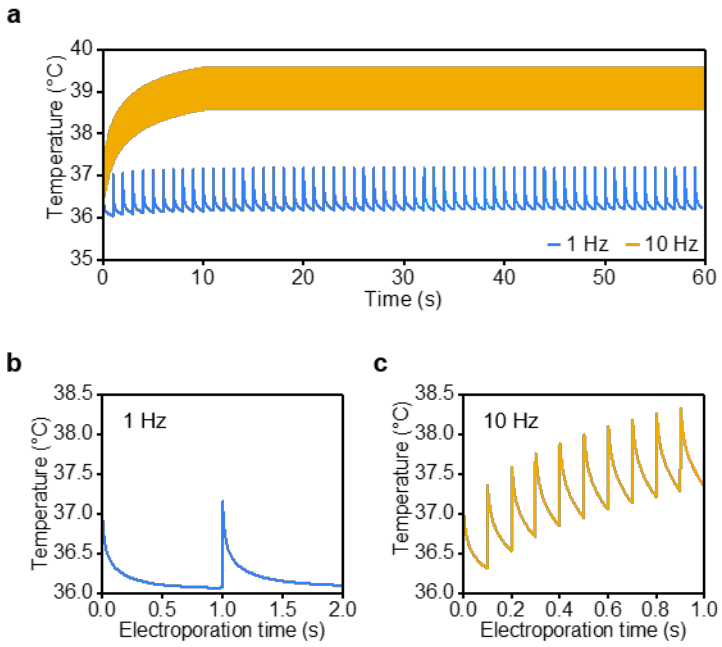

Supplementary Figure 59. FEA results of the temperature profiles during electroporation at 1 and 10 Hz. a, Temperature profile at 60 s. **b,** Temperature profile at 2 s during electroporation at 1 Hz. **c,** Temperature profile at 1 s during electroporation at 10 Hz.

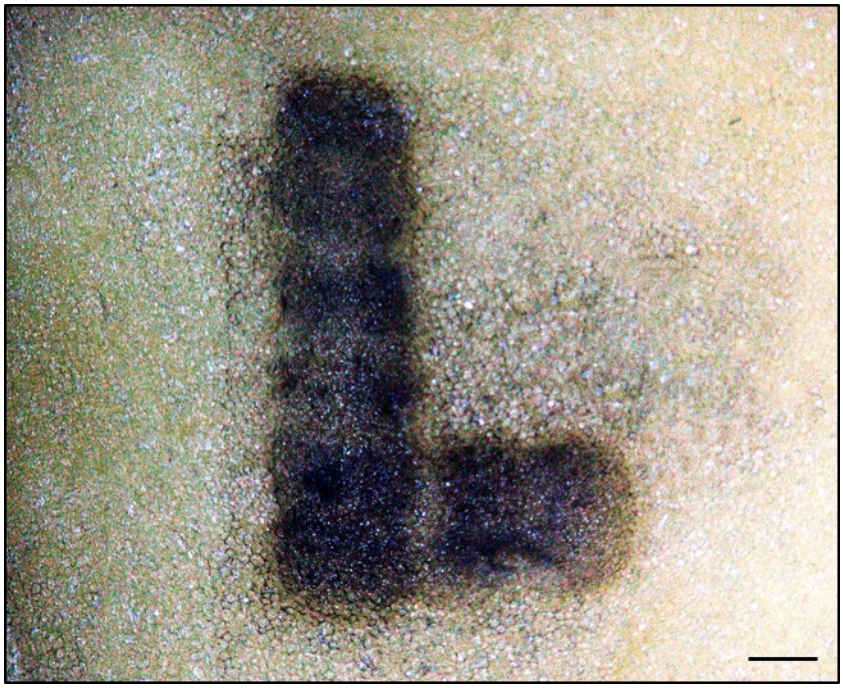

Supplementary Figure 60. Multiple lesions formed on a potato through electroporation. Input signals are biphasic pulses with a duration of 100 μs, a frequency of 1 Hz, an amplitude of 200 V. Scale bar, 1 mm.

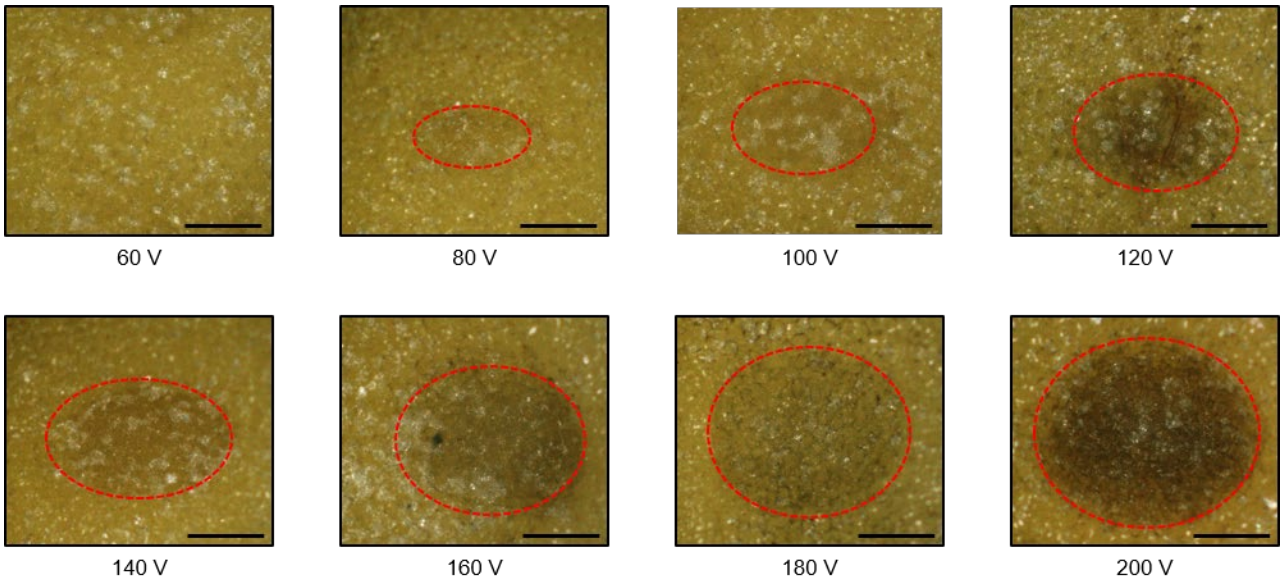

Supplementary Figure 61. Pictures of the potatoes after electroporation with two adjacent electrodes on the electrode array. Input signals are biphasic pulses with a duration of 100 μs, a frequency of 1 Hz, and amplitudes ranging from 60 V to 200 V. Red dashed circles indicate regions of the lesions after electroporation. Scale bars, 1 mm.

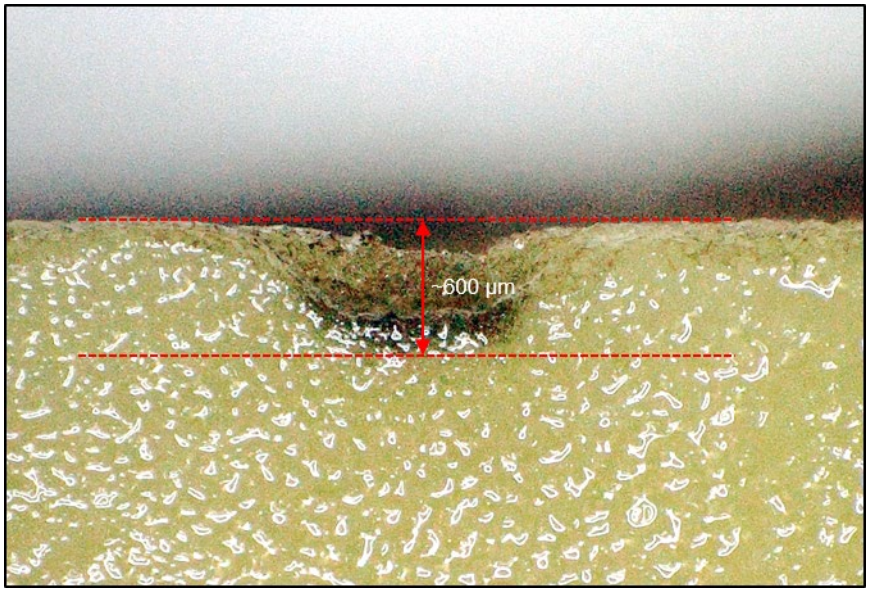

Supplementary Figure 62. Side view of a lesion created through electroporation on a potato model. The input biphasic pulse has a duration of 100 µs, a frequency of 1 Hz, an amplitude of 200 V. Scale bar, 1 mm.

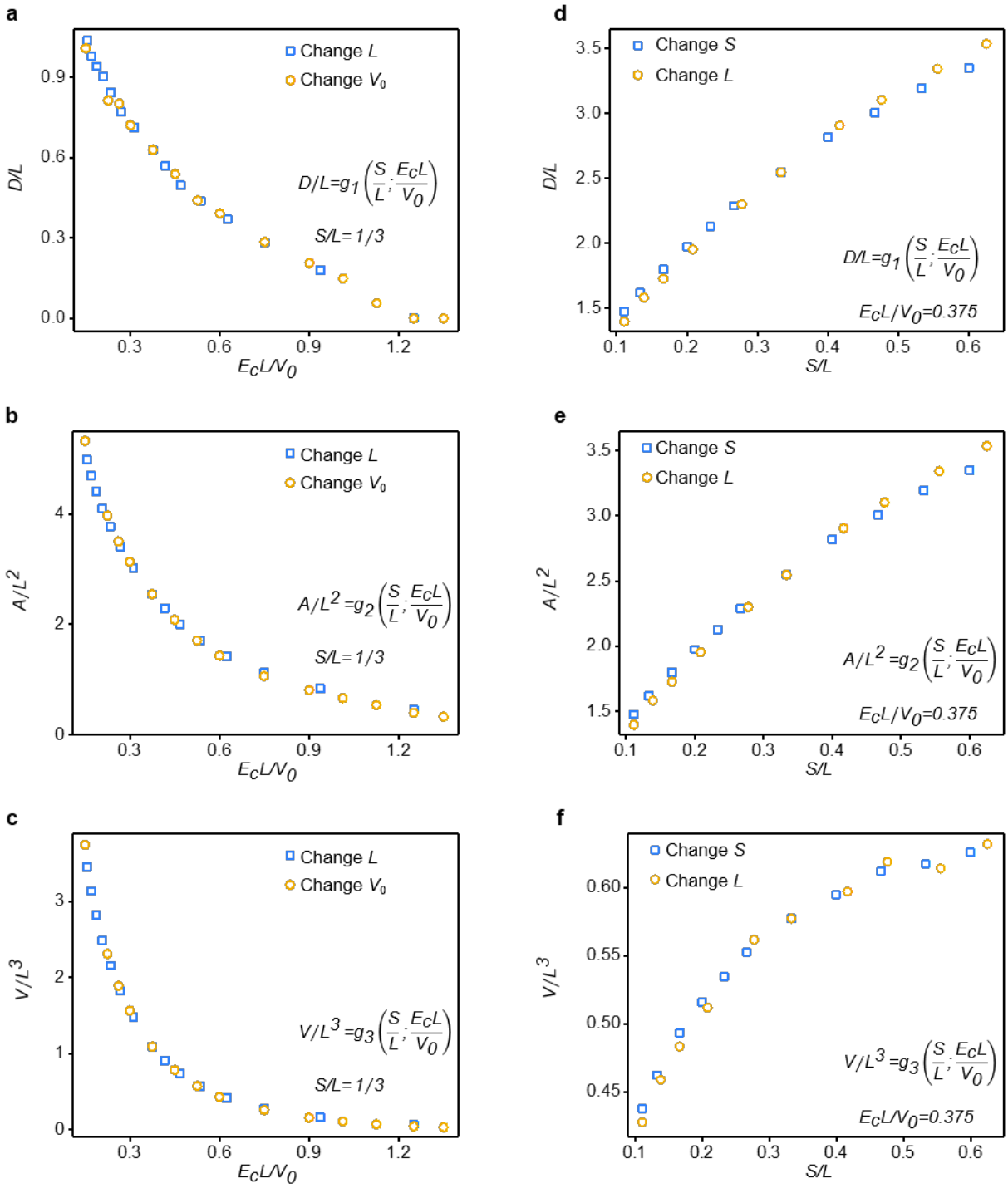

Supplementary Figure 63. FEA validation of the scaling law for potato electroporation with two adjacent electrodes. a-c, Normalized lesion size vs. normalized physical parameters. D, A, and V are the lesion depth (under the electrode), area, and volume, respectively. E_c is the critical electrical intensity (500 V/cm) that causes the potato damage. V_0 is the applied potential, L is the distance between adjacent electrodes, S is the side length of the electrodes. **d-f,** Normalized lesion size vs. normalized geometry parameters.

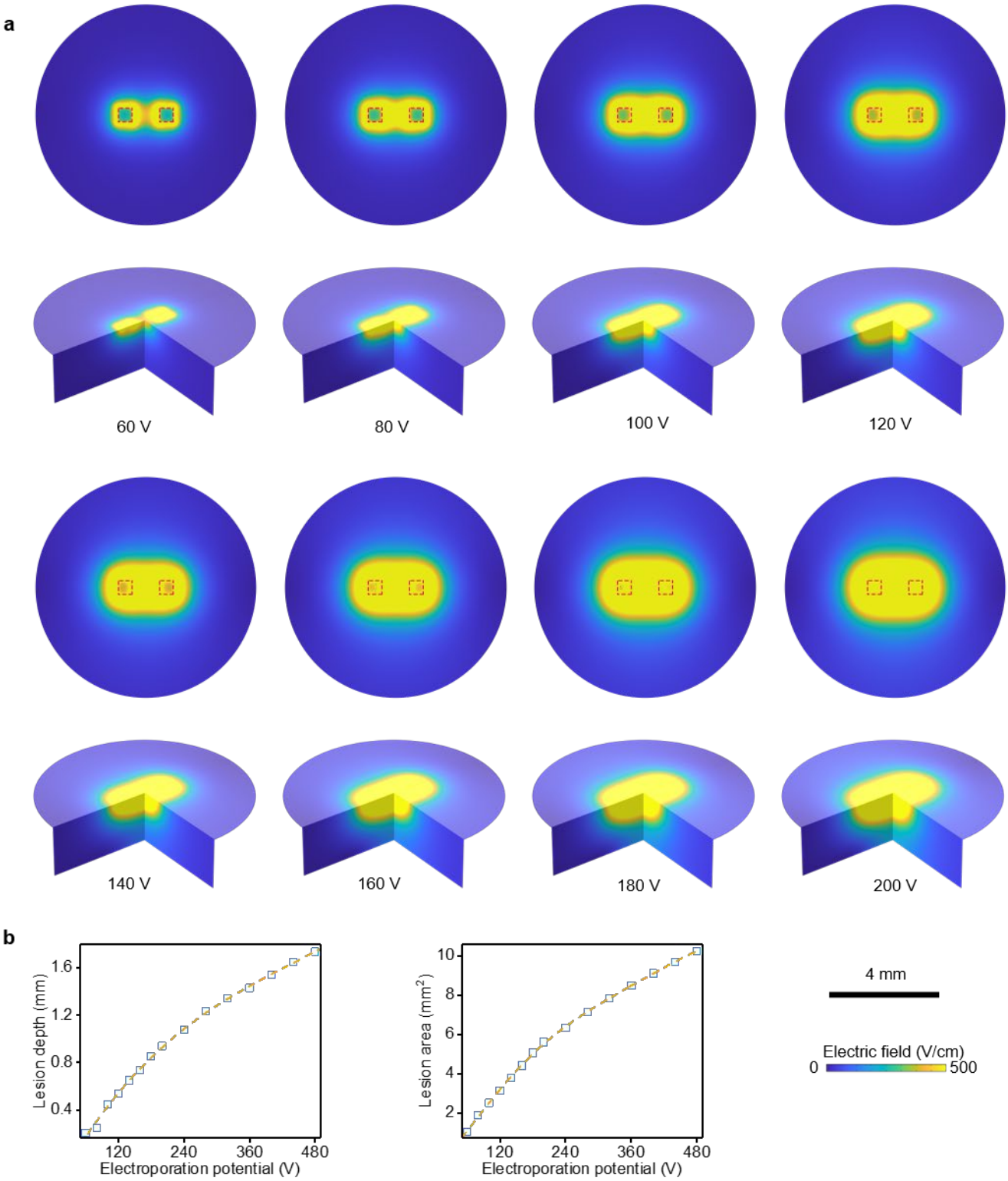

Supplementary Figure 64. FEA results of electroporation on a potato model. a, Electric field distribution under different applied voltages. **b,** Dependence of lesion depth and area (on potato surface) on the applied voltages.

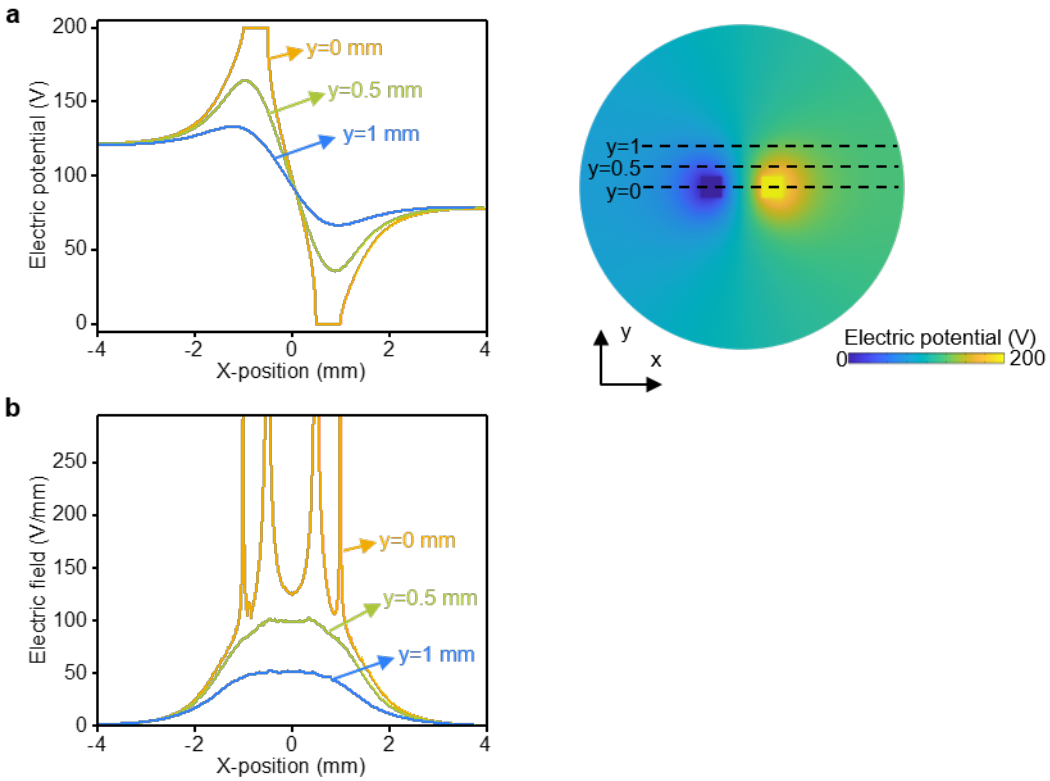

Supplementary Figure 65. FEA results of the distributions of electric potential and electric field along X-axis. a, Electric potential distribution. **b,** Electric field distribution along X-axis. Amplitude of the voltage applied to the electrode is 200 V.

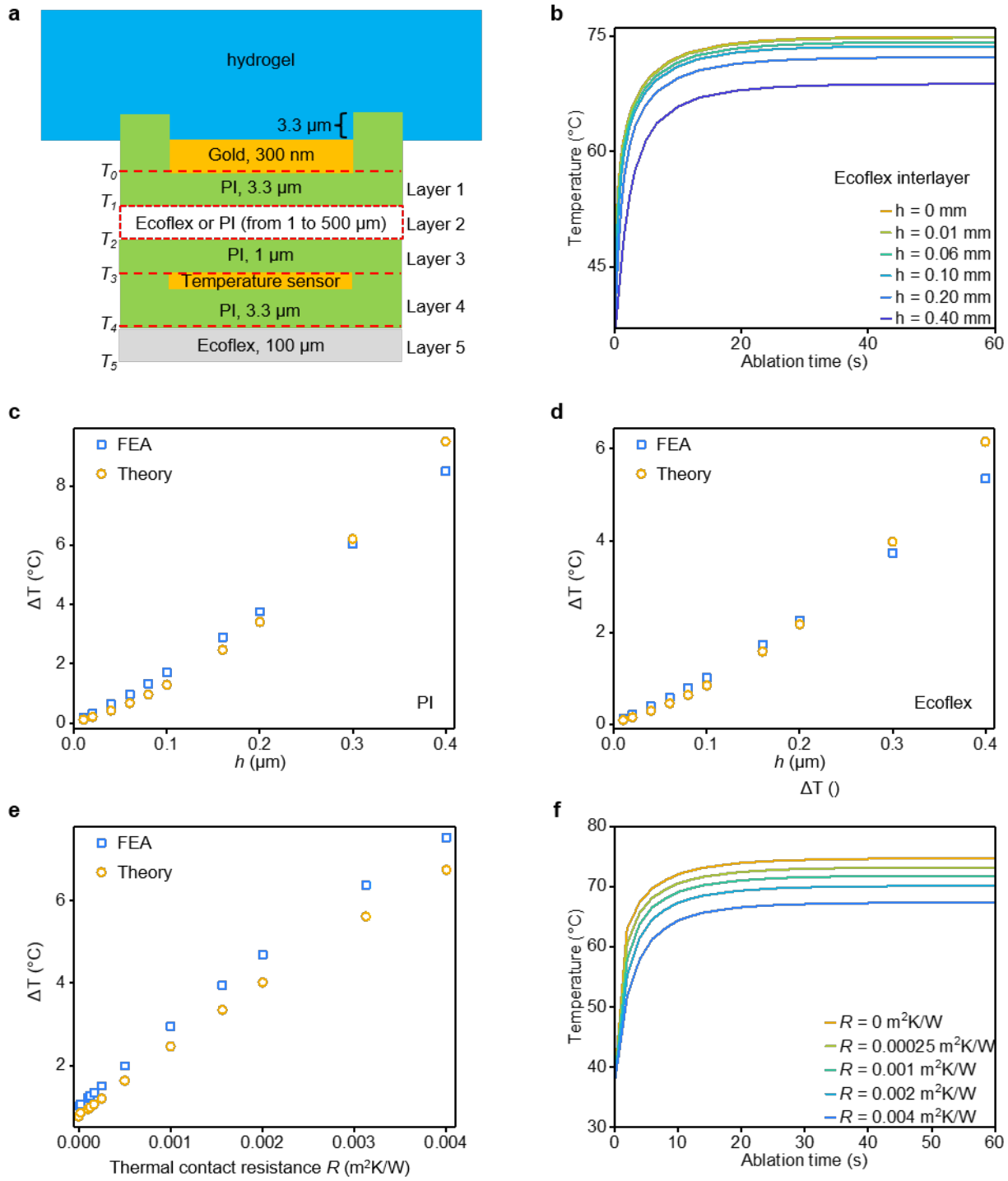

Supplementary Figure 66. FEA results of the temperature difference between electrode and temperature sensor. a, Schematic illustration of the FEA model. **b-d,** Dependence of the temperature difference on the thickness of the interlayer polymer (PI or Ecoflex, Layer 2) shown in (**a**) without considering interface thermal resistance. **e,f,** Dependence of the temperature difference on the thermal contact resistance (*R*) around the interlayer polymer (Layer 2 in (**a**)). The interlayer polymer in (**e,f**) is a layer of Ecoflex with the thickness of 0.1 mm.

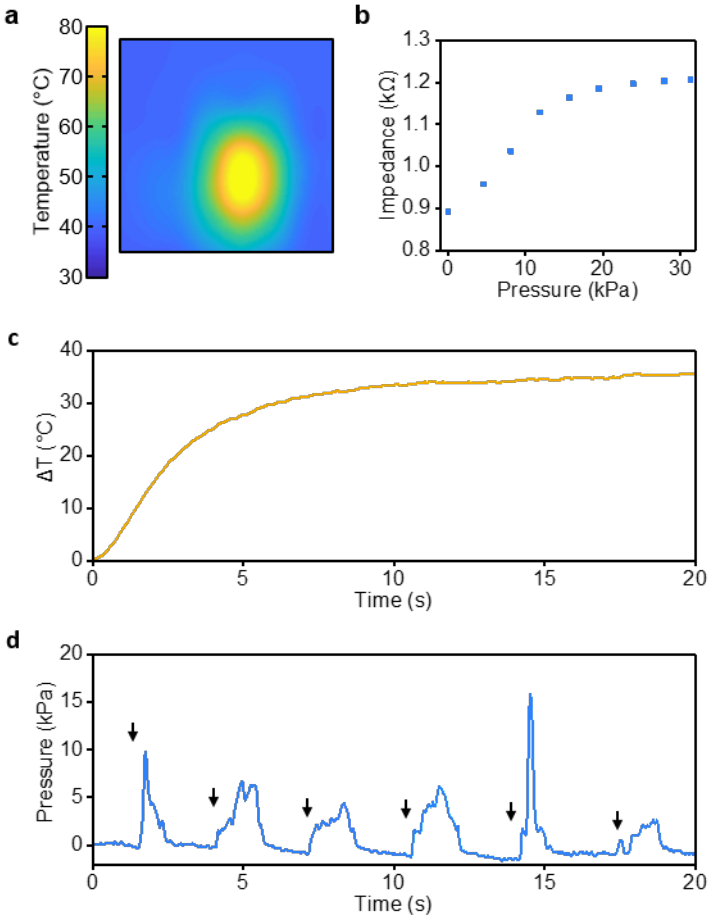

Supplementary Figure 67. Additional results of the simultaneous, multimodal operation of the integrated electrodes, temperature sensors, and pressure sensors. a, Spatial temperature distribution from the results in Fig. 3k after a four-order two-dimensional interpolation. **b,** Influence of pressure on the impedance between the electrode and non-perfused tissue (chicken breast, immersed in 0.1 M PBS). **c,** Response of the temperature sensor during RF ablation and random pressing. **d,** Response of the pressure sensor in constantan during RF ablation and random pressing. Conditions of the RF ablation in (**c,d**): (1) applying RF signals (0.44 W, 400 kHz) to two adjacent electrodes yields bipolar ablation on non-perfused tissue at room temperature; (2) black arrows in (**d**) indicate the manual application of normal forces on the non-perfused tissue during ablation.

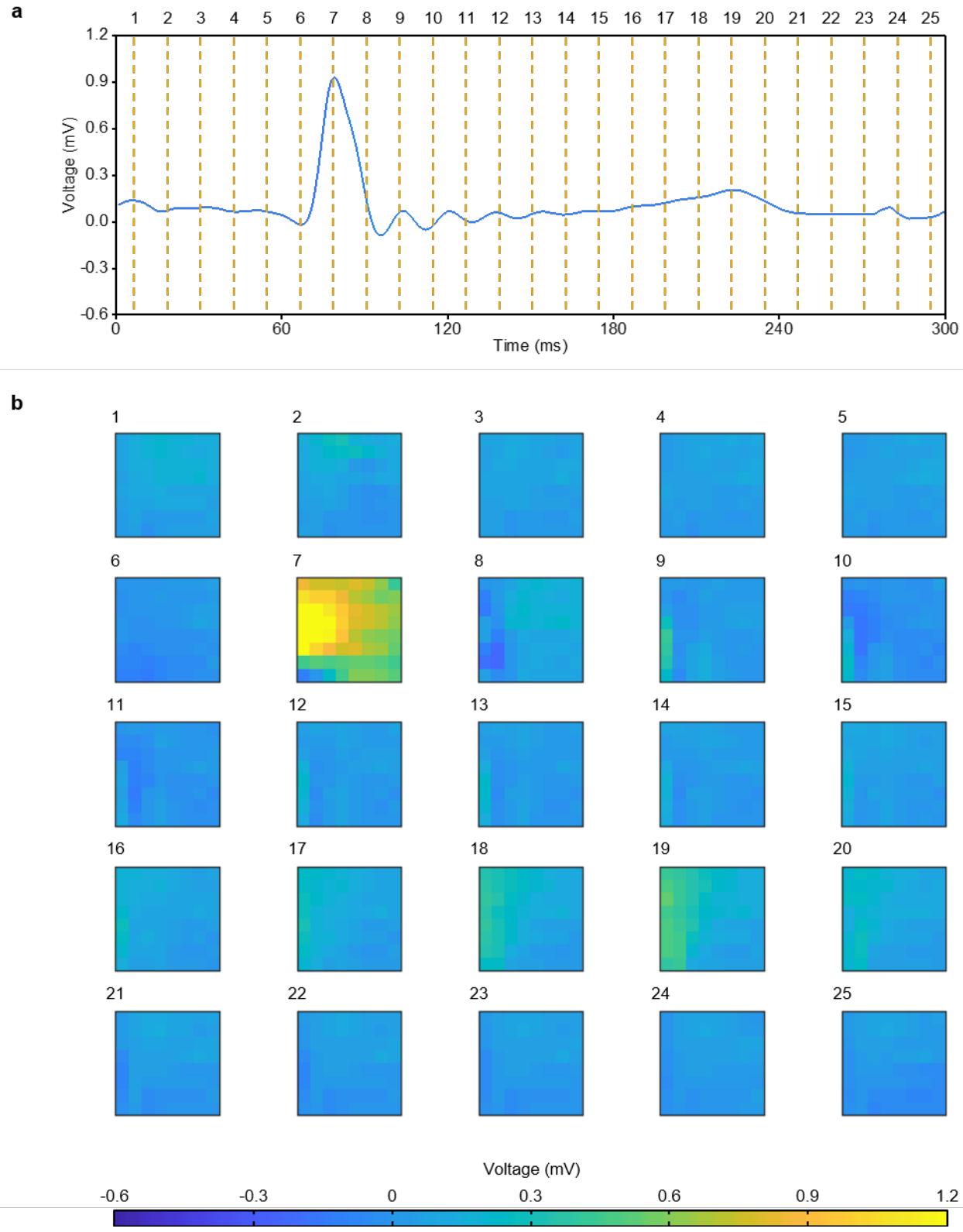

Supplementary Figure 68. Electrogram from a rabbit heart during pacing (200 BPM). a, Electrogram from one electrode. **b,** Electrogram maps in one pacing cycle.

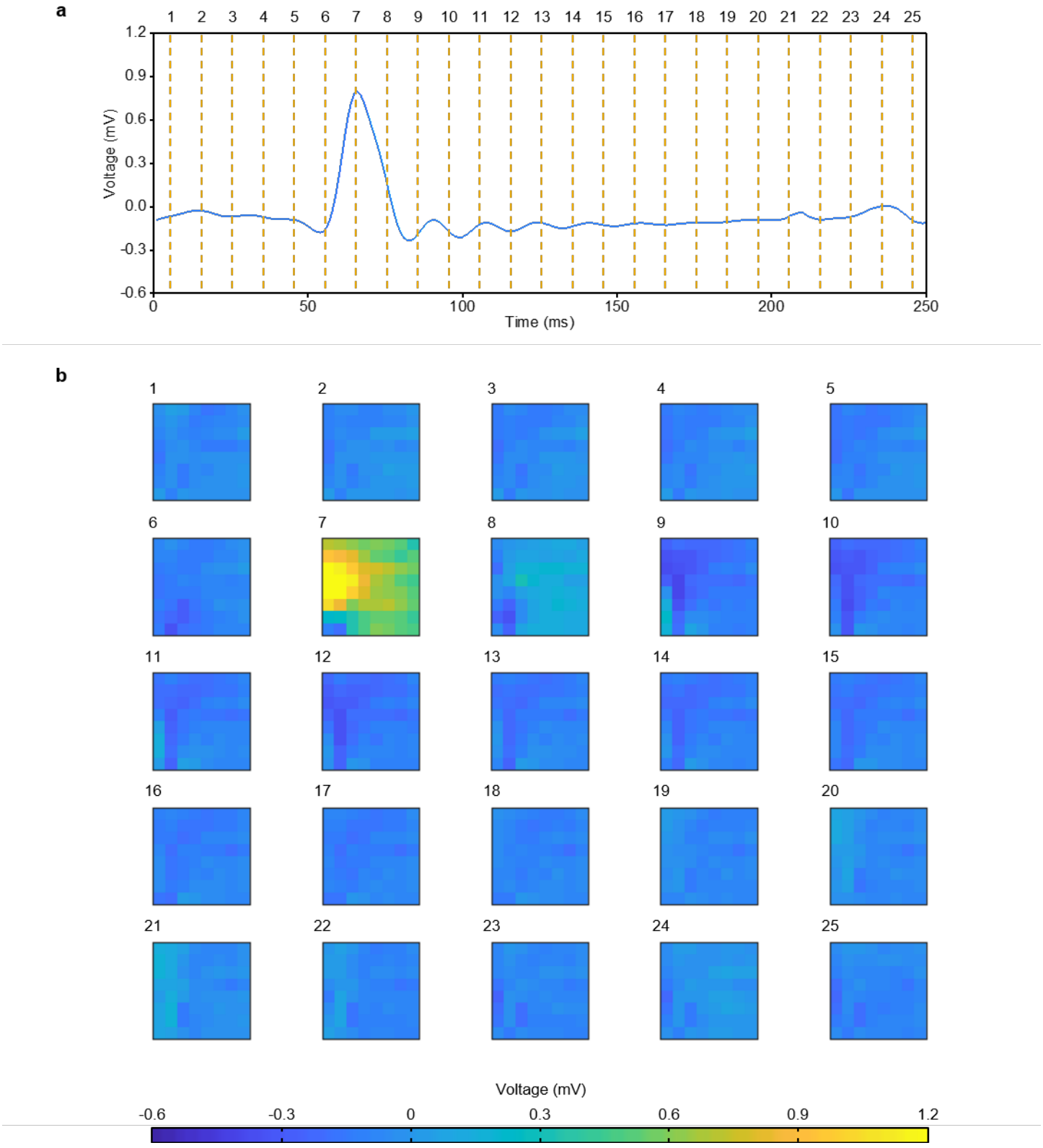

Supplementary Figure 69. Electrogram from a rabbit heart during pacing (240 BPM). a, Electrogram from one electrode. **b,** Electrogram maps in one pacing cycle.

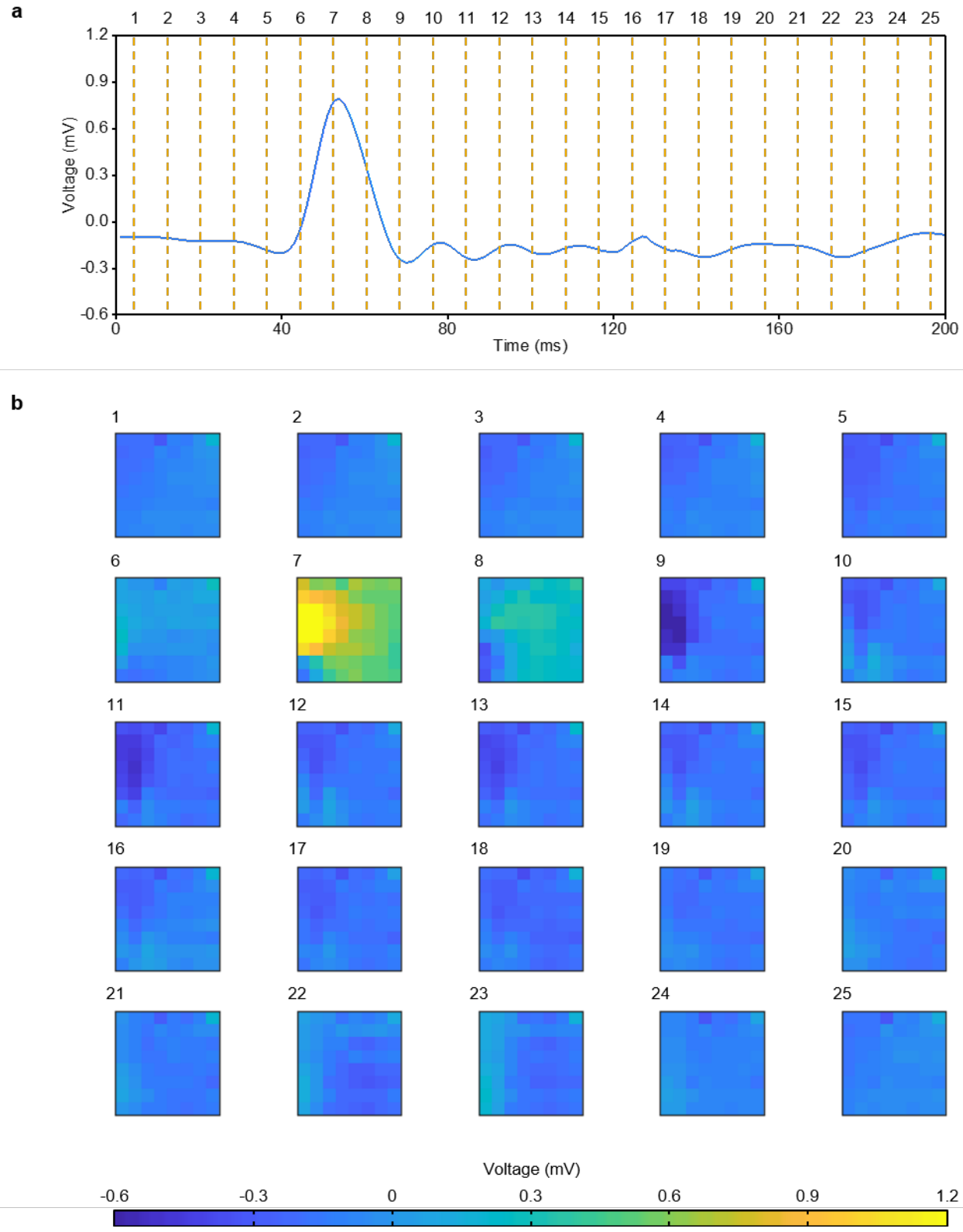

Supplementary Figure 70. Electrogram from a rabbit heart during pacing (300 BPM). a, Electrogram from one electrode. **b,** Electrogram maps in one pacing cycle.

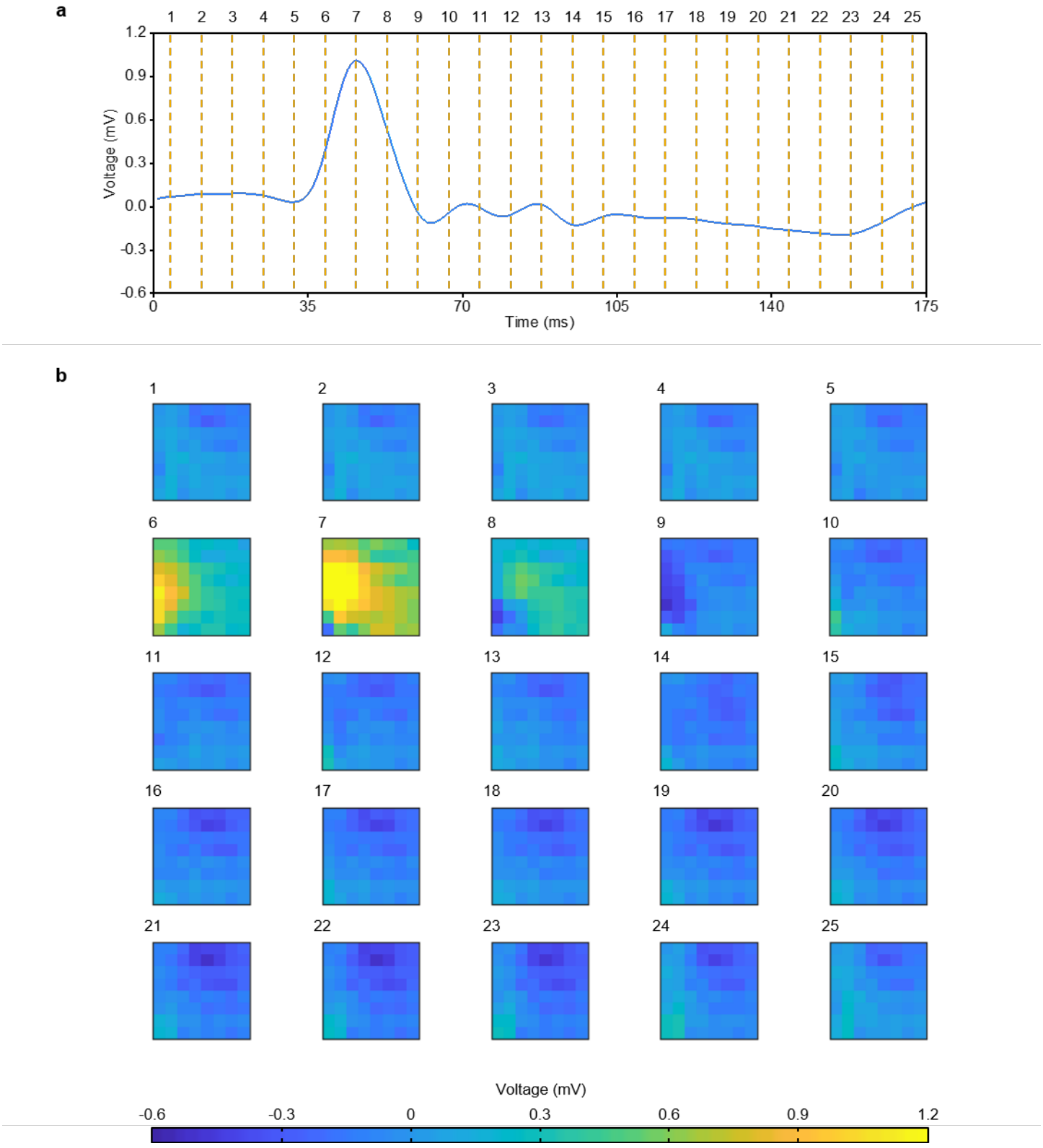

Supplementary Figure 71. Electrogram from a rabbit heart during pacing (343 BPM). a, Electrogram from one electrode. **b,** Electrogram maps in one pacing cycle.

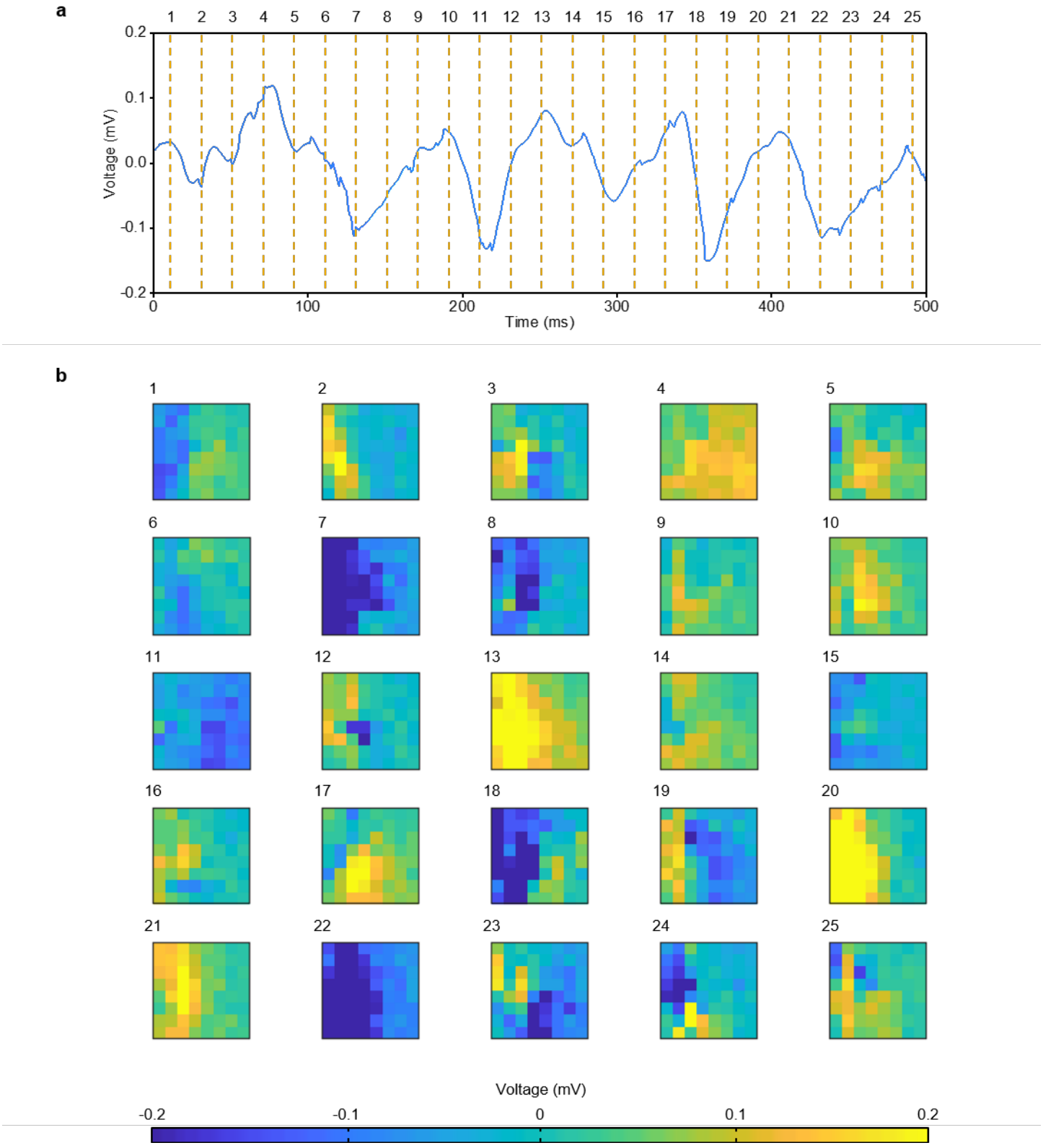

Supplementary Figure 72. Electrogram of a rabbit heart during an arrhythmia. a, Electrogram from one electrode. **b,** Electrogram maps.

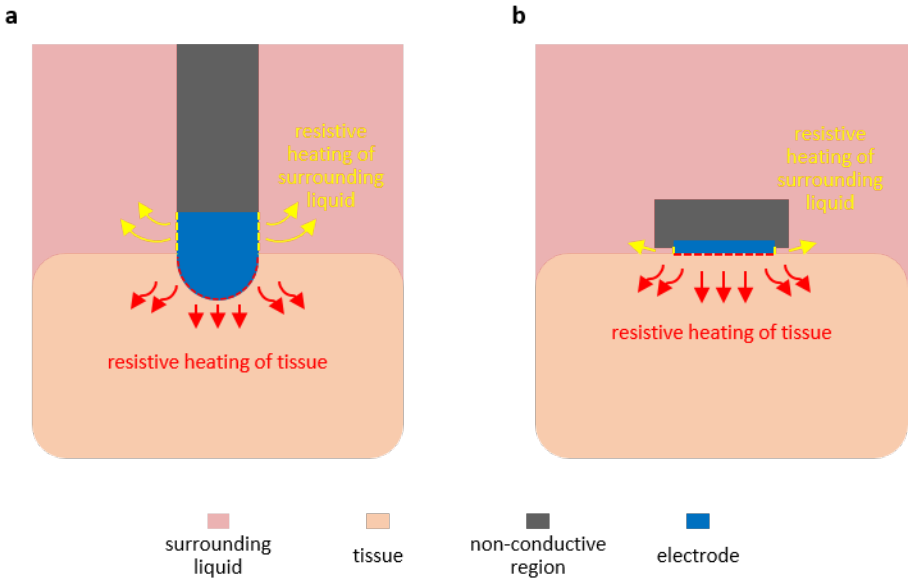

Supplementary Figure 73. Schematic illustrations of electrode interfaces. a, Interfaces between rigid electrode, cardiac tissue, and circulating blood. **b,** Interfaces between soft electrode, cardiac tissue, and circulating blood.

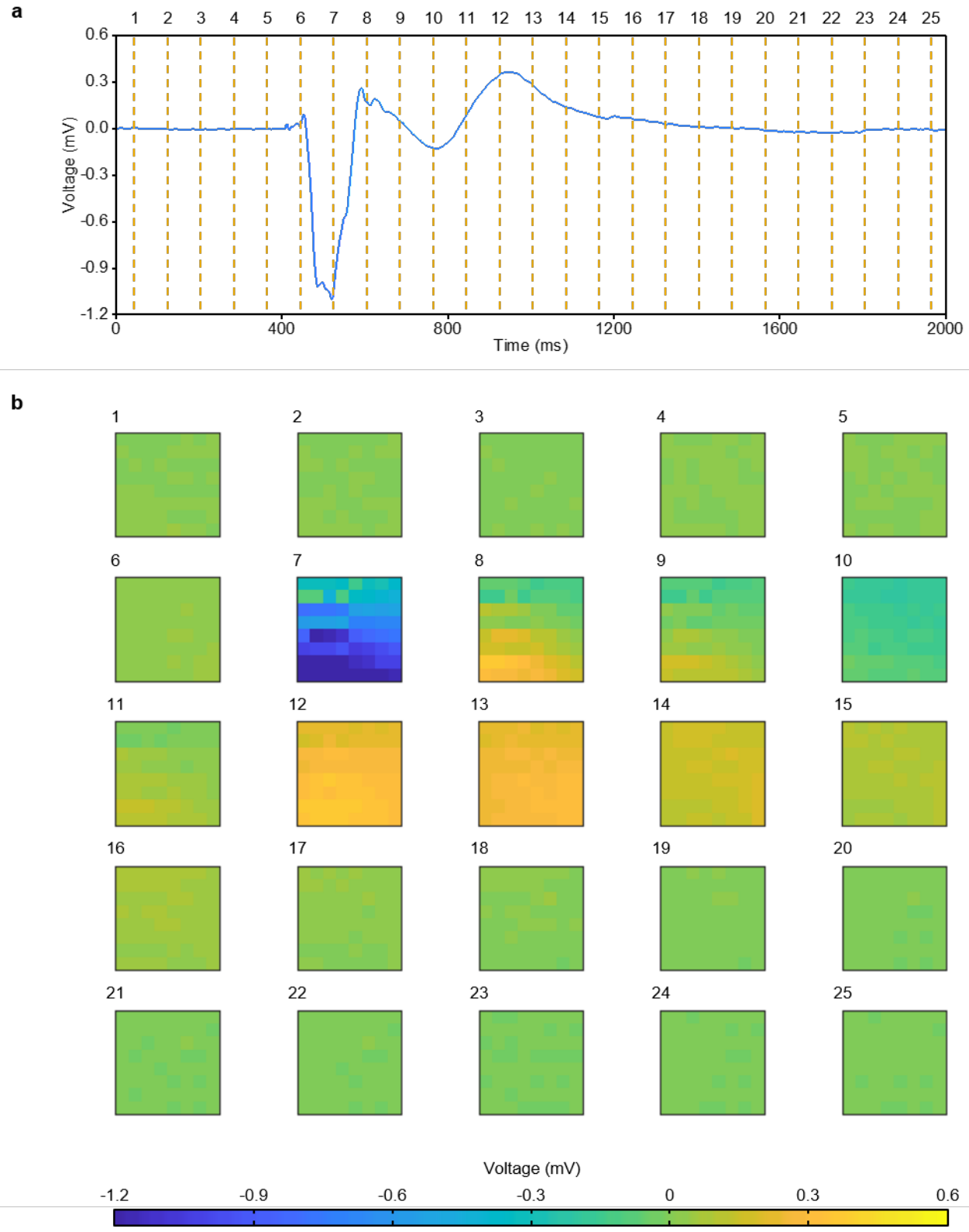

Supplementary Figure 74. Electrogram from a human heart during pacing (30 BPM). a, Electrogram from one electrode. **b,** Electrogram maps in one pacing cycle.

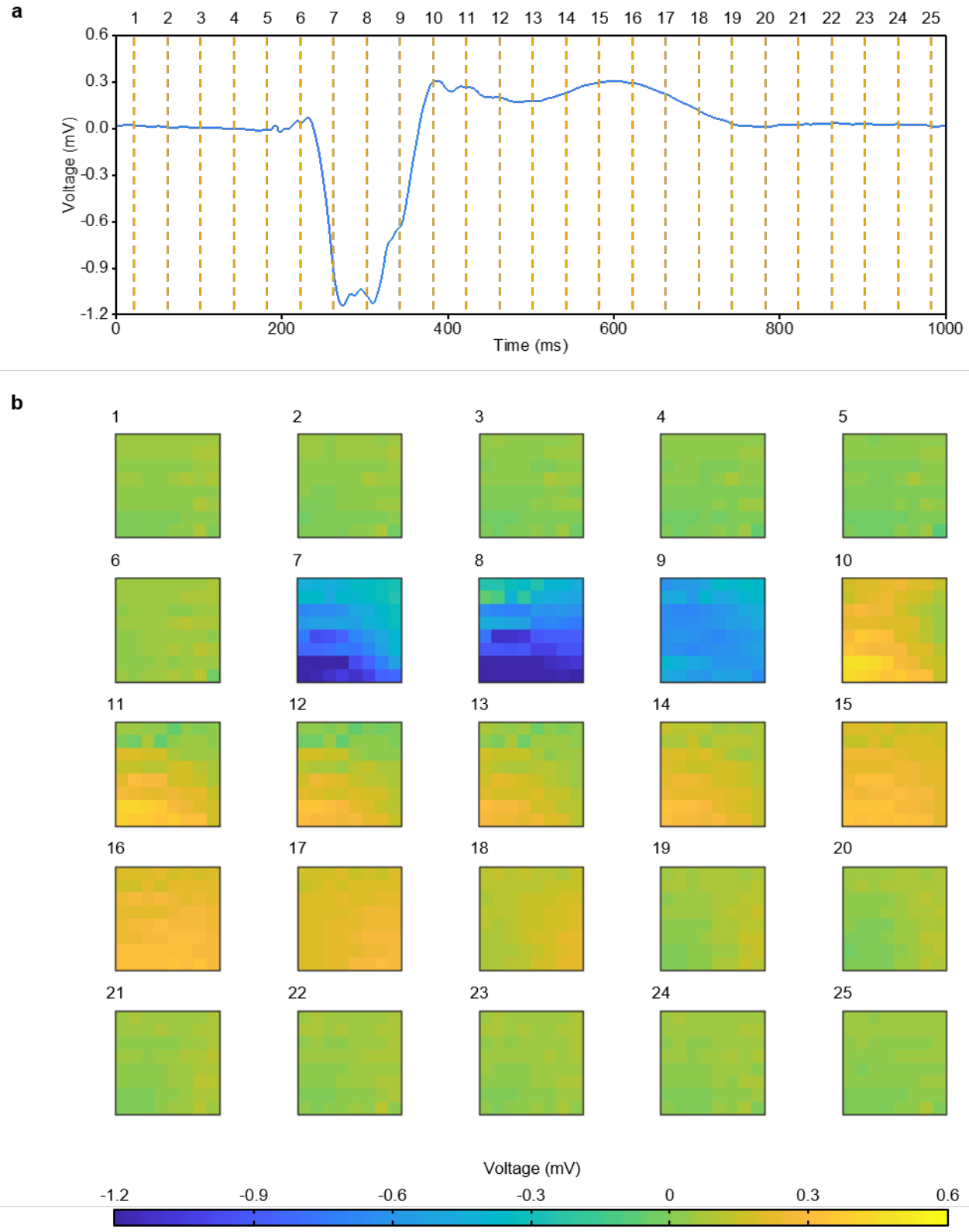

Supplementary Figure 75. Electrogram from a human heart during pacing (60 BPM). a, Electrogram from one electrode. **b,** Electrogram maps in one pacing cycle.

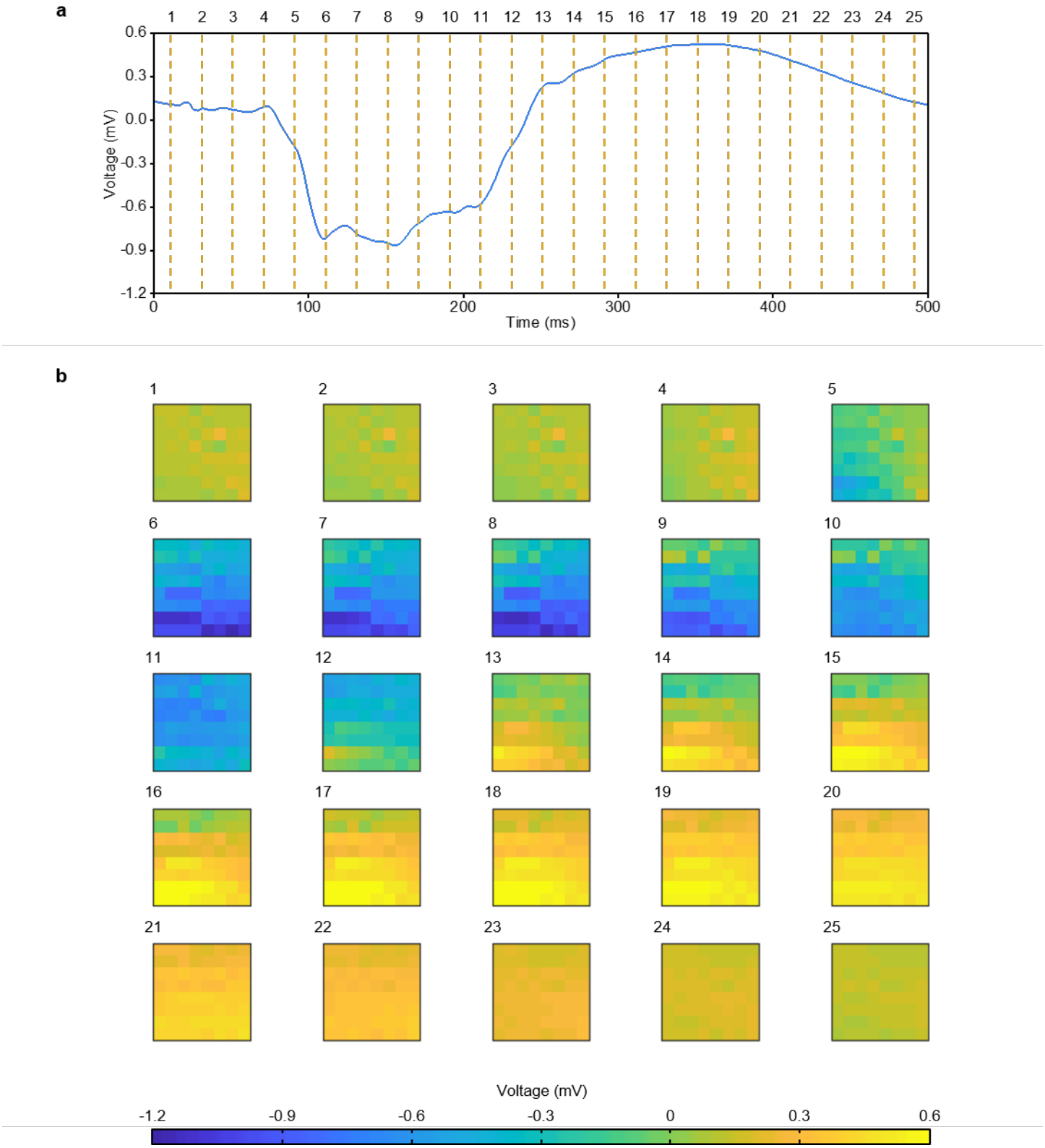

Supplementary Figure 76. Electrogram from a human heart during pacing (120 BPM). a, Electrogram from one electrode. **b,** Electrogram maps in one pacing cycle.

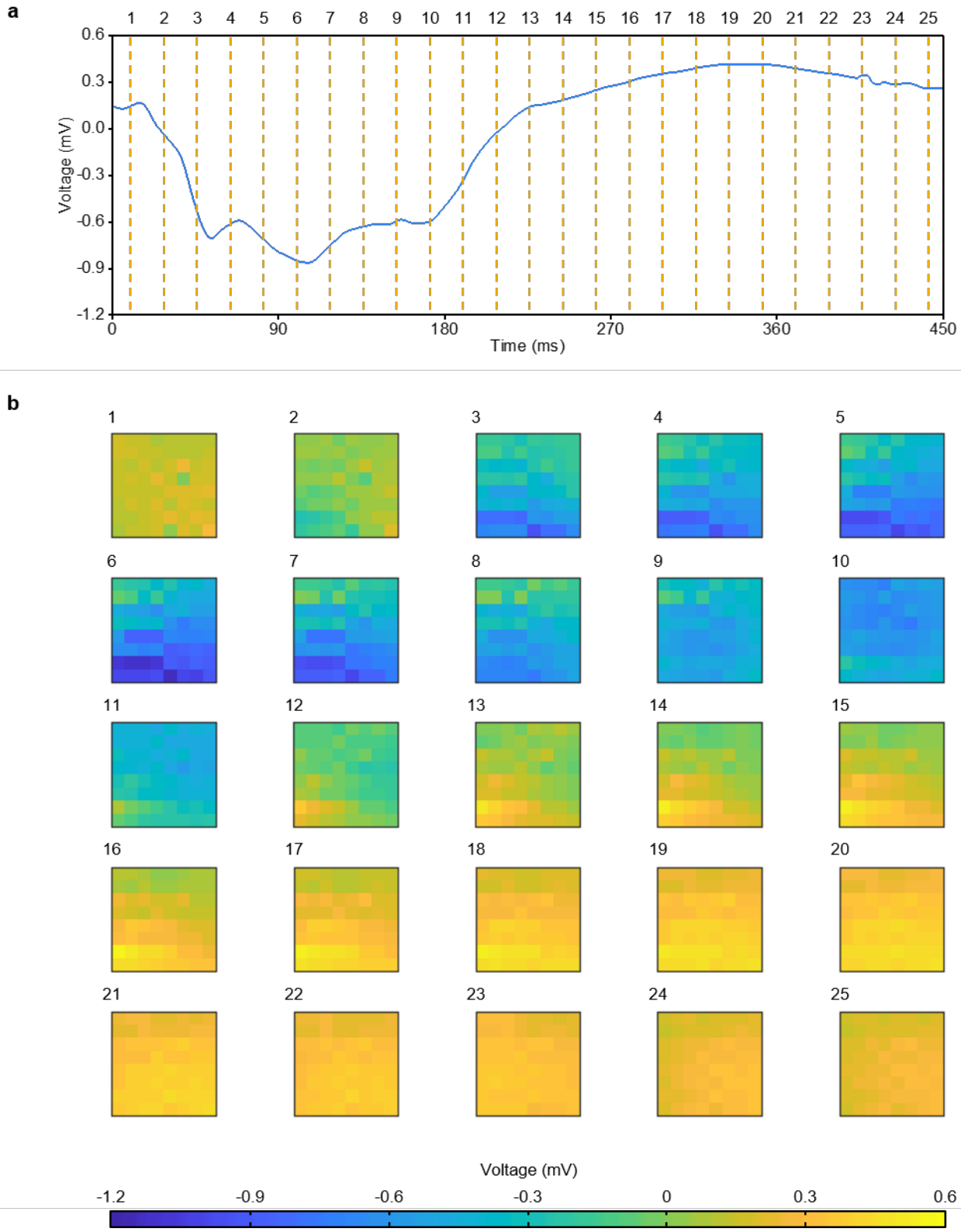

Supplementary Figure 77. Electrogram from a human heart during pacing (133 BPM). a, Electrogram from one electrode. **b,** Electrogram maps in one pacing cycle.

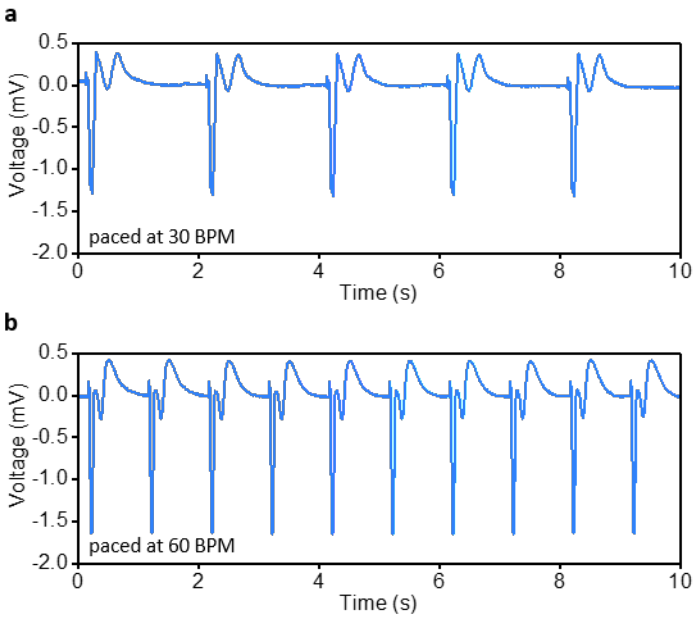

Supplementary Figure 78. Mechanical robustness of the system after attachment to ex vivo Langendorff-perfused human heart models. a, Signals recorded immediately after attachment to the heart (paced at 30 BPM). **b,** Signals recorded ~60 min after attachment to the heart (paced at 60 BPM).

References

[1] Magtibay, Karl, et al. "Physiological assessment of ventricular myocardial voltage using omnipolar electrograms." *Journal of the American Heart Association* 6.8 (2017): e006447.

[2] https://www.bostonscientific.com/content/dam/bostonscientific/ep/general/Blazer%20Family%20of%20Ablation%20Catheters.pdf

[3] Wittkampf, Fred HM, et al. "Myocardial lesion depth with circular electroporation ablation." *Circulation: Arrhythmia and Electrophysiology* 5.3 (2012): 581-586.

Supplementary Video 1. Temperature mapping using the multiplexing circuit with proper grounding.

Supplementary Video 2. Pressure mapping on a porcine heart.

Supplementary Video 3. Electrogram mapping on a rabbit heart.

Supplementary Video 4. Temperature mapping during radio-frequency ablation.

Supplementary Video 5. Electrogram mapping on a human heart.